Measurement of the atmospheric electron and muon neutrino flux with the ANTARES neutrino telescope

Federico Versari

Université de Paris

En cotutelle avec Università di Bologna

Ecole doctorale ED STEPUP 560

Measurement of the atmospheric electron and muon neutrino flux with the ANTARES neutrino telescope

Par Federico Versari

Thèse de doctorat de Physique de l'Univers

Dirigée par Antoine Kouchner, Annarita Margiotta

Et par Tommaso Chiarusi

Présentée et soutenue publiquement le 16/03/2021

Devant un jury composé de :

Coniglione Rosa, Istituto Nazionale di Fisica Nucleare, chercheur INFN, rapporteur
Desiati Paolo, Wisconsin IceCube Particle Astrophysics Center, Senior Scientist, rapporteur
Laura Patrizii, Istituto Nazionale di Fisica Nucleare, chercheur INFN, examinatrice
Andrii Neronov, Université de Paris , PU, examinateur
Isabelle L'Henry-Yvon, Université Paris Saclay, DR CNRS, IJCLAB, examinatrice
Tueros Matis, Instituto de Fisica La Plata, Chercheur CONICET, examinateur
Kouchner Antoine, Université de Paris, PU, Directeur de thèse
Margiotta Annarita, Université de Bologne, PU, Co-Directrice de thèse
Maurizio Spurio, Université de Bologne, PU, membre invité

Mots clefs: Neutrino, neutrinos atmosphériques, rayons cosmiques, télescope neutrino, physique des particules

Keywords: Neutrino, atmospheric neutrinos, cosmic rays, neutrino telescope, particle physic

Résumé

Les neutrinos atmosphériques sont des particules secondaires produites par des rayons cosmiques (RC) primaires interagissant dans l'atmosphère terrestre.

En raison du besoin de très grands détecteurs, seules quelques mesures du flux différentiel ont été effectuées par des télescopes à neutrinos souterrains, à savoir AMANDA, IceCube et SuperKamiokande. Il existe également une mesure historique de la collaboration de Fréjus.

Différents cadres théoriques sont disponibles pour estimer les flux de neutrinos atmosphériques. a des énergies de 100 GeV à 1 PeV, les principales sources de ν_μ sont des désintégrations semi-leptoniques et à trois corps de kaons chargés, tandis que les contributions des désintégrations de pions et de muons dominent en dessous de 100 GeV.

Ce flux de neutrinos *conventionnel* tend vers une loi de puissance $\Phi_\nu^c \propto E_\nu^{-\gamma_{CR}-1}$, où γ_{CR} est l'indice spectral des RC primaires. Le rapport de flux ν_μ/ν_e est ~ 2 dans la gamme du GeV et augmente avec l'énergie, atteignant un facteur ~ 20 à 1 TeV.

En règle générale, l'énergie du RC primaire est environ 20 fois supérieure à l'énergie du neutrino secondaire.

Les incertitudes sur les modèles de flux conventionnels à des énergies neutrinos supérieures a 1 TeV sont principalement dues à une mauvaise connaissance du spectre en énergie et de la composition des RC primaires, ainsi que des interactions hadroniques.

Les effets d'oscillation pour les ν atmosphériques sont négligeables au-dessus de $\sim$ 100 GeV. En conséquence, la contribution des neutrinos tau n'est pas prise en compte dans cette analyse car la production de ν_τ dans l'atmosphère est rare: elle est dominée par la désintérgration $D_s^+ \to \tau^+\nu_\tau$, suivie par la désintérgration du τ.

Cette thèse décrit une stratégie pour sélectionner des événements *shower-like* et *starting track*, caractéristiques des neutrinos, parmi le bruit de fond des muons atmosphériques avec les données collectées par le télescope à neutrinos ANTARES. Les distributions des événements observés sont traitées (*unfolding*) pour obtenir les spectres en énergie des ν_μ

et ν_e atmosphèriques, en tenant compte de la réponse du détecteur. Les résultats sont comparés à ceux obtenus par d'autres expériences.

Le télescope ANTARES est un détecteur de neutrinos utilisant la technique Tchérenkov. Il est situé en haute mer, à 40 km au large de Toulon, France, dans la mer Méditerranée. Le détecteur comprend un réseau tridimensionnel de 885 modules optiques, chacun contenant un tube photomultiplicateur (PMT) de 10 pouces.

Les modules optiques sont répartis le long de 12 lignes verticales ancrées au fond marin à des distances d'environ 70 m les unes des autres et à une profondeur d'environ 2500 m.

Les particules au-dessus du seuil Tchérenkov induisent un rayonnement cohérent émis dans un cône d'angle caractéristique $\theta_C \simeq 42^\circ$ dans l'eau.

Achevé en 2008, le télescope vise principalement la détection des muons traversants induits par les neutrinos.

La position, le temps et la charge collectée des hits, les signaux induits dans le PMT par les photons détectés, sont utilisés pour reconstruire la direction et l'énergie des événements induits par les interactions des neutrinos, mais aussi par les muons atmosphériques.

Des conditions de déclenchement basées sur des combinaisons de coïncidences locales sont appliquées pour distinguer les signaux dus à des événements physiques des bruits de fond optique du à l'environnement (désintégrations de ^{40}K et bioluminescence). Pour les études d'astronomie, les muons atmosphériques et les neutrinos atmosphériques constituent la principale source de bruit de fond.

Cette analyse se concentre sur les événements induits par les neutrinos dont les interactions sont contenues à l'intérieur (ou à proximité) du volume de détection instrumenté. Ces événements comprennent: des événements de type *shower-like* composés d'interactions à courant chargé (CC) de ν_e, produisant des gerbes électromagnétiques et hadroniques, des interactions à courant neutre (NC) de neutrinos de toutes saveurs induisant des gerbes hadroniques et des événements de type *starting track* composés des interactions CC de ν_μ, avec une gerbe hadronique près du point d'interaction et un muon qui s'en échappe.

Les événements collectés par le détecteur ANTARES sont reconstruits par plusieurs algorithmes. L'algorithme de reconstruction des traces (*tracks*) utilisé dans les analyses ANTARES est appelé AAFit et fournit la direction de la particule indidente avec son incertitude angulaire estimée ; le nombre de hits utilisés pour la reconstruction ; et un paramètre de qualité, appelé Λ.

Les événements de type *shower* se produisant à proximité du volume instrumenté sont reconstruits avec un algorithme dédié, TANTRA ; cette méthode basée sur une fonction de vraisemblance permet de reconstruire les coordonnées des points d'interaction, la direction du neutrino incident et son l'énergie.

Toutes les analyses ANTARES suivent une politique *en aveugle* pour éviter d'éventuels biais. Les coupes et les critères de sélection sont étudiés et optimisés sur un échantillon

d'événements simulés par Monte Carlo (MC) et c'est seulement à la fin de la chaîne de sélection complète que ces coupures sont appliquées aux données. Un petit échantillon contenant 10% des données réelles uniformément réparties sur la durée de l'expérience est utilisé pour vérifier la concordance avec les événements MC le long de la sélection.

Pour ces travaux, les données collectées de 2007 à fin 2017 ont été utilisées. Seules les analyses sans niveau de bioluminescence élevé ont été sélectionnées. La durée de vie totale correspond à 3012 jours. Le bruit de fond résultant est presque entièrement dû aux RC μ (muons atmosphériques) : après déclenchement et reconstruction, le rapport signal à bruit attendu est $\sim 10^{-4}$.

La suppression du bruit de fond est organisée en trois étapes différentes. Une présélection initiale, appelée conditions de départ, d'événements de types *shower-like* et *starting track* combine les informations des algorithmes de reconstruction AAFit et TANTRA, selon les exigences suivantes: la direction de l'événement telle que reconstruite par AAFit doit être ascendante (ie, angle zénithal $> 90°$), pour rejeter la plus grande fraction de RC μ; le vertex d'interaction neutrino reconstruit par TANTRA doit être contenu dans un volume cylindrique de rayon axial de 300 m et de hauteur de 500 m, centré au centre de gravité des modules optiques; l'incertitude angulaire estimée par TANTRA sur la direction de l'événement doit être $< 30°$ et le paramètre de qualité $M_{est} < 1000$, pour supprimer les événements mal reconstruits.

La deuxième étape utilise le paramètre de qualité AAFit, Λ. Le meilleur compromis pour supprimer le plus grand pourcentage de fond tout en conservant une fraction suffisamment importante d'événements de signal est obtenu en supprimant les événements avec $\Lambda \leq -5,7$.

Après cette coupure, 25% du signal survit, avec environ 30 événements de fond restants pour chaque neutrino atmosphérique. La classification finale des événements en tant que signal ou bruit de fond est effectuée avec un arbre de décision boosté (*Boosted Decision Tree* BDT), défini sur un espace de paramètres multidimensionnels.

Un BDT est un algorithme qui appartient à la famille des techniques d'apprentissage automatique supervisé (*supervised machine learning*). Pour créer la fonction de classification, des échantillons d'apprentissage sont nécessaires. Les événements RC μ simulés constituent l'échantillon de bruit de fond. Les interactions CC de ν_e atmosphériques sont utilisées comme signal.

Ce choix est motivé par le fait que la saveur ν_e produit le cas le plus propre d'événements de type *shower* et c'est le canal le plus difficile à mesurer dans les télescopes à neutrinos. Pour chaque événement RC μ ou ν_e, le classificateur est entraîné en utilisant 15 quantités. Certaines de ces quantités proviennent de la sortie des algorithmes AAFit et TANTRA et une autre variable d'apprentissage, appelée paramètre RC μ veto a été spécifiquement développée dans ce travail pour améliorer la puissance de séparation signal - fond du BDT.

La sortie BDT est un excellent discriminateur entre les événements atmosphériques ν_e et les RC μ (muons atmosphériques).

La condition BDT $> 0,33$ qui supprime tous les RC μ présents dans les événements MC est choisie comme critère de sélection. Une extrapolation de la queue de distribution BDT, en supposant une forme gaussienne, fournit une estimation prudente des événements de fond d'au plus ~ 3 dans l'échantillon final, ce qui sera utilisé dans la suite.

Afin de dériver des données les spectres en énergie ν_e et ν_μ, une méthode de dépliage (*unfolding*) est utilisée. Les deux vraies distributions sont déconvoluées de celle mesurée expérimentalement, sur la base de la réponse du détecteur et des hypothèses faites sur les taux d'interaction des différentes saveurs de neutrinos.

Le résultat de cette procédure, couplée avec l'acceptance du détecteur et la durée de vie de l'expérience, donne un spectre qui permet une comparaison directe avec d'autres expériences. La procédure de dépliage a été effectuée avec l'algorithme TUnfold qui est largement testé et validé dans le contexte de la physique des hautes énergies et peut gérer une ou plusieurs sources de bruit de fond.

L'énergie estimée par l'algorithme de reconstruction TANTRA est utilisée pour construire la distribution d'entrée pour l'algorithme de dépliage. Les événements avec BDT $> 0,33$ sont des ν_μ ou ν_e atmosphériques avec une contamination de moins de quelques pour mille de RC μ et une fraction ~ 1 % de neutrinos cosmiques; les deux échantillons sont considérés comme du bruit de fond.

Dans la procédure de dépliage, l'utilisation de l'énergie des événements reconstruite est limitée aux énergies comprises entre ~ 100 GeV et ~ 50 TeV. La borne inférieure est déterminée par le fait que notre algorithme de reconstruction ne peut pas reconstruire de manière fiable les énergies des neutrinos en dessous de 100 GeV.

Au-dessus de 50 TeV, les statistiques d'événements sont considérablement réduites par l'exigence de confinement du vertex d'interaction à l'intérieur ou à proximité du volume instrumenté. De plus, les neutrinos cosmiques, dont le flux souffre de grandes incertitudes, commencent à constituer le bruit de fond dominant. À partir du spectre d'événements déplié, pour les neutrinos électronique et muonique, un calcul du flux d'énergie différentiel dans les unités appropriées (GeV $^{-1}$ cm $^{-2}$ s $^{-1}$ sr $^{-1}$) a été fait, en tenant compte de la surface effective.

Ce paramètre est la caractéristique d'un télescope à neutrino, représentant la taille d'une cible hypothétique efficace à 100% que le détecteur offre à un certain flux de neutrinos simulé. L'erreur statistique dans le flux d'énergie différentielle est déterminée par la méthode TUnfold. La simulation MC dépend d'un certain nombre de paramètres avec des incertitudes associées.

L'impact est estimé en faisant varier à chaque fois un seul des paramètres suivants, et en produisant des jeux de données de simulation dédiées : l'efficacité globale des modules optiques, modifiée de $+10\%$ et -10%, l'incertitude sur les propriétés de l'eau, en augmentant et diminuant de 10 % la longueur d'absorption de la lumière dans l'eau par rapport à la valeur nominale, les incertitudes liées aux flux de neutrinos utilisés, y compris un changement de pente de $\pm 0,1$ dans l'indice spectral, indépendamment pour ν_e et ν_μ.

Chaque échantillon de MC modifié a ensuite été utilisé comme pseudo-données utilisées pour le dépliage. L'écart du contenu de chaque bin de E_ν du spectre obtenu avec les données nominales MC correspond à l'incertitude systématique associée à la variation du paramètre. Les erreurs statistiques de nos spectres de neutrinos atmosphériques dépliés dominent largement les erreurs systématiques.

La mesure du flux de neutrinos électroniques à haute énergie est difficile, car de très grands détecteurs sont nécessaires pour collecter des statistiques suffisantes, en plus des raisons liées de grandes incertitudes systématiques.

Les mesures de IceCube-DeepCore et IceCube reposent sur environ 200 interactions de ν_e dans le milieu de la glace polaire. La mesure actuelle est effectuée dans l'eau de mer, dans des conditions environnementales et avec des incertitudes systématiques complètement différentes, donnant des résultats cohérents avec ceux obtenus dans la glace polaire. Pendant une durée de vie de 3012 jours, environ 130 ν_e interactions ont été reconstruites dans le volume instrumenté d'ANTARES.

Le statistique de l'échantillon ν_e n'est pas suffisante pour tester des modèles au-dessus de quelques dizaines de TeV. En dessous de 100 GeV, la densité des PMT du détecteur ANTARES est insuffisante pour reconstruire un nombre significatif d'événements.

Concernant le flux ν_μ déplié obtenu, il apparait en accord avec la mesure précédente d'ANTARES, obtenue avec un échantillon d'événements traversants engendrés par des interactions neutrinos externes au volume instrumenté, c'est-à-dire un échantillon de données totalement indépendant.

La structure du manuscrit de thèse est la suivante: un rappel des connaissances sur les rayons cosmiques et la physique des neutrinos atmosphériques est donné dans le chapitre 1. Le chapitre 2 est consacré aux télescopes à neutrinos et les topologies des événements qu'ils peuvent détecter.

Dans le chapitre 3, le télescope à neutrinos ANTARES est décrit en détail. Dans le chapitre 4, le logiciel développé pour les simulations Monte Carlo d'ANTARES et la reconstruction d'événements, ainsi qu'une description de l'arbre de décision boosté utilisé dans cette thèse, sont décrits.

Le chapitre 5 contient les détails de la chaîne de sélection d'événements innovante spécifiquement développée pour cette thèse. Enfin, les chapitres 6 et 7 sont consacrés à la description de la procédure d'unfolding des événements sélectionnés et au calcul des spectres en énergie des neutrinos atmosphériques électroniques et muoniques.

Abstract

High energy atmospheric neutrinos are the topic of this thesis. They are produced in particle cascades initiated by the interaction of cosmic rays consisting mainly of protons, Helium and other heavier nuclei and spanning many orders of magnitude in energy, with the nuclei of the Earth's atmosphere A possible way to detect high energy neutrinos using huge volumes of transparent natural material such as ice or sea water was proposed by Markov in 1960. High energy neutrinos undergoing weak interactions with one of the nucleons of the medium produce relativistic charged particles than can originate Cherenkov radiation. Cherenkov photons can then be detected by a lattice of photosensors. The ANTARES neutrino telescope is a three-dimensional array of photomultipliers distributed over 12 lines, installed at the bottom of the Mediterranean Sea. The detector was operated in partial configurations since March 2006 and completed in May 2008. It has been taking data continuously since then. In this thesis, a measurement of the atmospheric electron and muon neutrino spectra with the ANTARES neutrino telescope, using ten years of data collected from 2007 to 2017, is presented. This is the first atmospheric electron neutrino flux measurement ever done with ANTARES and is the first two flavours atmospheric neutrino spectra measurement ever done in the energy range between around 100 GeV and 100 TeV. To achieve these results a new event selection chain has been developed to reject the background of atmospheric muons and select events induced by electron or moun neutrinos in (or close to) the instrumented volume of the detector. In addition, an unfolding procedure able to treat several signal sources has been applied. The structure of the thesis is the following: the basics of cosmic rays and the physics of atmospheric neutrinos are discussed in chapter 1, chapter 2 is dedicated to illustrate the neutrino telescopes and the topologies of events that they can detect. In chapter 3 the ANTARES neutrino telescope is described in detail. In chapter 4 the software developed for the ANTARES Monte Carlo simulations and the event reconstruction, together with a description of the boosted decision tree used in this thesis, are described. Chapter 5

contains the details of the innovative event selection chain specifically developed for this thesis. Finally, chapter 6 and 7 are dedicated to the description of the unfolding procedure of the selected events and to the calculation of the energy spectra of atmospheric electron and muon neutrinos.

Contents

1 Atmospheric Neutrinos

Cosmic rays (CRs) were discovered in 1912 by V. Hess [1]. Using three golden electrometers he measured the amount of radiation up to an altitude of 5300 meters in a free balloon flight. He found that the level of radiation increased with altitude, showing that some kind of radiation enters the atmosphere from above. This was in contradiction with the hypothesis that the flux of ionizing particles arised from Earth's radioactive rocks exclusively. He gave the name of "cosmic radiation" to this phenomenon. Hess received the Nobel Prize in Physics in 1936 for his discovery. Many investigations have been made on the nature of cosmic rays since then, but their origin and the mechanisms connected to their acceleration are not yet completely clear.

Figure 1.1: Historical photograph of Hess preparing for a balloon flight (American Physical Society)

1.1 Cosmic Rays

Cosmic particles hit the top of the Earth's atmosphere at the rate of about 1000 per square meter per second. They are characterized by two components: hadrons, which are protons ($\sim$ 87%), Helium ($\sim$ 12%) and heavier nuclei ($\sim$ 1%), and leptons, which are about 100 times less abundant.

The measured all-particle differential energy spectrum of CRs, which ranges from 10^9 to 10^{20} eV, is shown in Fig. 1.2. The primary CR energy spectrum can be described as a power law:

$$\frac{dN}{dE} \propto E^{-\gamma} \tag{1.1}$$

where E is the CR energy and γ the spectral index. As shown in Fig. 1.2, at least three

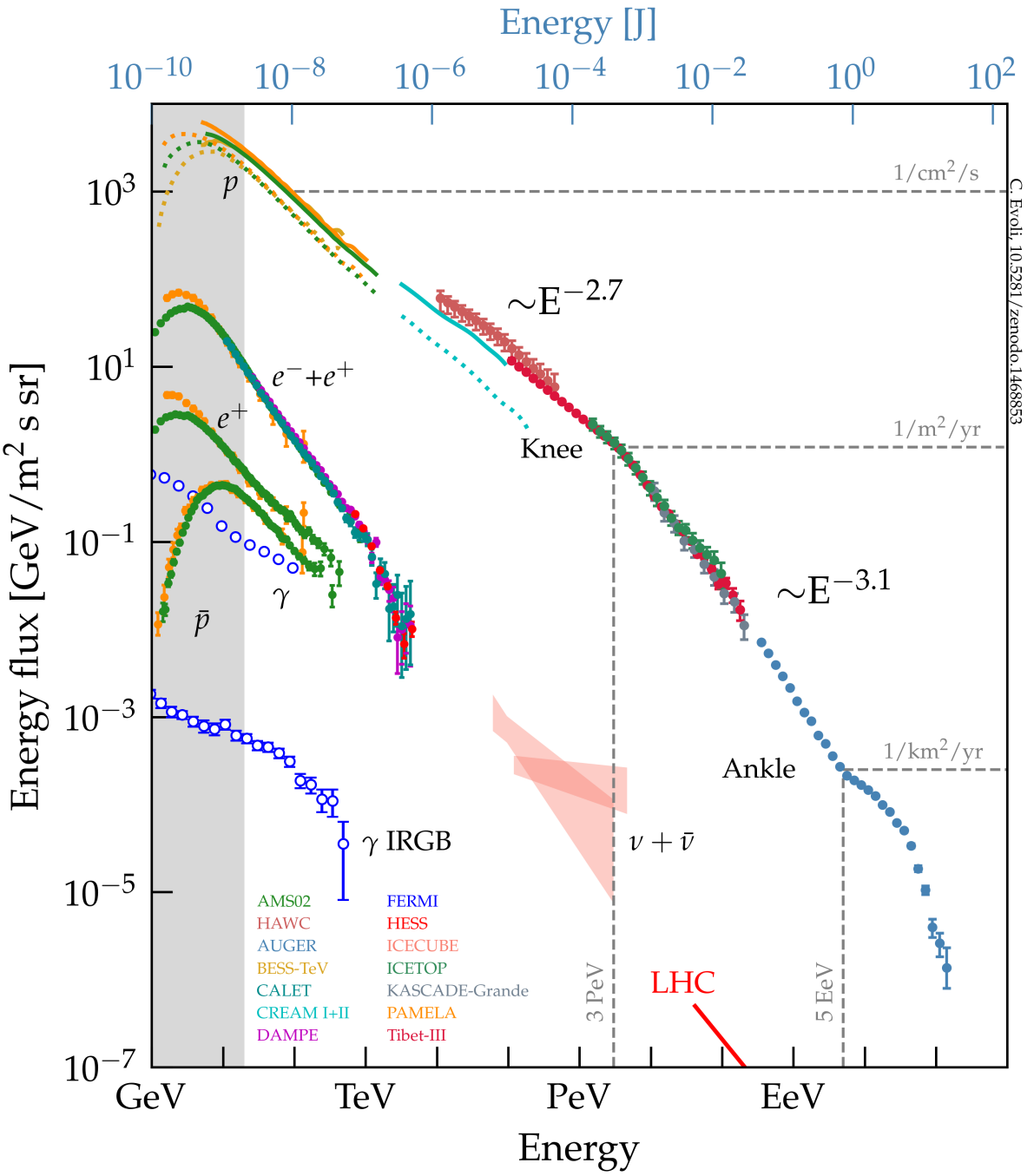

Figure 1.2: Energy flux of CRs observed at Earth by several experiments. The grey shaded region shows the energies where the CR flux is influenced by solar modulation. Figure taken from [2].

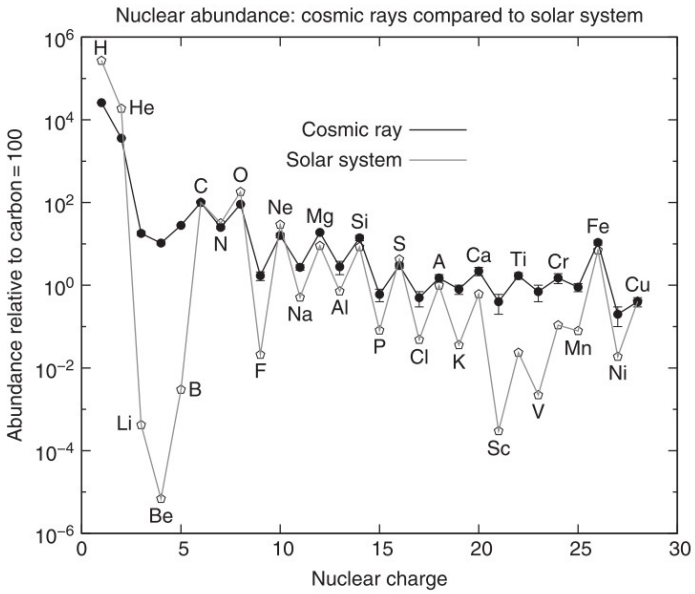

Figure 1.3: The cosmic ray elemental abundances measured on Earth (filled symbols connected by solid lines) compared to the solar system abundances (open symbols), all relative to carbon = 100. Figure taken from [3].

regions can be identified in the spectrum, characterised by different values of the index:

- $E \lesssim 3 \cdot 10^{15}$ eV, $\gamma \sim 2.7$. CRs up to this energy (called the *knee* region of the spectrum) are usually considered to be produced by sources located in our Galaxy;
- $3 \cdot 10^{15}$ eV $< E < 3 \cdot 10^{19}$ eV, $\gamma \approx 3.1$. In this energy range a transition from Galactic to extra-Galactic sources is expected;
- $E \approx 3 \cdot 10^{19}$ eV, $\gamma \approx 2.7$. At extremely high energies a flattening of the energy spectrum, known as the *ankle*, appears and the spectral index is again ~ 2.7;

Anti-protons and positrons are included on Fig. 1.2. They are mostly "secondary particles" being produced by collisions of "primary" cosmic ray nuclei during their propagation in the interstellar medium. In the figure also the cosmic neutrino flux discovered by IceCube [4, 5] and confirmed, though with a lower significance, by the ANTARES neutrino telescope [6] is shown.

The elemental composition of CR radiation is quite similar to what is observed in the Solar System, with some evident differences as shown in Fig. 1.3: Li-Be-B and Sc-Ti-V-Cr-Mn are relatively more abundant in CRs than in the Solar System by several orders of magnitude. Collisions (spallation processes) in the interstellar medium (ISM) of primary C and O nuclei, for the first group, and of Fe nuclei for the second one produce

an enhancement of their relative abundance [7]. From the knowledge of cross sections for spallation, one can learn something about the amount of matter traversed by cosmic rays between production source and the observation site.

Together with the absolute composition of cosmic rays it is interesting to understand which is the energy shape of the spectrum for each species of primary CRs. Fig. 1.4 shows the major nuclear components in CRs as a function of the energy-per-nucleus, in the energy range below the *knee*. The spectrum is described by a power law and its spectral index γ_i, where i indicates the nuclear species, is almost the same for all, apart from protons. It should also be noticed that data reported in Fig. 1.4 have been obtained mainly through balloon-borne experiments (CREAM [9], ATIC [10] and TRACER [11]) with a good agreement between the different measurements.

1.1.1 CR composition models

Various attempts have been made to reconstruct the all-particle flux in terms of its individual components, *e.g* assuming power-law shape extrapolation from direct composition and flux measurements combined with rigidity-dependent cut-offs to accomodate the behaviour in the knee region and beyond. An overview of these possible fits to the all-particle spectrum is provided in reference [28]. In general, several mass groups are considered for the primary composition and different fits become possible to describe the spectrum. In addition, different source populations can be assumed, inducing different rigidity dependent cutoffs. Some example are the so-called *Hillas models* [29] or the *Gaisser-Stanev-Tilav models* [28]. A more global approach is followed by the authors of the Global Spline Fit [31], where the constraints on the power-law spectral behaviour and rigidity dependent cut-offs are relaxed.

1.1.2 Galactic CR sources

Baade and Zwicky [12] proposed that supernovae can provide the adequate energetics to explain the observed flux of CRs. Later, it was recognized that relativistic particles can be effectively accelerated via Fermi mechanisms [13, 14] at shock waves during the expansion of supernova remnants (SNRs) in the interstellar medium. The present formulation of this idea is often referred to as the Supernova Remnant paradigm for the origin of CRs and it relies on some observations, namely:

- **CR energy balance**: In a core-collapse SN around 10 Solar masses are ejected with a velocity $U \sim 5 \times 10^8$ cm/s. Assuming ~ 3 SNs per century in the Galaxy, the average output power from Galactic supernovae is $P_{SN}^{kin} \sim 3 \times 10^{42}$ erg/s. This value is one or two orders of magnitude larger than the power $P_{CR} \sim 5 \times 10^{40}$ erg/s requested to maintain the steady cosmic ray measured energy density $\rho_{CR} \sim 1$ eV/cm^3. To fulfill the energy balance requirement, the CR acceleration mechanism

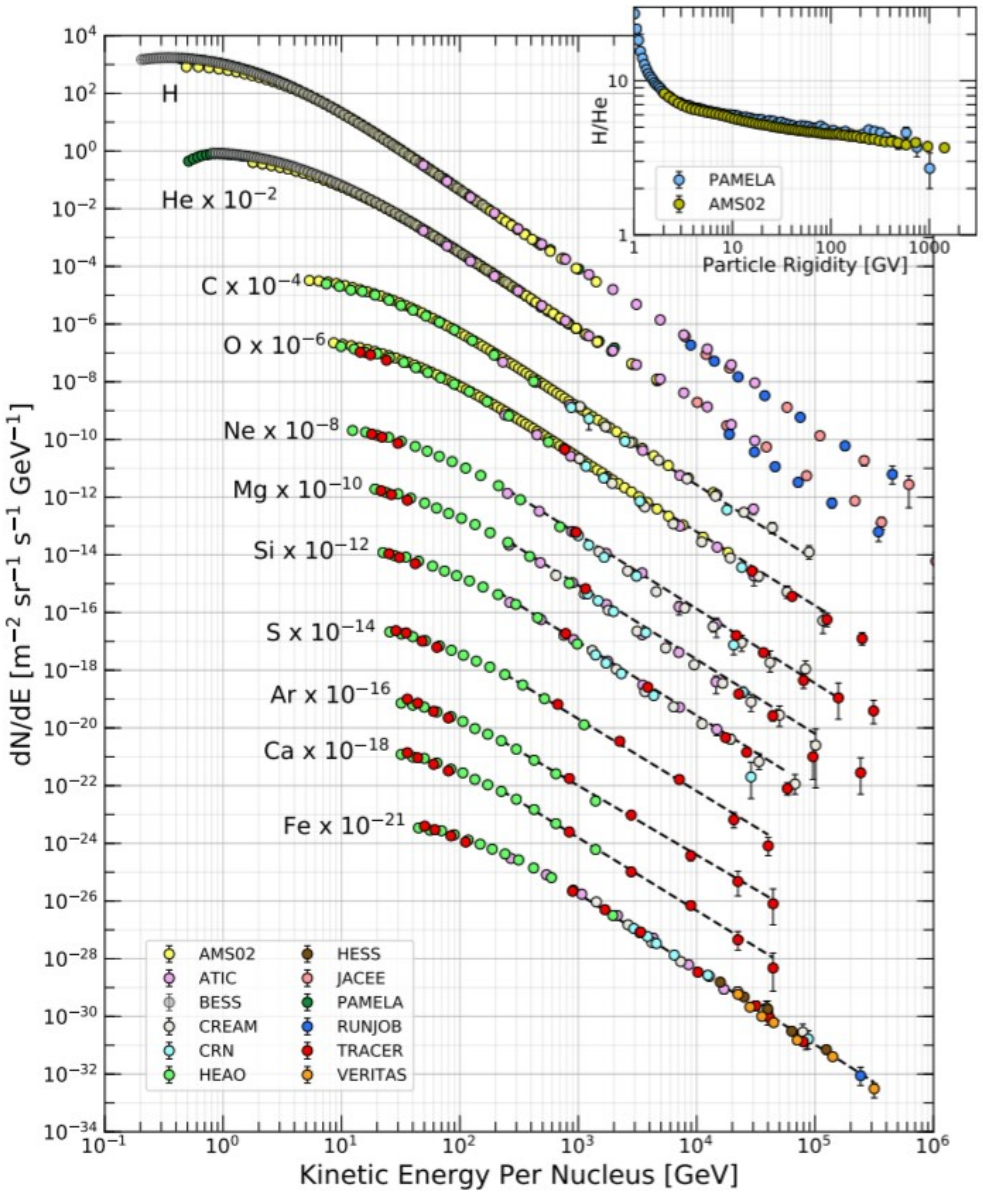

Figure 1.4: Fluxes of nuclei of the primary cosmic radiation expressed in particles per energy-per-nucleus are plotted vs energy-per-nucleus. The inset shows the H/He ratio as a function of rigidity. Figure taken from [8]

.

should convert part of the kinetic energy of material ejected by the SN into high energy particles: $P_{CR} = \eta P_{SN}^{kin}$, with efficiency $\eta = 0.01 - 0.1$. The particle energy gain in the first-order Fermi mechanism is $\sim (4/3)\beta$, where β is the ratio between the shock wave velocity and the particle velocity. This value of β is approximately what is required according to the mechanism suggested by Ginzburg and Syrovatskii [15].

- **Chemical abundances**: The composition of cosmic rays as measured by direct experiments, when the effects of propagation in the Galaxy are considered, is similar to the abundances of the elements in the Solar System and the chemical composition of the Solar System is similar to that produced by core-collapse supernovae.

- **Maximum energy**: The supernova model describes CRs with energy up to the *knee* and fixes the knee energy dependence on the atomic number, Z, of the considered nucles as, $E^{max}(Z) \simeq 300 \cdot Z$ TeV. A consequence of this model is that the chemical composition of CRs becomes heavier as the energy increases from values below to above the knee.

1.1.3 Extra-galactic CR sources

Active Galactic Nuclei (AGN) are the most powerful continuous sources of radiation in the Universe. A supermassive black hole (SMBH) is often present at the centre of galaxies. When fed with accreting matter, jets of particles and radiation can be emitted by the SMBH and the emission region around it becomes visible as an AGN. The AGN becomes even more luminous than its host galaxy if the emission is collimated in the line of sigth of the observer. A large variety of objects can be classified as AGNs. The unified model for AGNs [16, 17] explains the large variety of observed features considering that the same kind of objects can be seen from different angles. Because of the presence of emission jets and shocks in the galactic and extra-galactic medium, AGN can accelerate CRs to the most extreme energies. So far, no correlation between the arrival direction of ultra-high energy cosmic rays (UHECRs) and AGNs has been found [18].

Gamma Ray Bursts (GRBs) are cosmic events of short duration (ms to few minutes). They are characterised by an extremely bright γ-ray emission followed by an afterglow in X, UV and optical radiation. On the basis on the duration of the burst they are classified as "short" or "long". Short GRBs (below few seconds of duration) are believed to be originated by the merging of two neutron stars or of a neutron star and a black hole. Since compact objects are involved, this results in γ-ray emissions of short duration. Long GRBs can be produced by the collapse of extremely massive stars. In both cases the steady γ emission and the subsequent afterglow can be described with the fireball model [19]. The central engine, activated by a huge release of gravitational energy, can produce a jet of highly relativistic material, with Lorentz boost larger than 100 – 200. This jet

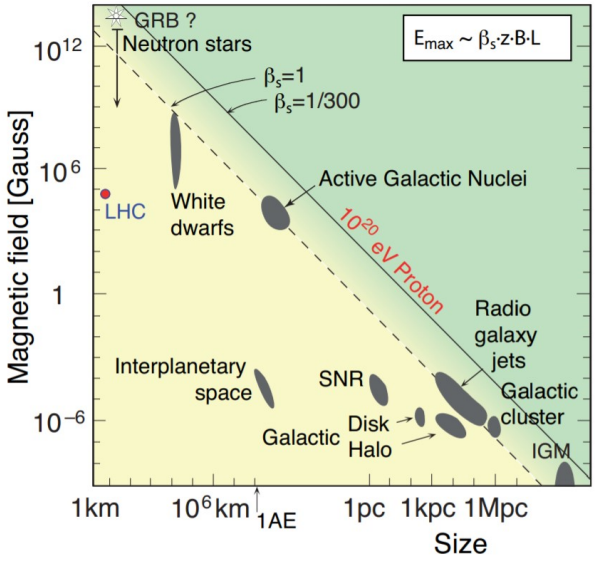

Figure 1.5: Hillas plot of astrophysical objects in which CRs could be accelerated. Plot extracted from [20].

moves through a dense environment producing shocks, emitting γ-rays by synchrotron processess and inverse Compton effect. The afterglow emission, at lower frequencies, is caused by the time-delayed interaction of the jet with the surrounding medium. Since large and extremely fast shocks are present, CR can be accelerated during GRB events. The high Lorentz boost of the shock can enhance the maximal energy of accelerated particles up to the highest end of the CR spectrum.

Hillas-plot

The relation between the energy that a cosmic ray can reach and the properties of its accelerator in terms of size and magnetic field can be graphically described in the so-called "Hillas plot" (Fig. 1.5). At a fixed size of the acceleration site, the higher the intensity of the magnetic field, the longer the CR is confined within its surrounding and can be further accelerated via Fermi mechanisms. At a given magnetic field intensity, the larger the site, the more encounters with the accelerating shocks are possible. Finally, a more compact object would require a higher magnetic field intensity to accelerate a CR to the same energy as a larger source. Moreover, the presence of a relativistic shock, with a Lorentz boost factor Γ, can produce a further enhancement of the CR energy.

1.1.4 CR measurement techniques and experiments

Direct CR measurements are usually performed with instrumentations and detectors on satellites and ballons. Due to load limitations, these experiments cannot be too large and thus fail at measuring the spectra of particles at very high energy/rigidity. For energies above a hundred of TeV, only indirect measurements of the CR flux are possible. They are based on the observation of the cascade of particles induced by CR interactions at the top of the atmosphere. Different technologies are exploited to measure the properties of the particle showers, during their development in the atmosphere, or at their arrival at the ground, or when they reach a certain depth or, also, with a combination of these measurements. Indirect measurements cover the energy range from 100 TeV to 100 EeV, but fail at identifying the nature of the CR nuclei on an event-by-event basis. It is however possible to obtain, by means of statistical methods and using Monte Carlo simulations, an estimation of the CR composition at the highest energy. In any case these measurements are largely dependent on the CR interaction model as well as on the systematic effects in the estimation of the CR properties. The results from the Pierre Auger Observatory suggest a heavier CR composition at the highest energies [21], even though some tension is present with the most recent results obtained by the Telescope Array Collaboration which prefer a lighter composition [22] above 10^{19} eV. At intermediate energies, around the knee region, several experiments have attempted to measure the composition on the basis of the shower topology and to perform per-particle spectral measurements; even though these measurements are strongly dependent on the hadronic interaction model considered, this has provided some hints on the behaviour of the CR compositions. In particular the KASCADE-Grande [23] and the ARGO-YBJ [24] have tested the composition of the CR spectrum around the knee and actually they find different spectral breaks for the light component. The LHAASO experiment [25] is expected to provide high-precision measurement of the CR spectrum in the knee region [26] while Auger-Prime [27] should improve the knowledge of the very-high energy region of CR spectrum.

1.2 Atmospheric neutrinos

When a CR reaches the top of the atmosphere, it penetrates it until it collides with an air nucleus. This usually happens at an altitude of about 10-20 km [3]. An extensive cascade of particles, showering down through the atmosphere, results from this interaction. The most abundant hadronic products are pions and kaons, neutral and charged. Neutral pion decays induce an electromagnetic cascade; charged mesons can decay leptonically.

These leptons, except for electrons that cannot go deep into water or ice, constitute the entirety of the atmospheric events that can be detected in a very large volume neutrino telescope (VLVνT) (Chapter 2), placed at large depths under sea, lake water, or ice.

Even though they represent the background to the cosmic searches to which VLVνT are devoted, these experiments can provide an insight into the study of atmospheric lepton fluxes and thus into CR physics. The flux of atmospheric neutrinos can be measured, from sub-GeV to few hundreds-TeV energies, with the current generation of neutrino detectors and, in particular, with VLVνT. The atmospheric neutrino flux is the convolution of the primary cosmic ray flux at the top of the atmosphere and the neutrino yield per primary particle. This yield is affected by several factors, mostly related to the efficiency in producing the mother particles of neutrinos, i.e. hadrons decaying into leptons. At a first approximation, the neutrino flux can be written as [3]:

$$\frac{d\Phi_\nu}{dE_\nu d\Omega}(E_\nu, \theta) = AE^{-\gamma_p} \sum_m \frac{B_m}{1 + \frac{c_m E_\nu}{\epsilon_m} \cos\theta} \tag{1.2}$$

where the first term $AE_\nu^{-\gamma_p}$ accounts for the primary CR spectrum with spectral index $-\gamma_p$. The sum then runs over the neutrino mother particles m: the coefficients B_m and c_m are related to the model describing the hadronic interaction. Finally, the term ϵ_m is the *critical energy*, for which the interaction length equals the decay length of the particle m; above this energy all the mother particles would interact before decaying, thus reducing the number of neutrinos at the highest energies and making the spectrum steeper. The description of the hadronic interactions both in the primary interaction and in the following development, is rather uncertain because they are low-transferred-momentum processes, not fully studied at accelerator experiments. Also the parton distribution functions used in the description of these interactions are affected by large uncertainties, both in the theoretical models and in the experimental results.

A review of the connection between hadronic interactions at high energies and the inclusive spectra of atmospheric leptons is reported in [32]. In particular, the energy spectrum of the primary nucleons that take part in the production of leptons at a fixed energy, is shown in Fig. 1.6. It can be seen that the primary cosmic ray nucleon energies peak at 10 times the lepton energy, with a long tail extending to the highest energies. The shape of these distributions show that there is a non negligible probability that the primary cosmic ray can carry significantly more energy than an observed lepton.

Different hadron species produce the majority of inclusive leptons and a summary is shown in Fig. 1.7. Here the contribution of each groups of mother particles that directly decay into muons and neutrinos as a function of the produced lepton is reported. As the energy increases, the decays of particles become suppressed above their critical energy. At energies above $\sim$ 100 GeV and up to 1 PeV, the main source of ν_μ are semi-leptonic and three-body decays of charged kaons, while the contributions from pion and muon decay dominate below 100 GeV. Concerning atmospheric ν_e, above 100 GeV and up to some tens of TeV, they come mostly from decays of neutral and charged kaons. These represent the *conventional* atmospheric neutrino flux for electron and muon neutrinos. At higher energy, shorter lived particles, with a mean lifetime approximately 5 to 6 orders

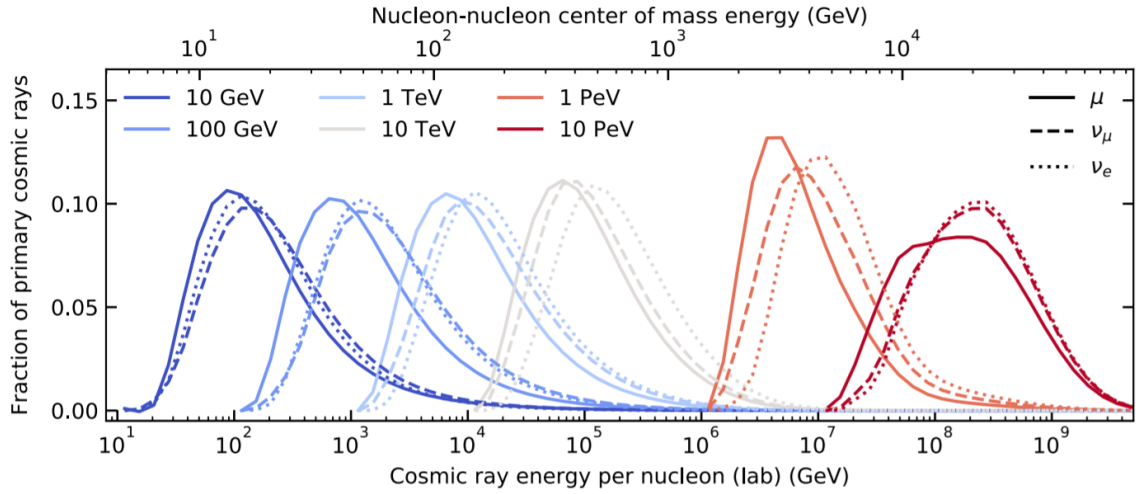

Figure 1.6: Probability density functions (PDFs) of the primary nucleon energies corresponding to inclusive leptons at a fixed energy (see the color code legend in the upper left). The solid, dashed and dotted lines refer to the individual lepton species (see top right legend). Atmospheric neutrinos up to 1 PeV probe center of mass collisions (top axis) that are within reach of current collider experiments (the LHC reaches 13 TeV). Figure taken from [32].

of magnitude smaller than pions and kaons, such as charmed hadrons start contributing to the overall flux, producing the harder *prompt* atmospheric neutrino component. Tau neutrinos are rare and are mainly produced by the decay of $D_s^+ \to \tau^+ + \nu_\tau$ and the subsequent decay of $\tau \to \nu_\tau + X$ and are not considered in the analysis.

In this thesis, the conventional component is described and implemented in the ANTARES Montecarlo simulation (Chapter 4.1) according to the calculations described in [34], while the prompt component follows the prescription reported in [35]. These evaluations of the atmospheric neutrino flux come from detailed simulations of the atmospheric shower development at a certain location, in order to account for the local intensity of the magnetic field which influences cosmic ray spectra at low energies.

1.3 Atmospheric neutrino measurements

Atmospheric neutrinos in the energy range from 100 MeV up to 100 PeV from an experimental point of view represent a continuous source of neutrinos. Underground experiments of the kton scale, designed in the 1980s to search for proton decay, started to measure atmospheric muon and electron neutrino charged current interactions. Two detection techniques were used: tracking iron calorimeters with a fine segmentation (such as Frejus [43], NUSEX [36] and Soudan 2 [37]) and water Cherenkov detectors, such as

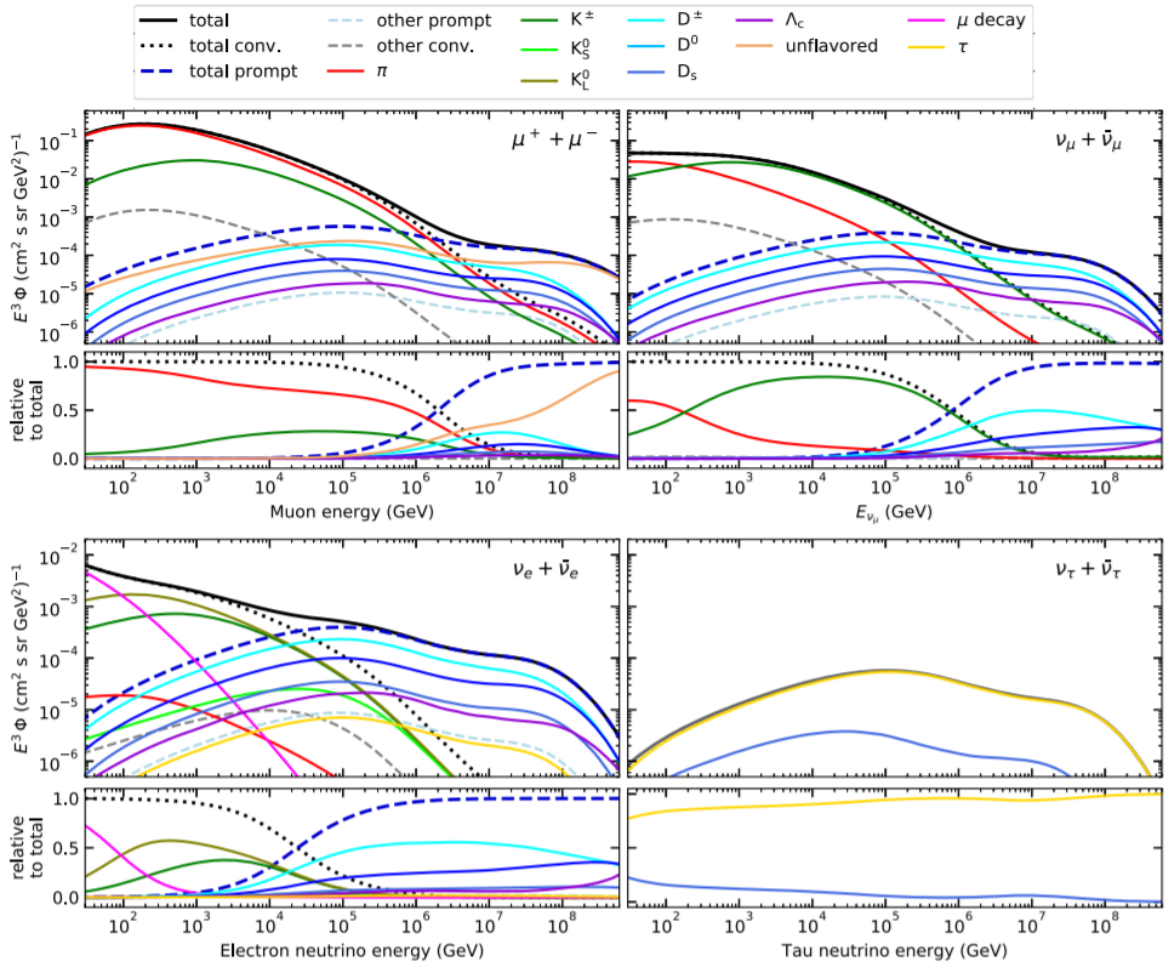

Figure 1.7: Groups of mother particles which contribute with their decay to the production of atmospheric μ (top left), ν_μ (top right), ν_e (bottom left) and ν_τ (bottom right). Figure taken from [32].

Kamiokande [39] and IMB [38]. The IMB and Kamiokande deficit of ν_μ-like events was the first indication for atmospheric neutrino oscillations and in 1998, Super-Kamiokande (SK) [40], MACRO [41], and Soudan 2 [37] in the same conference session in Japan presented new results with definitive indications of atmospheric neutrino oscillations. The Super-Kamiokande (SK) detector, located 1000m underground in the Kamioka mine in Japan, consists of a stainless steel tank filled with 50,000 tons of ultrapure water. The detector is divided into two regions: the inner region where 11,200 20-inches photomultipliers (PMTs) detect the light produced by the Cherenkov effect from charged particles produced in neutrino interactions; the external region which consists of a shielded volume for an anticoincidence veto for the rejection of the atmospheric muon background. Super-Kamiokande is the world's largest underground neutrino detector at the time this thesis is written.

In Fig. 1.8 the flux of electron and muon atmospheric neutrinos, measured by several experiments, is shown. Below 100 GeV the SK measurements [42] are by far most accurate both for electron and muon neutrinos, with respect those produced by Frejus in the past [43]. The discrepancy with the Frejus measurement below 1 GeV is due to the difference in geomagnetic cutoff at the Frejus site with respect to the SK one. At higher energies the ν_μ SK points overlap the AMANDA [44], ANTARES [49] and IceCube [45, 46] results. This type of detectors, called neutrino telescopes, are described in the next chapters. Concerning the ν_e neutrinos, the expected lower flux compared to ν_μ's makes the measurement challenging as the energy increases. Prior to this work, only IceCube produced measurements [47, 48] of the atmospheric ν_e neutrinos from 100 GeV and above.

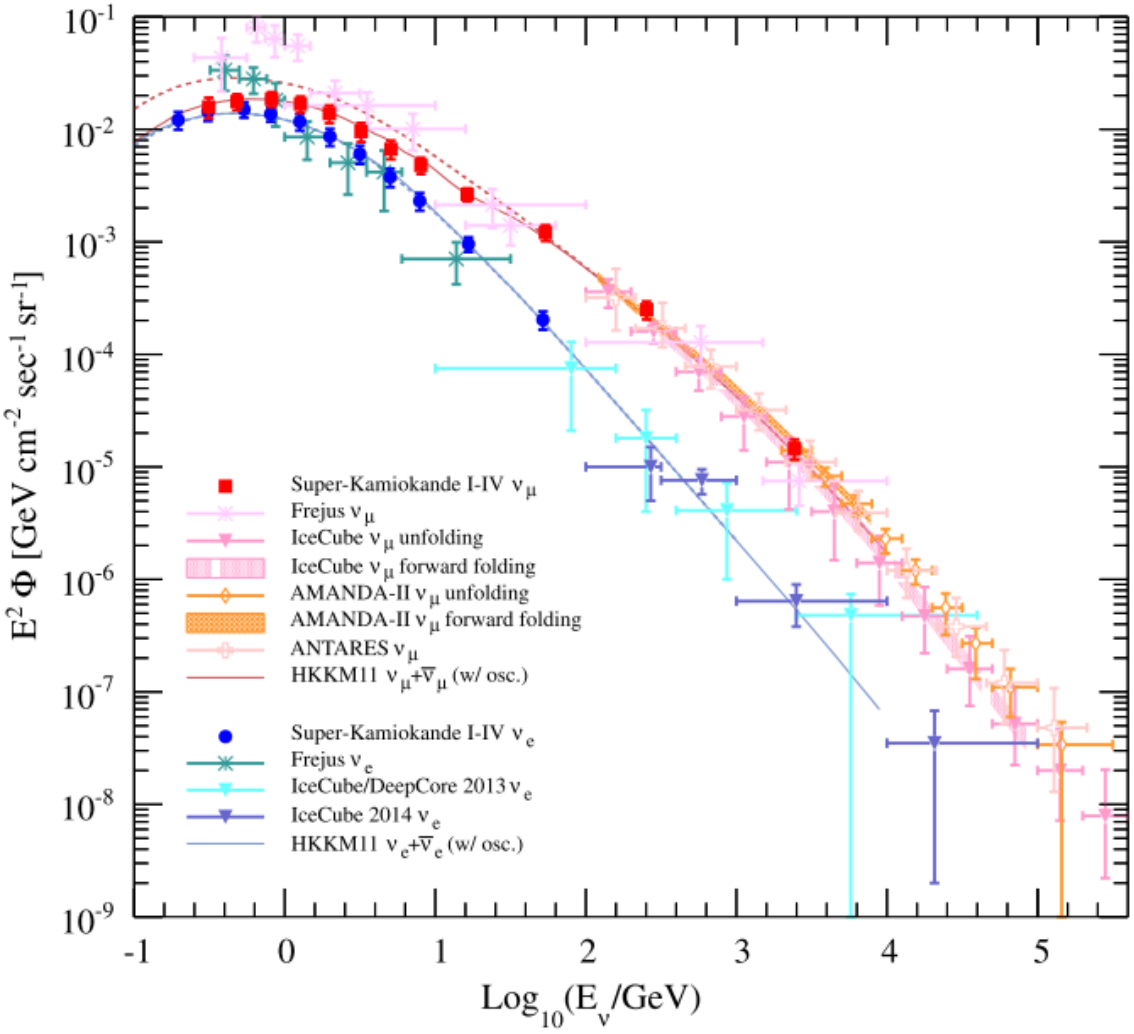

Figure 1.8: Measured atmospheric electron and muon neutrino flux by several experiments: Frejus [43], Super-K [42], AMANDA [44], IceCube [45, 46] and ANTARES [49]. The figures includes alto the HKKM11 flux model predictions [50]. Figure taken from [42].

2

Neutrino telescopes

Following the suggestion of Markov [51], a neutrino telescope is a 3-dimensional array of optical sensors, installed at a great depth under water or ice. These sensors can detect the Cherenkov photons produced by the products of neutrino interactions in the surroundings of the instrumented apparatus.

2.1 Neutrino interactions

Neutrinos only interact via *weak interactions* (W.I). W.I. have a short range and are mediated by the exchange of charged ($W^{\pm}$) and neutral (Z^0) massive bosons. The interactions between neutrinos and matter, depending on the mediator, can be classified in two types:

- *Neutral current (NC)*: The interaction is mediated by the neutral boson Z^0. The neutrino in the final state is identical (except for its momentum) to the incoming one and no charged lepton is produced. This can be represented by the reaction:

$$\nu_f + N \rightarrow \nu_f + X \tag{2.1}$$

  where ν_f is a neutrino of flavour f, N is a nucleon and X is a generic final hadronic state.

- *Charged current (CC)*: The interaction is mediated by the charged bosons $W^{\pm}$. In the final state a charged lepton with the same flavour of the interacting neutrino is produced:

$$\nu_l + N \rightarrow l^- + X \tag{2.2}$$

$$\overline{\nu}_l + N \rightarrow l^+ + X \tag{2.3}$$

The total cross-section for neutrino interactions, as a function of the interacting neutrino energy, is shown in figure 2.1. Neutrinos with energies of interest for neutrino telescopes ($E_\nu > 10$ GeV), can resolve the individual quark constituents of the nucleon. This reaction is called deep inelastic scattering and manifests itself in the creation of a hadronic shower.

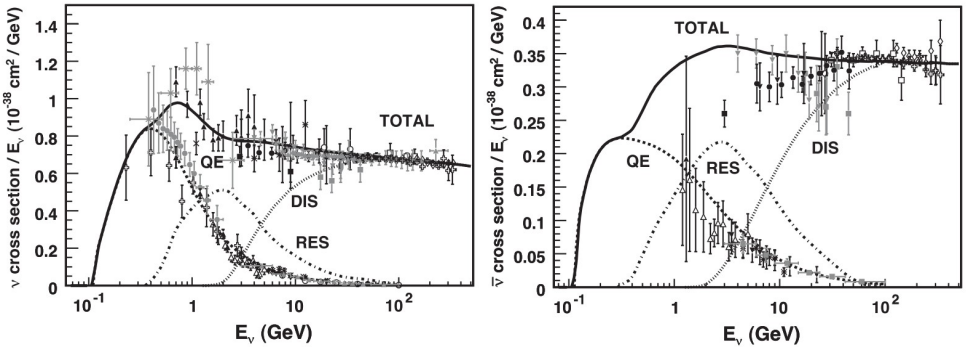

Figure 2.1: Total neutrino and antineutrino per nucleon CC cross-sections divided by neutrino energy and plotted as a function of energy. Points with markers present different measurements. Predictions for different contributions are shown: quasi-elastic scattering (dashed), resonance production (dot-dashed), and deep inelastic scattering (dotted). This figure is taken from [53].

2.2 Cherenkov light emission

CC and NC neutrino interactions can produce relativistic charged particles. When a charged particle travels faster than the speed of light in an insulator, Cherenkov [52] photons are emitted. Charged particles polarise the molecules along their trajectory and radiation is emitted when molecules depolarise.

This light is generated in a cone with a characteristic angle θ_c:

$$cos(\theta_c) = \frac{1}{\beta n} \tag{2.4}$$

$$\beta = \frac{v}{c} \tag{2.5}$$

where n is the refractive index of the insulator.

For highly relativistic particles ($\beta \approx 1$) in sea water ($n \approx 1.36$), the Cherenkov cone has an opening angle of about 42 degrees. The number of Cherenkov photons N emitted per unit wavelength interval $d\lambda$ and unit travelled distance dx by a charged particle of charge

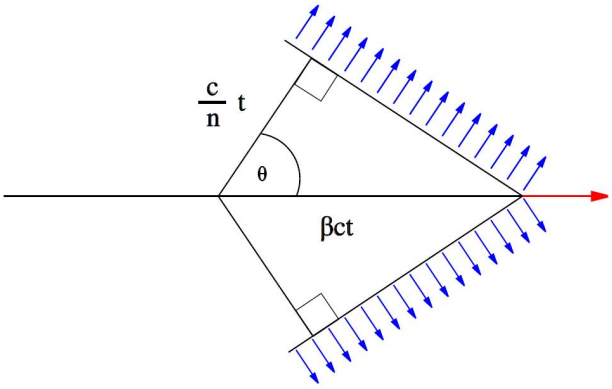

Figure 2.2: Illustration of the Cherenkov cone.

e is given by:

$$\frac{d^2N_\gamma}{dxd\lambda} = \frac{2\pi}{137\lambda^2} \cdot \left(1 - \frac{1}{n^2\beta^2}\right) \tag{2.6}$$

Cherenkov emission is mostly in the visible and UV wavelengths (300 ÷ 600 nm) and the mean number of Cherenkov photons emitted is about $3.5 \cdot 10^4\ m^{-1}$.

2.3 Physical background

Neutrino telescopes are not background free. Showers induced by interactions of cosmic rays with the Earth's atmosphere produce muons and neutrinos. Atmospheric muons can penetrate the atmosphere and up to several kilometres of ice/water as shown in figure 2.5. Neutrino detectors must be located deep under a large amount of shielding material in order to reduce the background. The flux of down-going atmospheric muons exceeds the flux of muons induced by atmospheric neutrino interactions by many orders of magnitude, though decreasing with increasing detector depth, as is shown in figure 2.3. In fact, neutrino telescopes typically look for upward going events, i.e. neutrinos that come from the opposite hemisphere with respect to the location of the detector. This significantly reduces the atmospheric muon backgroung thanks to the Earth shield to the latters.

2.4 Event topologies

Several event topologies can be observed in a neutrino telescope. In figure 2.4, according to the interacting neutrino flavour, the interaction channel and the observed interaction products, all the possible neutrino event topologies are represented. Among

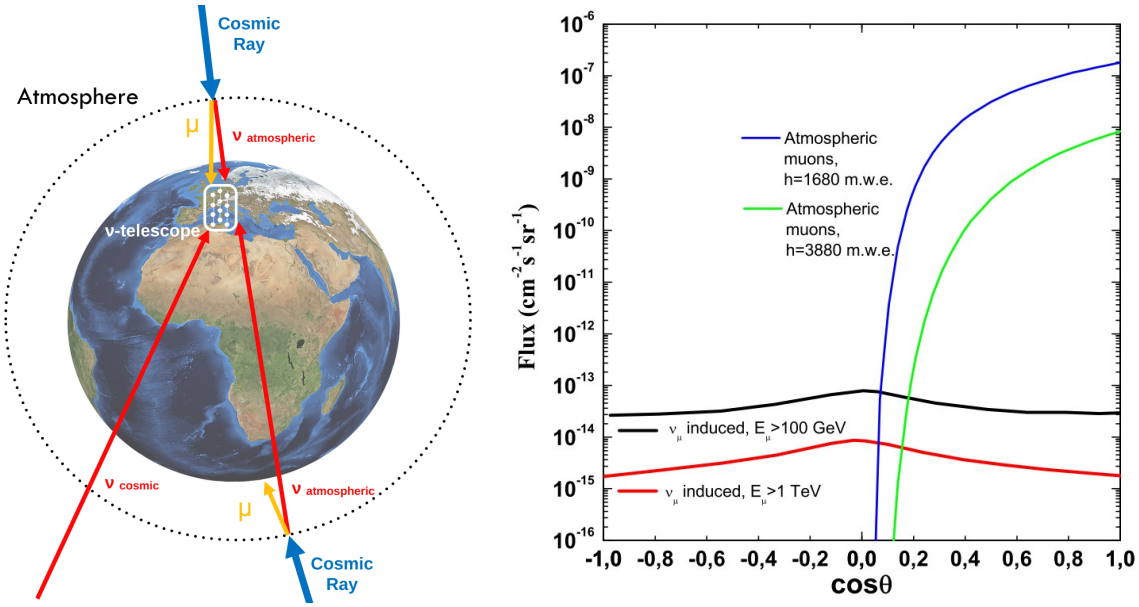

Figure 2.3: **Left**: Sketch of the muon and neutrino flux that can/cannot reach the location of a neutrino telescope. **Right**: Different contributions (as a function of the cosine of the zenith angle) of the atmospheric muons for two different depths and of the atmospheric neutrino induced muons, for two different muon energy thresholds.

them the three main event categories are: *track-events*, *shower-events* and *double-bang* events.

2.4.1 Track events

When a muon neutrino interacts via CC, a muon is produced. The Cherenkov photons emitted along the muon path allow the reconstruction of the muon track direction. Analogously the amount of the Cherenkov light emitted can be used to estimate the released energy. The angle between the muon and the neutrino directions is:

$$\theta_{\nu\mu} \approx \frac{0.6^o}{\sqrt{E_\nu}(TeV)} \tag{2.7}$$

and this channel provides the best pointing performance for a neutrino telescope. An event display of a track event observed by the ANTARES neutrino telescope is shown in figure 2.6 left.

Muons lose energy because of ionisation, bremsstrahlung, photo-nuclear interactions and pair production. The muon range, defined as the distance that the particle of energy E_μ, can travel before reaching the detection threshold E_μ^{thr}, ranges from a few hundred up to several thousand meters as shown in figure 2.5. This largely increases

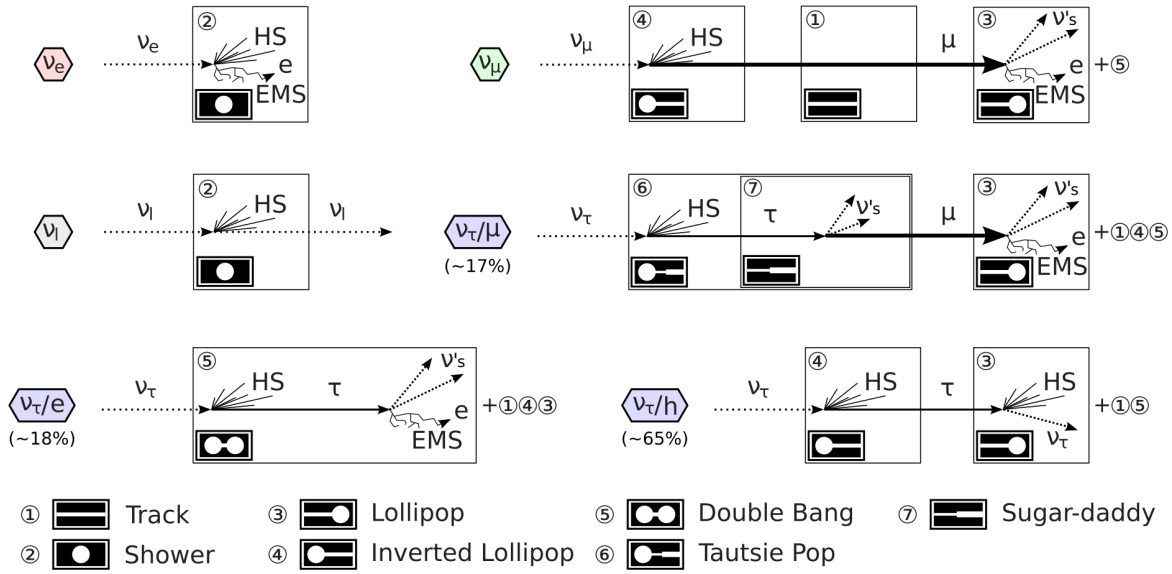

Figure 2.4: Types of events observed in neutrino telescopes depending on the type of interaction, incoming neutrino flavour and part of the interaction which is observed. HS denotes hadronic shower and EMS, electromagnetic shower. Figure adapted from Figure taken from [54].

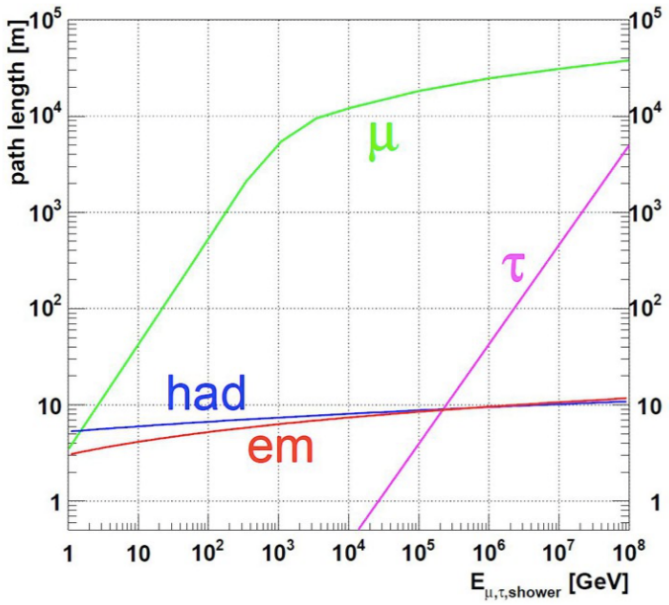

Figure 2.5: Longitudinal ranges of particles for different event topologies. The plot shows the range of muon and tau lepton tracks and the length of hadronic and electromagnetic cascades as function of the particle/shower energy. Figure taken from [55].

the effective volume of the detector since neutrino interactions happening far away from the instrumented volume can still be detected. As a consequence only part of the muon track is directly observed in the detector. This limits the capabilities of neutrino energy reconstruction for track-like events but increases the effective detection volume.

2.4.2 Shower events

Hadronic and electromagnetic showers are produced when a neutrino (of every flavour) interacts via NC or an electron neutrino interacts via CC. As long as the charged particles in the showers are above the Cherenkov threshold, light is emitted. The topology of a shower can be described as a function of its longitudinal and lateral extension.

An electromagnetic (EM) cascade is produced by a high-energy electron that radiates a photon via bremsstrahlung and the subsequent pair production reactions. It has a longitudinal extension of few meters and its lateral extension is negligible compared to the longitudinal one. Such a shower is small compared to the spacing between the PMTs in a neutrino telescope: EM showers represent to a good approximation a point-like source of Cherenkov photons. For this reason the angular resolution for shower events is worse with respect to that obtained for track events.

Hadronic showers, produced in NC interactions, show the same features as EM cascades, even though they are affected by more important event-by-event fluctuations.

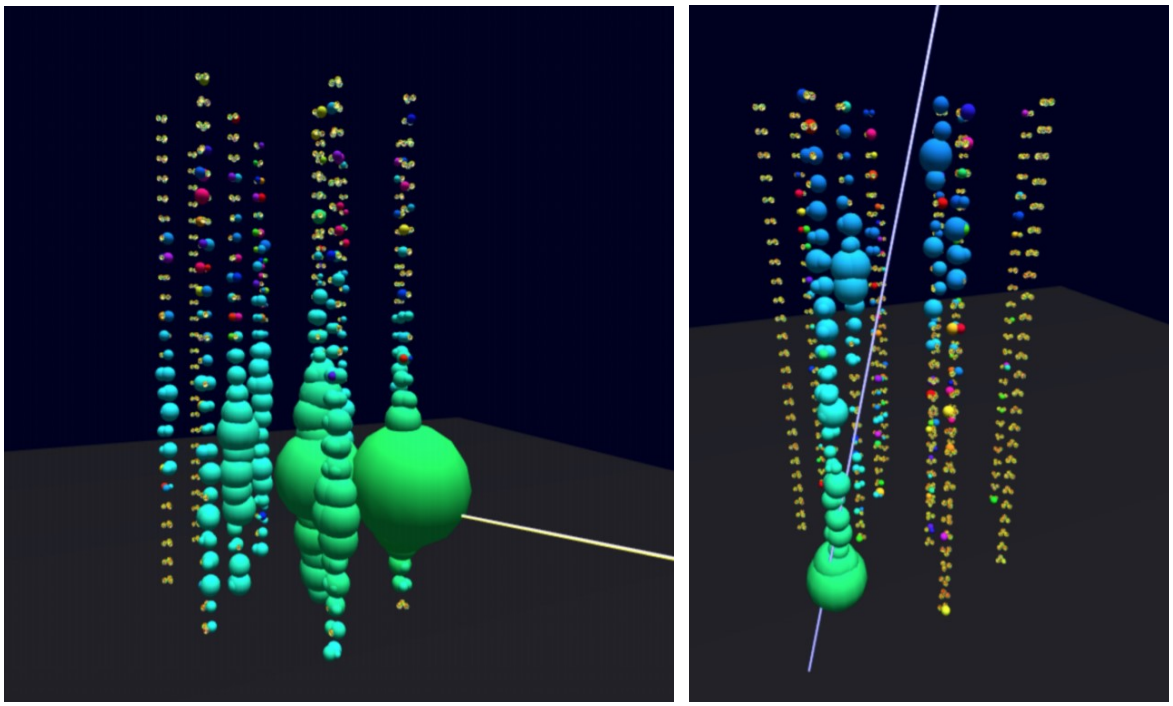

Figure 2.6: Event display of two events observed by the ANTARES neutrino telescope. The picture on the left shows a *shower-like* event topology and the right one shows a *track-like*. In both event displays, the size of the colored spheres represents the amount of photoelectrons collected on a PMT and the color code shows the arrival time of the photons. The straight lines that cross the detector indicate the reconstructed direction of the incoming neutrino.

The most common secondary particles in this kind of cascade are pions, kaons and nucleons. Muons produced in pion decays usually leave the shower producing few photons, so they contribute significantly to the fluctuations. Figure 2.5 shows that the longitudinal profile of hadronic showers is very similarly to the EM one. So, even if there are many possible differences between the two kinds of cascades, they are not distinguishable in large volume neutrino detectors.

Due to the fact that all the shower particles are contained within a few meters from the interaction vertex, all Cherenkov photons are emitted almost isotropically along the shower axis. For this reason a calorimetric measurement of the shower energy can be performed.

An event display of a shower event observed by the ANTARES neutrino telescope is shown in figure 2.6.

2.4.3 *Double-bang* events

When a tau neutrino interacts via CC, it produces a τ lepton. Taus have a short lifetime ($2.9 \cdot 10^{-13} s$) and decay producing various particles. This peculiarity allows the identification of τ events. In fact for large enough τ energies, the Lorentz factor can be large and the τ can produce a visible track before the decay. Overall, a shower is produced at the interaction vertex (first *bang*) and another one at the tau decay point (second *bang*), connected by a track-like signature. Such a *double bang* event can be observed in a large volume neutrino telescope only if the τ energy is in the order of 1 PeV or larger.

2.5 Current and future neutrino telescopes

Different options have been investigated for the construction of neutrino telescopes. The properties of water and ice of absorbing and scattering photons, significantly affect the performance of the detector in obtaining a high quality reconstruction of the neutrino properties. Neutrino telescopes can then be classified according to the medium in which they are immersed. In general, ice is more transparent than water but the presence of dust and trapped air bubbles causes a larger diffusion of photons and a degradation of the reconstruction performance.

An overview of past, present and future of neutrino telescopes, classified according to the medium and arranged chronologically, is presented in the following.

2.5.1 Under-water neutrino telescopes

Water, as a medium for high energy neutrino detection, was investigated either in the sea (or ocean) and in deep lake. The first project ever was DUMAND [56], conducted from 1976 until 1995 in the Pacific Ocean offshore Hawaii Islands at a depth of about 4800 m; all the subsequent projects took advantage of the experience coming from it.

BAIKAL GVD

A neutrino telescope has been built in the Lake Baikal, Russia, at a depth of $\sim$ 1800 m [57]. The first test detection units were deployed in the early nineties and, with these, it was possible to make a first search for high energy neutrinos [58]. Next generation cubic kilometer scale neutrino telescope Baikal-GVD (Gigaton Volume Detector) is currently under construction in Lake Baikal since 2015. The detector is specially designed to search for high energies neutrinos whose sources are not yet identified. The configuration of the telescope consists of functionally independent clusters of strings, which are connected to shore by individual electro-optical cables. Each cluster comprises 288 OMs arranged along 8 strings where seven peripheral strings are uniformly located at a 60 m distance around

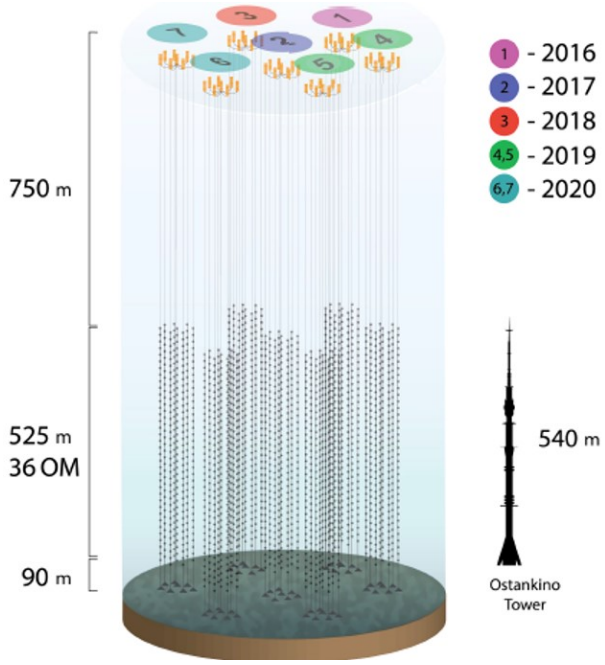

Figure 2.7: Baikal-GVD detector status in 2020 where 7 clusters, each comprised of 8 strings, are already functional. Figure courtesy of Olga Suvorova, member of the Baikal-GVD collaboration.

a central one. The distances between the central strings of neighboring clusters are about 300 m. In figure 2.7 a schematic view of the current configuration of the GVD detector is shown and in [59] the latest results obatined from the colleted data are reported.

ANTARES and KM3NeT

At the moment, the center of gravity of the research in under-water neutrino telescopes is the Mediterranean Sea. The presence of large abyssal planes, with depths ranging from 2500 to 4500m and low deep sea current favours this development. The ANTARES telescope [60], the detector on which this thesis is focused and described in details in the next chapter, is located at a depth of about 2500 m 40 km off-shore Toulon, France. This detector will take data until KM3NeT [61], the new generation neutrino telescope currently under construction, will exceed its size and performance.

KM3NeT is a research infrastructure comprising the ARCA and ORCA telescopes. The former will be located about 80 km off-shore from the coast of Portopalo di Capo Passero, Sicily, Italy, at a depth of 3500 m. The latter will be located at about 10 km far from the ANTARES site. The ARCA detector will have a final instrumented volume of more than 1 km^3 and is designed for the investigation of high energy neutrino astrophysics and the search for the sources of cosmic neutrinos. The ORCA detector is optimised

for the study of low energy neutrino oscillation physics and for the measurement of the neutrino mass hierarchy. This network follows a modular design made of building blocks (BB) of 115 strings. The different spacing between strings allows to target for different neutrino energies. In figure 2.8 are shown a schematic view of a BB and a string, together with a real picture of the fundamental light detection element the so-called Digital Optical Module (DOM). Each DOM consists of a glass sphere with a diameter of 17 inches which contains 31 PMTs with their corresponding readout electronics. The use of multiple PMTs per each DOM presents important advantages compared to the traditional use of one single PMT. The photocatode area increases by a factor 3. It also permits the identification of more than one photon arriving to the same DOM. This feature further allows a better rejection of the optical background, either due to bioluminescence or ^{40}K decay. Each DOM also contains a LED in the upper hemisphere for time calibration purposes, a compass/tiltmeter in order to determine the orientation of the DOM and an acoustic piezo sensor for positioning determination. A string or Detection Unit (DU) consists of 18 Digital Optical Modules connected via an electro-optical cable where information and power are transmitted. A buoy is placed on top of the string and together with a heavy anchor placed at the seabed, they keep the string in a vertical position underwater. In the anchor there is a key component of the string called Base Module (BM) that allows to exchange power and information, through an optical fiber circuit, from and to the string. At the moment the KM3NeT project is in its Phase-1 construction stage [61] but the modularity of the experiment design allows data to be taken as it is built. The most recent published results can be found in [62].

2.5.2 Under-ice neutrino telescope

The Antartic Ice shell has been exploited to build a neutrino telescope. Starting from the experience of the AMANDA [63] detector, its successor IceCube [64], depicted in figure 2.9, is currently the largest neutrino telescope in the world. It is located at the geographic South Pole, at the permanent Amudsen-Scott Pole Station. IceCube comprises an array of 5,160 Digital Optical Modules deployed on 86 strings at a depth of 1.5-2.5 km below the ice surface just above the bedrock in the clear, deep ice. High quantum efficiency PMTs are used in a denser sub-array located at the center of the detector. This sub-array, called DeepCore, enhances the sensitivity to low energy neutrinos, especially for neutrino oscillations studies. Finally, a surface CR detector, called IceTop, completes the IceCube Observatory. The total instrumented volume is about one cubic kilometre. The IceCube detector has achieved remarkable results in neutrino astronomy. In particular, it allowed the discovery of a diffuse flux of cosmic neutrinos [65, 66] and found first evidence for cosmic particle acceleration in the jet of an active galactic nucleus [67, 68]. The IceCube collaboration plans to expand the actual detector to next-generation instrument called IceCube-Gen2 [69]. This new detector aims at resolving the high-energy neutrino sky from TeV to EeV energies, investigating cosmic particle acceleration through multi-messenger

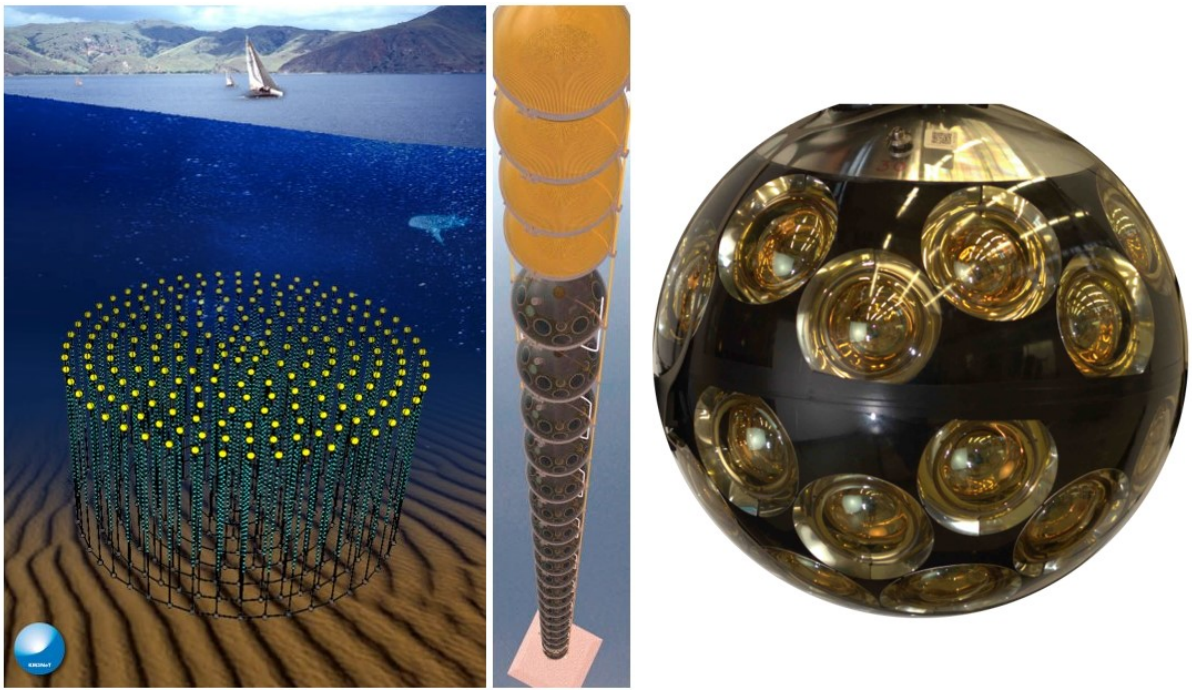

Figure 2.8: **Left**: artistic representation of a KM3NeT building block made of 115 strings; **Middle**; schematic view of a KM3NeT detection unit; **Right**; picture of a KM3NeT Digital Optical Module.

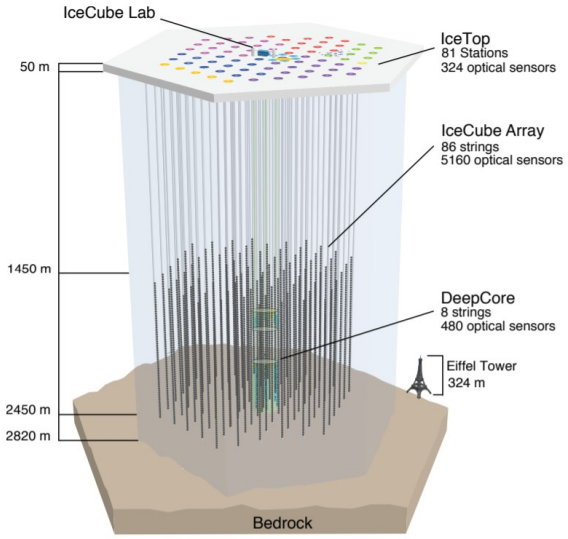

Figure 2.9: Schematic view of the IceCube detector taken from [64].

observations, revealing the sources of the highest energy particles in the universe and probing fundamental physics with high-energy neutrinos.

3

The ANTARES neutrino telescope

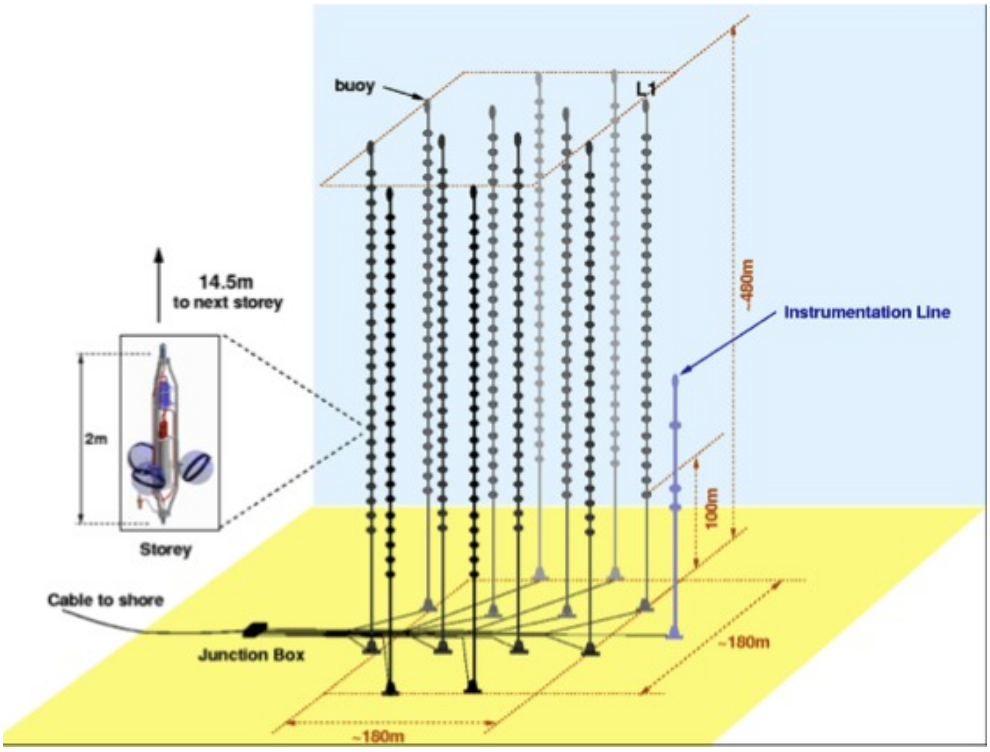

Figure 3.1: Schematic view of the ANTARES detector.

ANTARES (**A**stronomy with a **N**eutrino **T**elescope and **A**byss environmental **RES**earch) is the largest and longest operated undersea neutrino telescope in the Northern hemisphere. Its construction began in 2006 and it has been completed in 2008. It has been continuously taking data since then, and analysed data samples date back to 2007.

The ANTARES detector is located 40 km off-shore Toulon (see Fig. 3.2), France,

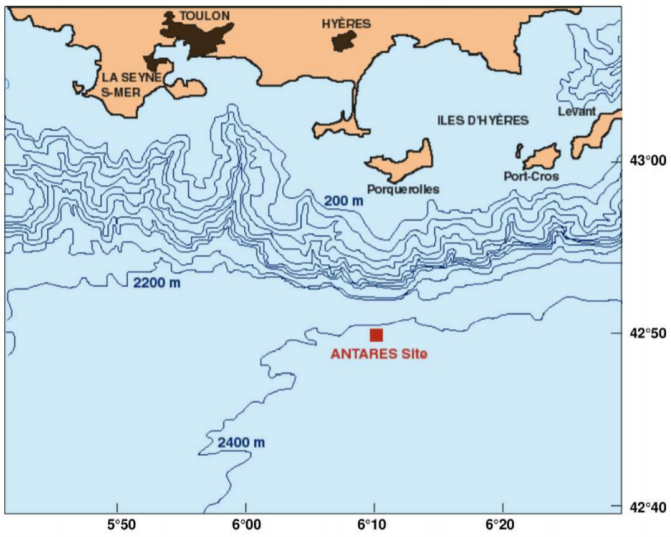

Figure 3.2: Map of the Mediterranean sea coast of Toulon, France. The red square shows the ANTARES position.

at a depth of 2475 m on the Mediterranean seabed. Its location makes it sensitive to neutrinos coming from a large part of the Southern sky, including the Galactic Centre region, which contains many interesting astrophysical objects.

3.1 Design

ANTARES is a 3-dimensional array of optical sensors [70]. It consists of 885 optical modules (OMs) distributed along 12 lines. Each line has 25 storeys, each storey consisting of a triplet of OMs with the only exception of the twelfth line, where the last sector (upper five storeys) is equipped with acoustic devices [71]. The arrangement of OMs in space, described in 3.1.3, was optimised by means of simulations in order to have the best neutrino detection efficiency. The telescope is connected to the shore station, located in La-Seyne-Sur-Mer, with a 40 km-long electro-optical cable that provides the power supply of the detector and guarantees the transmission from/to shore.

3.1.1 Optical module

The Optical module is a pressure resistant 17-inch diameter glass sphere that contains a photomultiplier (PMT) to detect Cherenkov light. The PMT model was chosen during the research and development phase of the ANTARES project [70]. A large detection area for each unit was required. Simulations showed that the geometrical area of the PMT should be larger than 500 cm^2 if a photocathode quantum efficiency larger than

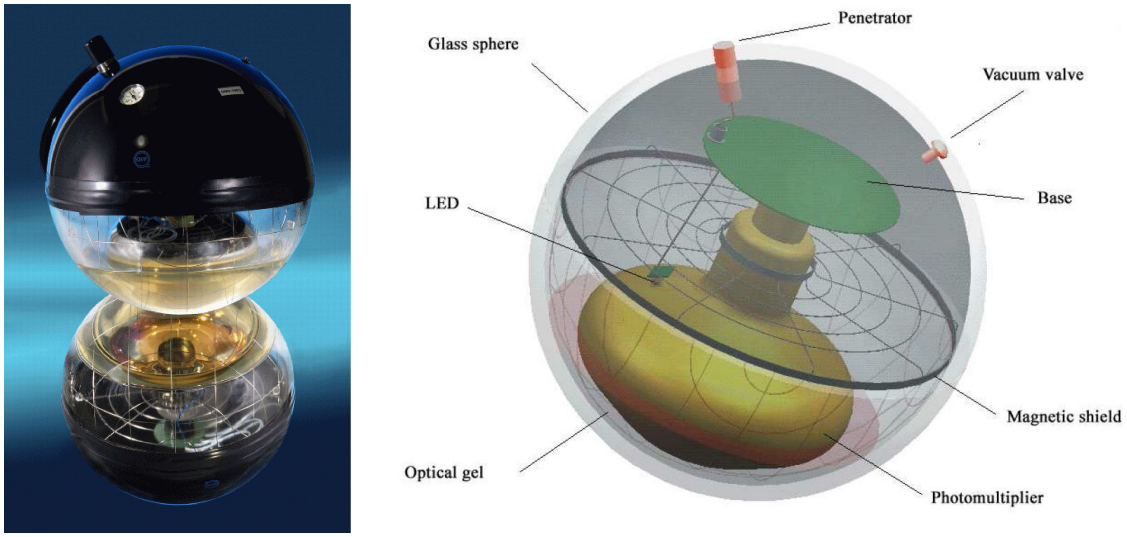

Figure 3.3: **Left**: Photo of an Optical Module. **Right**: Schematic view of the Optical Module.

20%, for the mean value of the Cherenkov light wavelength in water, is considered. The main requirements of the PMT are listed in table 3.1.1:

photocathode area	$\geq 500\ cm^2$
quantum efficiency	$\geq 20\ \%$
collection efficiency	$\geq 80\ \%$
TTS	< 3 ns
gain reached with HV $>$ 2000 V	$\geq 5 \cdot 10^7$

Table 3.1: Table of the main characteristics of ANTARES PMTs.

Eventually, a 10-inches photocathode diameter PMT (Hamamatsu R7081-20 model) was chosen, with a gain of about $5 \cdot 10^7$ at high-voltage (> 2000 V).

The PMT is enclosed in a borosilicate glass sphere, 41.7 cm large in inner diameter and 15 mm thick. The sphere is designed to withstand high pressures of about 260 atm during operation, and 700 atm during qualification tests. Its glass has a refractive index of 1.47 in the $300 \div 600$ nm range and the light transmission is larger than 95% above 350 nm, where the peak of Cherenkov photon emission is located. The influence of the Earth's magnetic field can degrade the transit time spread (< 3 ns FWHM) of the PMT: thus a $\mu - metal$ grid with high magnetic permeability is installed between the PMT and the glass sphere using an optical gel. The optical gel was chosen with an appropriate refraction index to reduce reflection. On the opposite side with respect to the PMT, an internal built-in LED is present. This is used for calibration purposes.

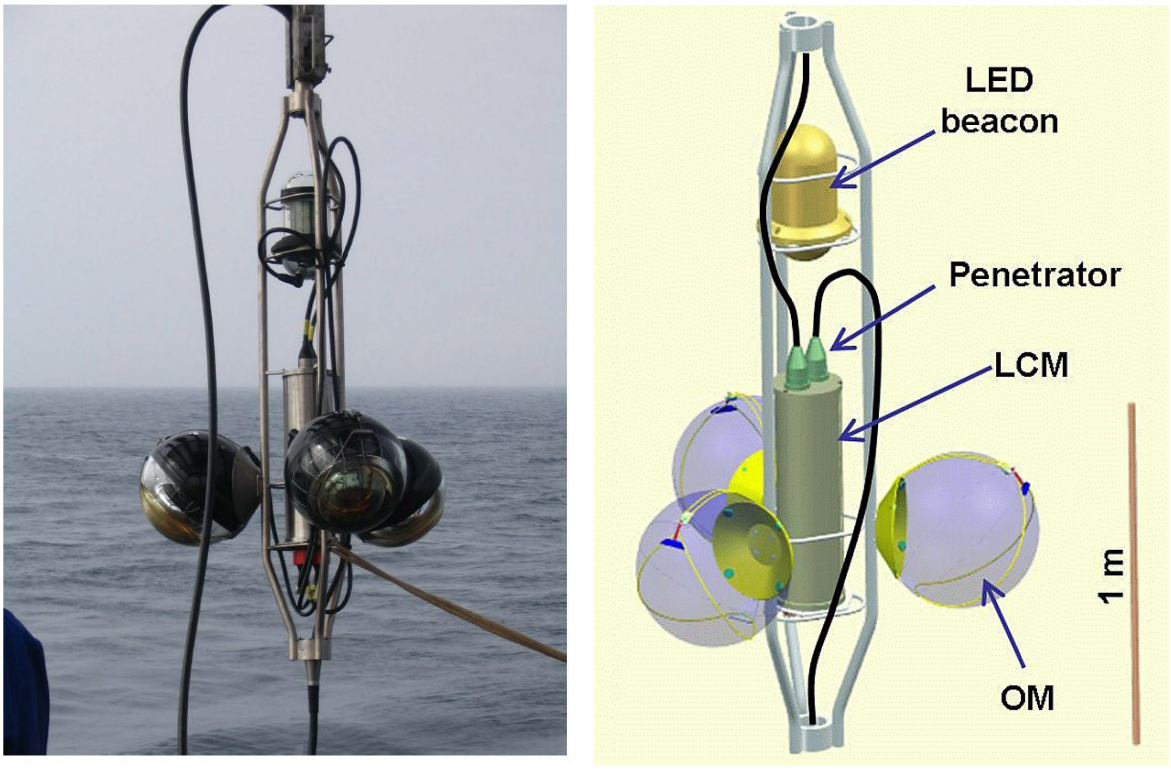

Figure 3.4: **Left**: Photo of a storey before the deployment. **Right**: Schematic view of the storey.

3.1.2 Storey

A storey is made of a triplet of OMs, a titanium container called Local Control Module (LCM) and additional instruments for the positioning and calibrations. The three OMs are equally spaced by 120^o in the azimuthal angle and facing 45^o downwards to increase the efficiency in the detection of upward-going particles. The LCM contains and protects the electronics from water, and is placed at the center of the storey. All the electronic boards are contained in the LCM, as well as the Slow Control (SC) instrumentation. The electronic boards control the distribution of the clock signal, the PMT HV supply and the readout of PMT signals.

The main electronic component is the Analogue Ring Sampler (ARS), which digitises, the signals coming from the OMs, providing information about their amplitude, arrival time and shape.

3.1.3 Line

A line is composed of 25 storeys equally spaced by 14.5 m and grouped in five sectors. It has a total length of ∼450 m. The lowest ∼100 m are not instrumented in order to avoid that, because of marine currents, material from the seabed could spread on the lowest OMs. The lines are anchored to the seabed by the Bottom String Socket (BSS) and held vertically using a buoy at the top of the line. The BSS contains the String Power Module (SPM), that controls the power supply to all instrumentation of the line. In each sector, a Master Local Control Module (MLCM) contains the Ethernet switch to control data distribution from the storeys of the sector. Two of the lines have in their BSS also a Laser Beacon used for time calibration.

3.1.4 The Junction Box and the electro-optical cable

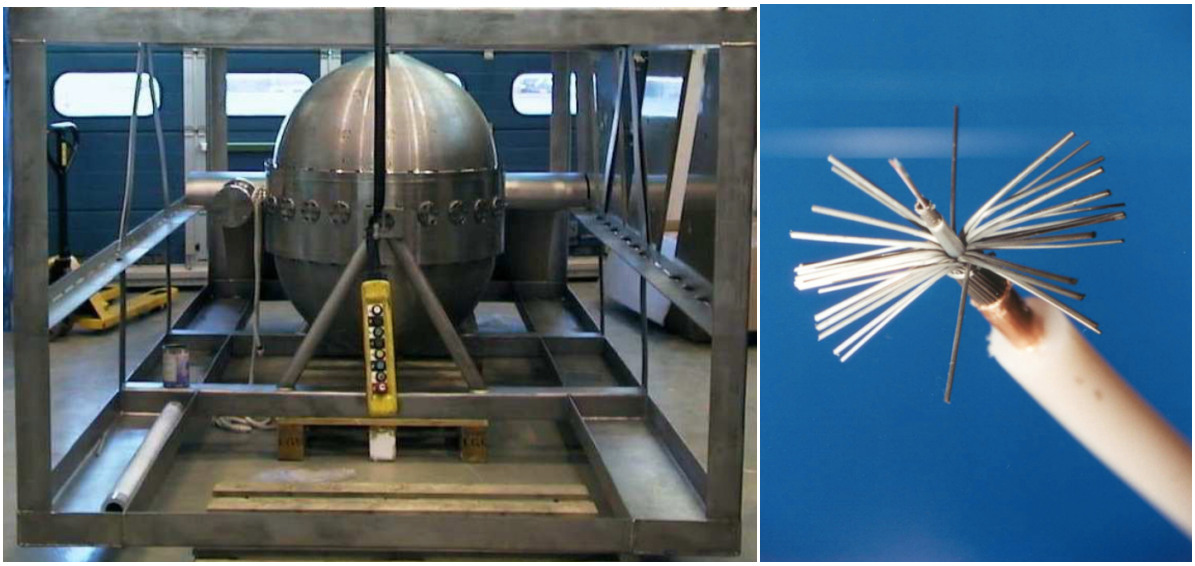

Figure 3.5: **Left**: Photo of the Junction Box. **Right**: Photo of the electro-optical cable end.

The shore station and the detector are connected by the 42 km long Main Electro-Optical Cable (MEOC). It is made of 48 monomode pure silica optical fibres and has a diameter of 50 mm. By means of this cable the data acquisition control commands, the clock signal and the power supply are distributed to the whole detector and/or to its specific components and data transmission to shore is ensured.

The MEOC arrives from shore at the Junction Box (JB), a titanium egg-shaped vessel. In the JB, the electrical and optical signals are split from the MEOC to the BSS of the lines. The junction box is responsible for the distribution of power, clock signal and

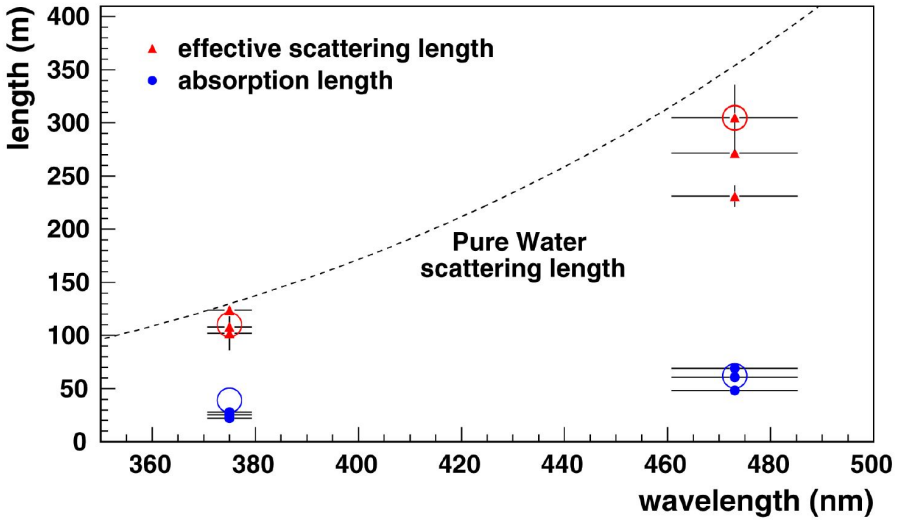

Figure 3.6: Water properties at the ANTARES site. The red and blue symbols represent the measured effective scattering and absorption length of light in water respectively at two different wavelength over different periods of time. The black dashed line shows, for comparison, the effective scattering length of light in pure water. Picture taken from [74].

data transmission to the BSS and of bi-directional communication between shore and the detector.

3.2 Water properties

The detector is located in deep sea water. Water is one of the main actors of the detector since it is both the target for neutrino interaction and mean of light propagation. The knowledge of the optical properties of sea water at the ANTARES site is extremely important to understand the response of the detector and to produce an accurate Monte Carlo simulation (chapter 4.1).

3.2.1 Light transmission

The transmission of light in water is characterised by the processes of absorption and scattering of photons. Absorption reduces the number of photons that reach the PMTs. Scattering changes the direction of photon propagation and the distribution of their arrival time, and this worsens the event reconstruction performances.

The propagation of light in a transparent medium is quantified, for a given wavelength λ, by the medium optical properties coefficients:

- the absorption: $a(\lambda)$

- the scattering: $b(\lambda)$
- the attenuation: $c(\lambda) = a(\lambda) + b(\lambda)$

Coefficients are defined so that, for each of them, a relative absorption, scattering and attenuation length is set. These lengths represent the path after which a beam of initial intensity I_0 and wavelength λ is reduced in intensity by a factor of $\frac{1}{e}$, according to the following relation:

$$L_i(\lambda) = i(\lambda)^{-1} \tag{3.1}$$

$$I_i(x, \lambda)) = I_0(\lambda)e^{-x/L_i(\lambda)};\ \text{i = a,b,c} \tag{3.2}$$

where x is the optical path (in meters) traversed by photons.
The measured value of the effective attenuation length for a wavelength of 466 nm, in the ANTARES site [74], is:

$$L_c(\lambda = 466nm) = 41 \pm 1(stat) \pm 1(syst)\ \text{[m]} \tag{3.3}$$

3.2.2 Biofouling and sedimentation

The presence, in the sea water, of particle sedimentation and biofouling on the OMs can reduce the light transmission through the glass sphere. These effects on the ANTARES optical modules have been studied in [75]. The experimental setup consisted of two glass spheres similar to those used for the OMs. One of them was equipped with five photo-detectors glued to the inner surface of the sphere at different inclinations zenith angles illuminated by two blue light LEDs contained in the second sphere. The loss of transparency, shown in figure 3.7, in the equatorial region of the OM is about 2% after one year, then shows some saturation effect.

3.2.3 Bioluminescence and ^{40}K background

Optical background in sea water is characterised by two components:

- decays of radioactive element;
- bioluminescence;

The radioactive background is dominated by the ^{40}K decays:

$$^{40}K \rightarrow ^{40}\ Ca + e^- + \overline{\nu}_e \tag{3.4}$$

$$^{40}K + e^- \rightarrow ^{40}\ Ar + \nu_e + \gamma \tag{3.5}$$

In the first channel, the electrons are often above the Cherenkov threshold hence, if the ^{40}K decays close to an OM, some light can be detected. The γ in reaction 3.5, has an

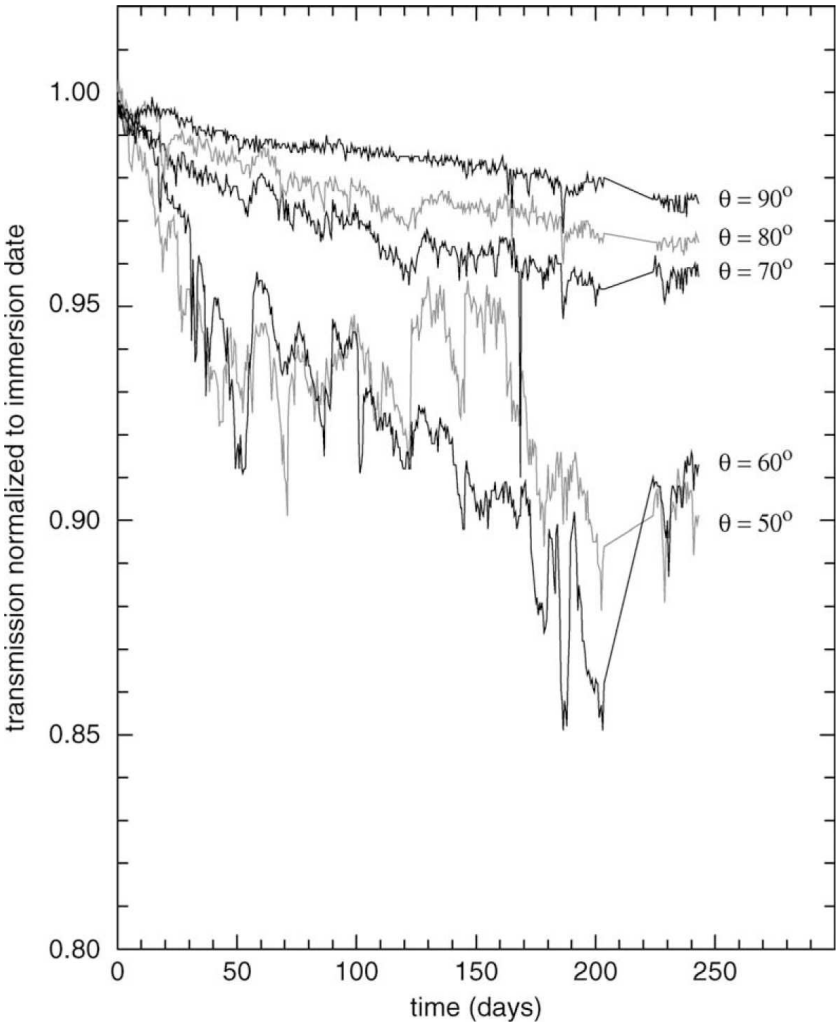

Figure 3.7: Light transmission as a function of time at the ANTARES site. Different curves correspond to different angular position along the device surface. Details can be found in [75].

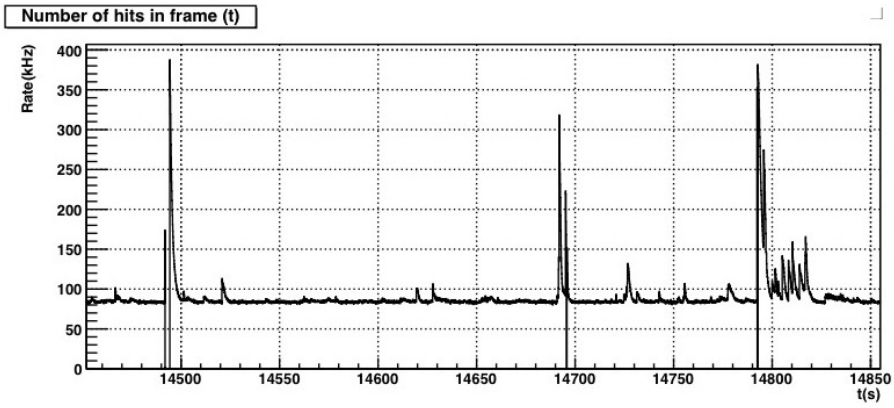

Figure 3.8: Median measured rate evolution on a OM.

energy of 1.46 MeV and can induce electrons above the Cherenkov threshold via Compton scattering. The intensity of this background is related to the salinity of water, which is almost constant in all the Mediterranean Sea. The mean single rates from ^{40}K decays is around 80 kHz on a single PMT.

Besides the quite constant baseline due to ^{40}K decays the luminescence produced by living organisms, the so-called bioluminescence, is also present. This background is found everywhere in oceans and there are two sources in deep sea: steady glowing bacteria and flashes produced by marine animals. The bioluminescence appears as a flat background and bursts, as shown in figure 3.8.

Seasonal effects in bioluminescence are also present and they reach their maximal intensity during spring where $\sim$ MHz single rates on PMTs can be detected. During these periods the detector may be switched-off to avoid damage to the electronics of PMTs.

3.3 Data acquisition

The ANTARES data acquisition system (DAQ) relies on the *all data to shore* paradigm. All signals induced by photons above a certain thresholds are digitised and sent to the on-shore control station. Dedicated trigger algorithms filter the data stream looking for potentially interesting events and store them onto disk.

3.3.1 Offshore DAQ

The data acquisition system converts the analog signal from each PMT in a suitable format for the data analysis [72]. The main part of the system, the Front End Module, is located off shore, in the LCM, and is connected to the two Analog Ring Samplers (ARS) coupled to each PMT [73]. The ARS is a customised chip, working in a token ring

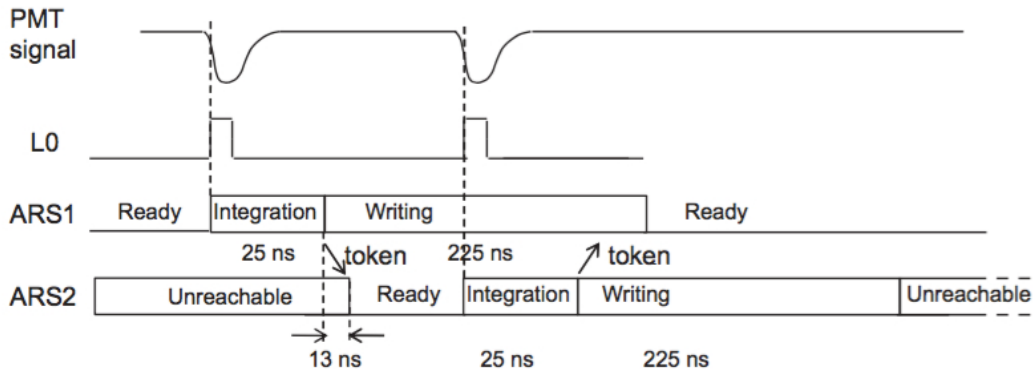

Figure 3.9: Working scheme of the Analogue Ring Samplers (ARS).

protocol for the digitisation of the analogue signals from the PMTs as shown in figure 3.9. The ARS has a charge threshold usually set at 0.3 photo-electrons to avoid spurious signals from dark currents, and integrates the PMT signal over a time window of about 30 ns. At the end of the integration window, the ARS enters a dead time of about 200 ns. After a token transmission time of about 13 ns, the second ARS starts looking for further signals over threshold and follows the same acquisition scheme. The time and charge information is digitised and constitute a *hit*, the fundamental information quantum of each event detected by ANTARES. This data acquisition step is called *level-0* trigger, and the hits recorded at this stage are called *L0-hits*.

3.3.2 Onshore DAQ and Triggering

The onshore DAQ system handles a data stream that goes from 0.3 to 1 GB/s, depending on the light rate on the PMTs. A farm of CPUs located at the onshore control station filters the data to identify the hits resulting from physical events (atmospheric muons and neutrinos) and rejects the hits related to the optical noise. This filtering stage is done using two levels of triggers that tag the so-called *L1-hits* and *L2-hits*. Both trigger levels are based on causality criteria with respect to the position of detected hits and their arrival time. Following the *L1* and *L2* hits definitions:

- ***L1-hits***: defined as the occurrence of two or more hits from optical modules on the same storey, within a 20 ns time-window. Also hits with a high charge (tipically > 3 p.e.) are classified as *L1-hits*. Two *L1-hits* (i and j) are considered causally related by imposing the following condition:

$$|t_i - t_j| \leq |\vec{r}_i - \vec{r}_j| \cdot v_g + 20\ ns \tag{3.6}$$

  where t_i and t_j are the arrival times, $\vec{r}_i$ and $\vec{r}_j$ the position of the corresponding OM and v_g is the group velocity of light in water. The inclusion of the 20 ns delay takes

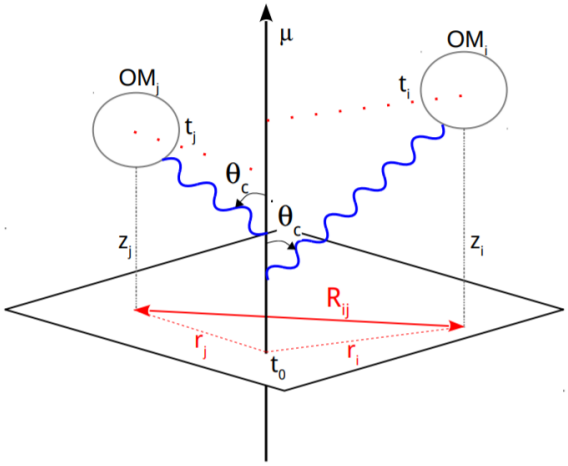

Figure 3.10: Parameters used to define the causal relation between two *L0-hits* in the 3N trigger.

into account potential scattering of the photons and time calibration uncertainties. A triggered event is defined when a number (typically ≥ 5) of causally correlated *L1-hits* are found. In this case, all the *L0-hits* within 2.2 μs before and after the first and last *L1-hits* participating in the trigger are written onto disk. The time-window just mentioned is easily interpreted as roughly the time needed for a muon to cross the detector.

- ***L2-hits***: Two high-level triggers are defined in the ANTARES DAQ chain:
  - **T3 trigger**: it requires *L1-hit* coincidences on adjacent or next-to-adjacent storeys of the same line within a time window respectively of 100 ns (adjacent) and 200 ns (next-to-adjacent). A more selective version of this trigger, called **2T3**, is used where two T3 clusters of hits are required within a time-window of 2.2 μs.
  - **3N**: this trigger relies on the assumption that the hits are produced by a muon *track-event*. The algorithm looks for hits that can result from the same track, imposing the condition:

$$|t_i - t_j| \leq \frac{|z_i - z_j|}{c} + \frac{R_{ij}}{c} tan(\theta_c) + 20\ ns \tag{3.7}$$

    where the symbols are defined in figure 3.10.

3.4 Calibrations

The physical analyses using ANTARES data require high-level information for each event such as the reconstructed direction of the interacting neutrino or its estimated energy. This information is provided by reconstruction algorithms which use time, position and charge of the hits. A dedicated detector calibration procedure is carried out for all these parameters.

- **Position calibrations**: even if the ANTARES lines are kept vertical by a buoy they can move (change their inclination and rotation) with the sea current. The position calibrations are necessary to know the OMs positions in the space. Hydrophones are mounted on storeys 1, 8, 14, 20 and 25 of each line. Acoustic transceivers are installed at the bottom of each line and an additional one located at a distance of 145 m from the detector. Measuring the time between an acoustic emission and detection allows to know the position of each OM with an accuracy better than 10 cm.

- **Time calibrations**: inside each OM a LED is hosted that send light to the photocatode. Using the LED, a light source with a known emission time, is possible to measure the time resolution of each OM can be measured. On average this time resolution is $\simeq 1.3$ ns and it is mainly due to the transit time of the photomultiplier tubes. To measure the relative time offset between two OMs, two laser beacons mounted at the bottom of the lines 7 and 8 and optical beacons on storeys 2, 9, 15 and 21 of each line are available. The optical beacons are used to measure the time offsets between OMs belonging to line while the laser beacons are used for inter-line time offsets.

- **Charge calibrations**: to compute the relation between the number of photo-electrons and the measured amplitude of each PMT several measurements were done before the deployment of the detector components. These measurements provided a linear relation between the p.e. and the amplitude, for a number of p.e. below 20. Above this value the readout electronics saturates and no discrimination of the charge is possible.

3.5 Data quality

The ANTARES data taking is organized in runs, usually lasting between six and twelve hours. In figure 3.11 the run duration for the data sample considered in this analysis is shown.

Several quantities are computed to characterize the data taking quality of each run. Following two of these quantities, namely the number of active OMs and the *baseline*, are described and represented for the entire period analyzed for the subject of this thesis.

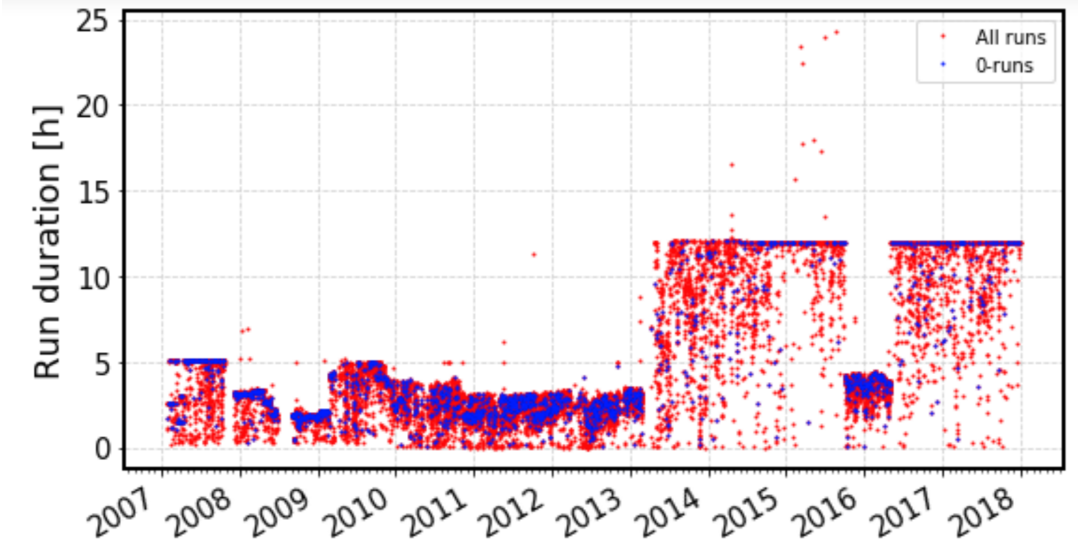

Figure 3.11: Run duration for the ANTARES 2007-2017 data sample. The blue dots represent the *0-runs* sample and the red one the whole data sample.

x

Active OMs

The ANTARES detector works in a continuously data taking regime along the year but, given its modularity, it can work even if one or more optical modules stop operating. Figure 3.12 shows the total number of optical modules operating as a function of time.

Baseline

Together with the status of the detection elements it is important to monitor the environmental conditions in which the detector is immersed, the deep seawater.

The *baseline* is defined as the average hit rate counting during a data acquisition run, for each PMTs. This parameter allows to evaluate the stability of the luminous background generated by biological activity which is added to the constant luminous background generated by the ^{40}K decay.

As can be seen in figure 3.13 there have been periods of high bioluminescence, mainly near spring, but in recent years this effect has mitigated and the quality of the data taking has improved from this point of view.

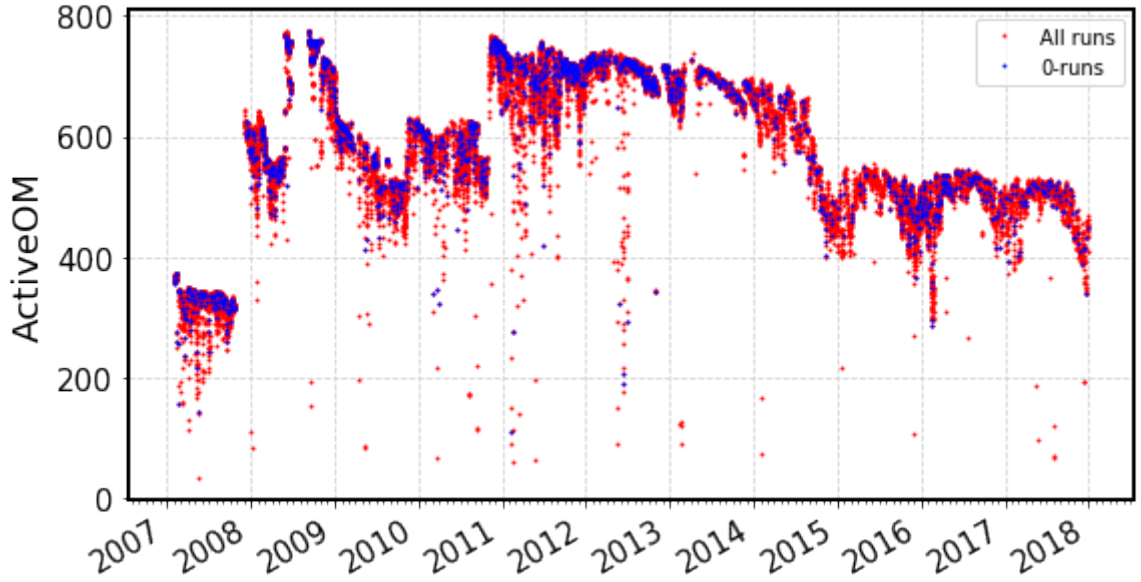

Figure 3.12: Active OMs for the ANTARES 2007-2017 data sample. The blue dots come from the *0-runs* sample and the red one from the whole data sample.

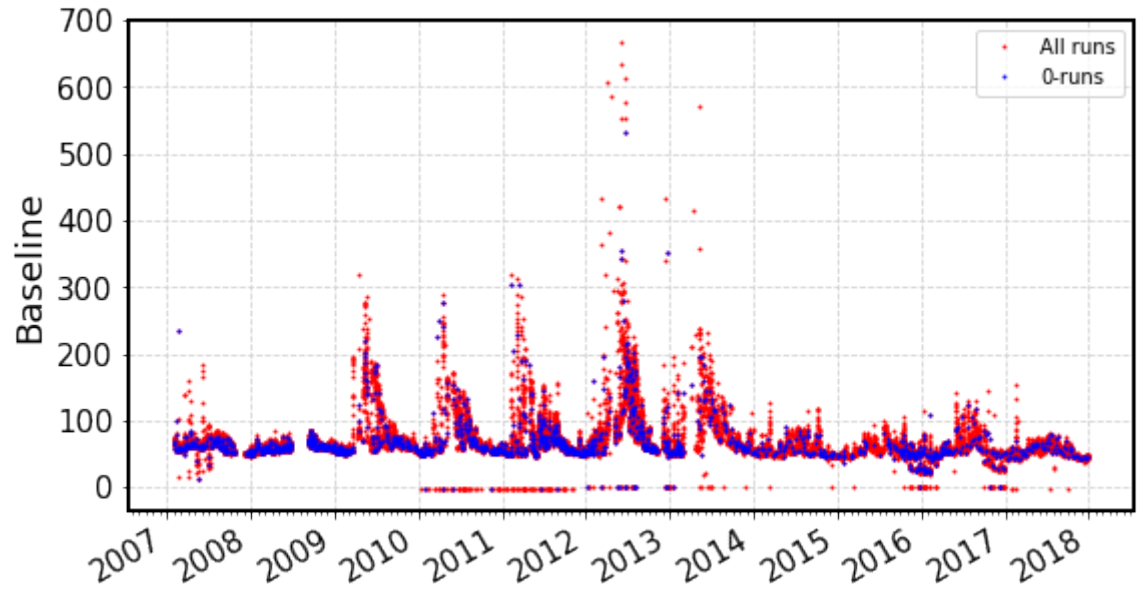

Figure 3.13: Baseline for the ANTARES 2007-2017 data sample. The blue dots come from the *0-runs* sample and the red one from the whole data sample.

4 Analysis tools

In this chapter, the software tools used in the analysis are described, where [77] has been used as introduction. At first the Monte Carlo (MC) simulation chain is presented, then the reconstruction algorithms used in the analysis are discussed. At the end the multivariate analysis method, developed by the TMVA project [78] and used for the last stage of the event selection is described.

4.1 Monte Carlo simulation

Monte Carlo simulations are required in any high-energy physics experiment to understand the behaviour of the detector and its physics potential. The Monte Carlo chain developed for the ANTARES experiment can be schematized into three main parts:

1. *Event generation.*
2. *Particles and light propagation.*
3. *Detector response simulation.*

Neutrino and atmospheric muon events are generated in the proximity of the detector, then they are propagated through the medium, Cherenkov light emission is simulated and photons are propagated to the OMs, taking into account also the PMTs response. Finally the data stream is built, the optical background is added and the DAQ electronics and triggers are simulated.

Detector *"can"*

Around all the PMTs a larger virtual cylinder, called the *can* is defined, which represents the active volume of the detector. It exceeds the instrumented volume, defined as the minimun cylinder that contains all the PMTs, by $\sim$ 200 m which corresponds

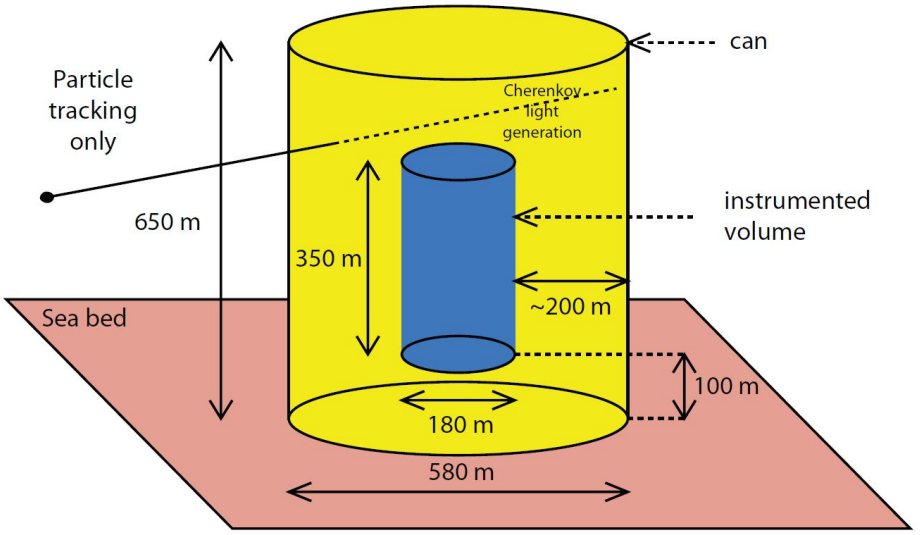

Figure 4.1: Definition of the ANTARES can. The can is built by extending the instrumented volume by three attenuation lengths (∼200 m), except from below where it is bounded by the sea bed from which no Cherenkov light can emerge.

to about three light absorption lengths in the water. In the simulation chain, outside this volume, only the particle energy losses are considered for particle propagation while inside the *can* the Cerenkov light is generated and propagated.

4.1.1 Event generation

Neutrinos

The dedicated GENHEN package [79] is suitable for Monte Carlo simulations over the full range of energy for neutrino studies in ANTARES, from neutrino oscillations to high-energy astrophysics, the majority of detected neutrinos in a range of energies from tens of GeV, limited by the energy threshold of muon detection at around 10 GeV, to multi-PeV, where the absorption of neutrinos in the Earth strongly attenuates the upward neutrino flux. To limit the influence of simulation uncertainties there are several general requirements that must be satisfied. Neutrinos interacting both inside the can (volume events) and outside the can (surface events) should be simulated in the same package in the correct proportion. For events inside the can, the production of the hadronic shower at the interaction vertex must be simulated, as charged secondary particles can contribute to the total amount of observed Cherenkov light. For events outside the can, high energy muons must be tracked until they stop or reach the surface of the can. The effect of the different media (rock and water) around the detector must be taken into account in

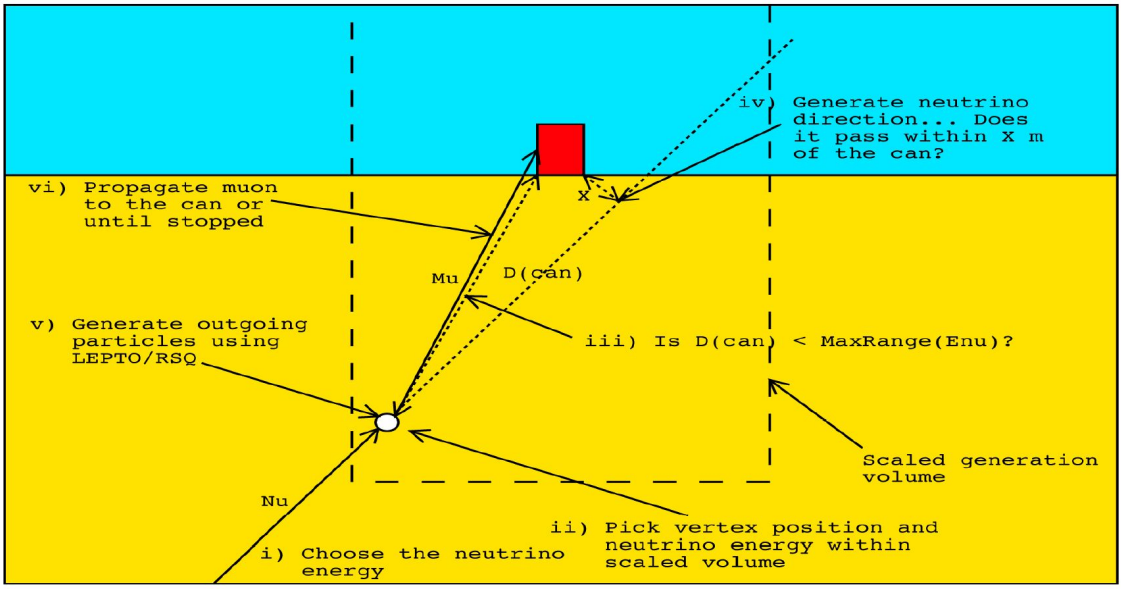

Figure 4.2: Schematic overview of the event generator algorithm GENHEN.

both the neutrino interactions and muon propagation. For high energy neutrinos, the probability of absorption in the Earth must be calculated given the neutrino interaction cross-section and an Earth density profile. A power law, $E^{-\gamma}$, is chosen for the generation spectrum of the neutrino interactions (which will be refered to as the "interacting neutrino spectrum" in the following description). This can then be weighted to different neutrino fluxes to give the event rates for specific models. Figure 4.2 schematically shows the neutrino production procedure.

The general simulation method foresees the definition of a volume around the detector which contains all potentially observable neutrino interactions for the given energy range. For neutrino interactions outside the can, any produced muon is then propagated and stored if it reaches the surface of the can. To get meaningful statistics after the muon propagation step, e.g. a few thousand muons at or within the can, it is typically necessary to simulate some billions of neutrino interactions. Clearly, the simulation time required to completely process this number of events would be very CPU time demanding. The largest possible muon energy in the simulation corresponds to the upper limit on the neutrino energies specified by the user, E_{max}. Hence, the maximum muon range at this energy is R_{max}. No neutrino interacting further away from the detector can produce a muon reaching the active volume. Hence we can use these distances to define our total simulation volume. Starting with this information, the full simulation then proceeds as follows: first a cylindrical volume around the instrumented volume of the detector of radius R_{max} is defined and the energy interval chosen by the user (between E_{min} and E_{max}) is subdivided into a user-defined number of equal divisions in $\log_{10}(E_\nu/\mathrm{GeV})$. For

each bin, all the relevant interaction processes are considered and simulated using the LEPTO [80] package and the number of events N to generate is calculated. Finally the loop over the number of events to generate in this volume starts and goes through the following steps:

- The energy of the interacting neutrino is sampled from the E^{γ} spectrum within the energy range of this bin.
- The neutrino position is chosen within the scaled volume.
- Whether or not the vertex is inside the can is determined. If it is outside, the shortest distance from the neutrino vertex position to the can is calculated. If this distance is greater than the maximum muon range at that neutrino energy, no muon produced by this neutrino will ever reach the can and the event is rejected with no further processing.
- The neutrino direction is sampled from an isotropic distribution. For events outside the can, it is calculated whether the distance of closest approach of the neutrino direction to the can is greater than some user specified distance.
- For each event, the neutrino interaction is simulated using the appropriate code to get the final state particles at the neutrino interaction vertex.
- For events inside the can, all these particles are recorded (position, direction, energy, etc) for further processing. For events outside the can, only the muons are kept.
- For those events which are kept, the "event weights" are calculated and event information is written on disk.

At the end, a record of each neutrino interaction producing at least one particle at or inside the can is obtained.

Event weighting

Assigning a weight to each simulated event, it is possible to reproduce any spectrum defined according to a model, and calculate the actual rates at the detector. Given a differential flux $\phi(E_\nu, \theta_\nu)$, the *global* weight is:

$$w_{global} = w_{gen} \cdot \phi(E_\nu, \theta_\nu) \tag{4.1}$$

where w_{gen} is the generation weight defined as:

$$w_{gen} = \frac{V_{gen} \cdot \rho N_A \cdot \sigma(E_\nu) \cdot P_{Earth}(E;\theta) \cdot I_\theta \cdot I_E \cdot E^{\gamma} \cdot F}{N_{total}} \tag{4.2}$$

- V_{gen} $[m^3]$: Generation volume;
- ρN_A: Product of the target density ρ for the Avogadro's number N_A that gives the number of target nucleons per unit volume;
- $\sigma(E_\nu)$ $[m^2]$: Total cross-section, as a function of the neutrino energy E_ν;
- $P_{Earth}(E_\nu; \theta_\nu)$: Survival probability for a neutrino crossing the Earth;
- I_θ $[sr] = 2\pi(cos\theta_{max} - cos\theta_{min})$: Angular phase factor depending on the range of $cos\theta_\nu$. It is the integral of the solid angle.
- I_E: Energy phase space factor depending on the input spectral index γ for the neutrino interaction rate. It is the integral of the energy spectrum between the minimum and maximum energy used in the generation.
- F: Number of seconds in one year.
- N_{total}: Total number of generated events.

Atmospheric muons

Cosmic rays interacting in the upper atmosphere produce extensive air showers that contain high energy muons. Although the ANTARES telescope is located at large depth under the sea, and exploits the shielding effect of water, the atmospheric muon flux at the detector is still very intense. An accurate simulation of this signal is mandatory to study the residual contamination of wrongly reconstructed tracks and to use the atmospheric muon tracks for calibrating the detector and testing the analysis software. Two possible approaches to the simulation of atmospheric muon bundles exist:

- *Complete simulation*: It is performed using dedicated software packages, as for example CORSIKA [81], that simulates extensive air showers starting from the first interaction of the primary particle and following the development of the shower through the atmosphere.
- *Parametric simulation*: This approach allows the fast production of an extremely large number of events being based on the use of parametric formulas that describe the multiplicity of the muon bundle, the distance of each muon from the shower axis and their energy spectrum within each event. The main drawback of this approach is the lack of flexibility in the choice of interaction and composition models.

In ANTARES, atmospheric muon bundles are generated using the MUPAGE software [83]. This is based on the parameterisation of the energy and multiplicity distribution of the muons inside a bundle. The parameterisation [84] has been built using a complete

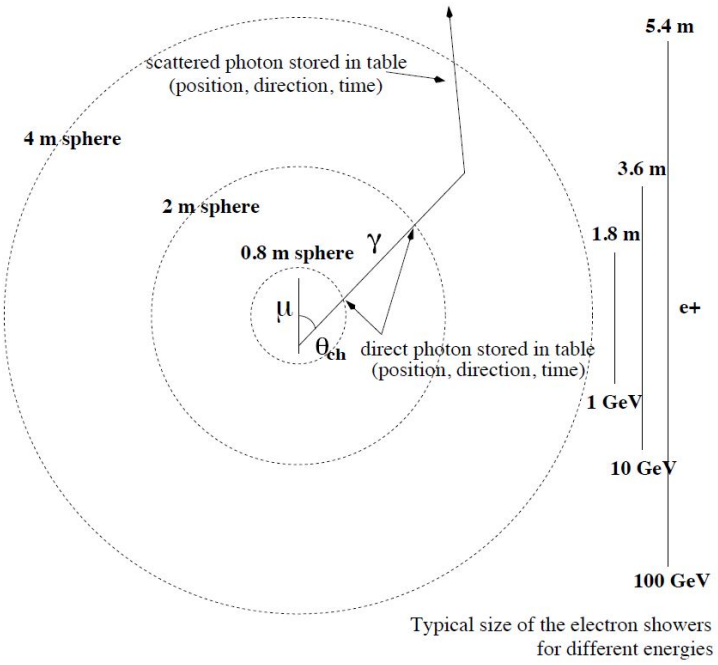

Figure 4.3: Schematic overview of the particles and light propagation.

simulation, performed with the HEMAS software, and considering a composition model obtained by the MACRO experiment at the Gran Sasso laboratories [85]. MUPAGE allows the production of atmospheric muons between 0° and 85° in zenith angle and covering the entire range and energy relevant for a neutrino telescope.

4.1.2 Particles and light propagation

All long-lived particles produced in neutrino interactions are tracked through the can volume using a package called KM3 (a GEANT-based software developed in the ANTARES context). The properties of the sea water, density and optical parameters, like scattering and absorption lengths of the light, are considered. Muons propagation through the can volume is done with the software MUSIC [86]. The tracks are propagated in steps of 1 meter, taking into account all the relevant physics processes, like energy loss, multiple scattering, radiative processes and hadronic interactions. Thanks to the homogeneity of sea water, a set of *scattering tables*, containing the probability of each photon to give a hit on a PMT as a function of 5 parameters is built. The parameters that are taken into account are:

- The distance of the OM from the muon track.
- The photon arrival time.

- 3 angles defining the direction of the photons with respect to the muon track and the PMT.

Similar scattering tables are created for electromagnetic showers. To have a reliable and fast simulation of the light produced in hadronic showers, the light production of each hadron is considered equivalent to that of an electron according to appropriate weight defined depending on the properties of each particle (*multi particle approximation*).

4.1.3 Detector response simulation and trigger

The detector response is simulated with the *TriggerEfficiency* program. This software, developed specifically for ANTARES, adds the hits due to the optical background to the hits coming from the event, then simulates the effect of the electronics and the trigger of events.

The first step adds to the MC events a fixed background rate specified by the user or taken from a real data run, according to a Poisson distribution. When real data are used in the run-by-run strategy, the program adds to the PMTs a background corresponding to what is measured in real data. This allows to consider not only the constant ^{40}K contribution, but also the optical background due to the biological activity that can vary depending on the season.

The electronics simulation reproduces the front-end board acquisition as described in Ref. [82]. In order to simulate the time resolution, which is $\sim$ 1.3 ns for single photo-electron signals and decreases for higher amplitudes, the hit times are smeared using a Gaussian function with a width of $\frac{1.3ns}{\sqrt{N_\gamma}}$, where N_γ is the number of simultaneously detected photons. Analogously the hit amplitude is simulated by smearing the integrated number of photons with an empirical function that produces a (roughly Gaussian) smearing. The defined hits are then processed with a trigger algorithm.

4.1.4 Run-by-run strategy

The Monte Carlo simulation strategy used for ANTARES is the so called *run-by-run* (rbr) [87]. For every physics run an analogous MC run is produced using the TriggerEfficiency option that takes information from the data files and use it in the processing of the physics output of the Monte Carlo chain. This approach is used to take into account the variability of the conditions in a marine environment and their effect on the data acquisition. In particular the biological and physical phenomena that affect the measured rates show an evolving trend both in seasonal (long term) and daily (short term) time scale. Also, a temporary or permanent malfunctioning of a PMT is considered in this way. Finally, different triggers acting during a specific data acquisition run are considered.

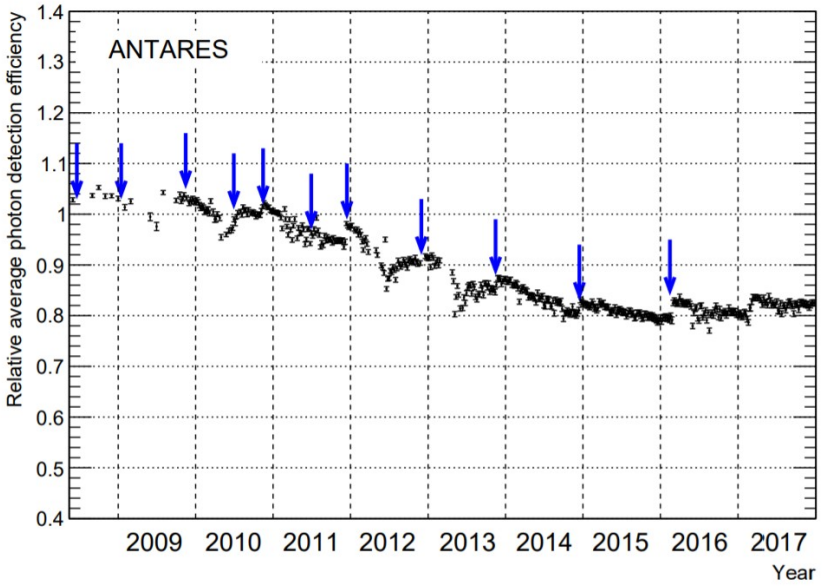

Figure 4.4: OM efficiency as a function of time, averaged over the hole detector. The blue arrows indicate a high voltage tuning of the PMTs. Figure taken from [88].

4.1.5 Detector ageing in Monte Carlo simulation

ANTARES is located in the sea depths and has been taking data since more than 10 years. The PMT aging, along with possible other environmental effects, such as biofouling and sedimentation, are expected to affect the optical modules detection efficiency. The variation of the detection efficiency of the optical modules along the data taking period, has been studied in detail in order to reproduce correctly the event rate with MC simulations. A dedicated analysis [88] has been performed using the measurements of the ^{40}K decay rate as reference. The signal from the ^{40}K decay is considered is constant and stable in time. In figure 4.4 the OM efficiency relative to the value measured as a function of time, averaged over the whole detector is presented. The figure shows how the relative detection efficiency decreased by about 20% in the first period and then saturated and remained constant. In the ANTARES Monte Carlo simulation, these ageing effects are taken into account thanks to the trigger efficiency program which allows the user to apply an efficiency coefficient to each PMT for each run. Thanks to the aforementioned analysis based on the ^{40}K decay, monthly tables were produced in which the efficiency of each PMT is calculated and than applied to the rbr simulation.

4.2 Reconstruction algorithms

In a neutrino telescope an event is basically a set of triggered hits detected by the PMTs, associated to a position, a time and a charge related to the number of photo-electrons that have been detected. Two main topologies of events are defined in sec. 2.4: the so-called *track events* (sec. 2.4.1) and the *shower events* (sec. 2.4.2). Triggered events must be reconstructed to obtain the physics quantities that are required for the analysis like the energy of the event, which is a proxy of the parent neutrino energy and the direction of the parent interacting neutrinos. For each topology, several reconstruction algorithms have been developed. In the following, the shower and track reconstruction algorithms used in this thesis are presented.

4.2.1 Shower-like event reconstruction

TANTRA

The TANTRA algorithm (**T**ino's **ANT**ARES Shower **R**econstruction **A**lgorithm) [89] reconstructs the direction and the energy of *shower-like* events. This reconstruction strategy has been developed for the search of neutrino point-source described in [90]. The reconstruction is performed according to the following steps:

1. Position hit selection: the set of hits, causally compatible with a common source of emission, with the largest sum of associated charge is selected.
2. Position reconstruction: a 4-dimensional linear least squares pre-fit for the shower space-time position is performed, whose result is used as input to an M-estimator fit.
3. Shower hit selection: hits that are compatible with the fitted position within a user-defined time residual window are selected.
4. Shower direction reconstruction: a probability density function (PDF) table based on Log-Likelihood minimisation determines the neutrino direction and energy.

Position Reconstruction

A hit selection is necessary to reject background hits. The selection criterion for each pair of hits is:

$$|\vec{r}_i - \vec{r}_j| \geq c_w \cdot |t_i - t_j| \tag{4.3}$$

being:

- $\vec{r}_i$: position of the OM that recorded the hit i.
- t_i: time of the hit i.

- $c_w = 0.217288 \cdot c$ [m $\cdot$ s^{-1}]: speed of light in water for the average Cherenkov light wavelength

This condition selects space-time correlated hits. Starting from this sample of hits, the shower vertex is defined assuming that the following relation is satisfied:

$$(\vec{r}_i - \vec{r}_{shower})^2 = c_w^2 \cdot (t_i - t_{shower})^2 \tag{4.4}$$

where i runs from 1 to the number of selected hits ($N_{SelectedHits}$); $\vec{r}_{shower}$ and t_{shower} are the shower vertex position and time. The system of equations obtained so far is linearised by taking the difference between every pair of equations i and j:

$$(\vec{x}_i - \vec{x}_j)\,\vec{x}_{shower} - c_w^2 \cdot (t_i - t_j)\,t_{shower} = \frac{1}{2}\left[|\vec{r}_i^{\,2}| - |\vec{r}_j^{\,2}| - c_w^2\left(t_i^2 - t_j^2\right)\right] \tag{4.5}$$

The resulting linear equation system can be written as:

$$\mathbf{A}\vec{v} = \vec{b} \tag{4.6}$$

where:

- $\mathbf{A} = \begin{bmatrix} (x_1 - x_2) & (y_1 - y_2) & (z_1 - z_2) & -c_w(t_1 - t_2) \\ \vdots & \vdots & \vdots & \vdots \\ (x_{N-1} - x_N) & (y_{N-1} - y_N) & (z_{N-1} - z_N) & -c_w(t_{N-1} - t_N) \end{bmatrix}$
- $\vec{v}$: is the four-dimensional space-time fit for the vertex.
- $\vec{b} = \frac{1}{2} \cdot \begin{bmatrix} |\vec{r}_1^{\,2}| - |\vec{r}_2^{\,2}| - c_w^2(t_1^2 - t_2^2) \\ \vdots \\ |\vec{r}_{N-1}^{\,2}| - |\vec{r}_N^{\,2}| - c_w^2(t_{N-1}^2 - t_N^2) \end{bmatrix}$

The system is solved using the method of the least linear square fit.
After this step, an *M-estimator* is calculated by minimising the following equation using the previous result as the starting point:

$$M_{Est} = \sum_{i=1}^{N_{SelectedHits}} (q_i \cdot \sqrt{1 + \frac{t_{res,i}^2}{2}}) \tag{4.7}$$

where:

- q_i: charge of *i-th* hit ;
- $t_{res,i} = t_i - t_{shower} - |\vec{r}_i - \vec{r}_{shower}|/c_w$: *time residual* of *i-th* hit.

Direction reconstruction and energy estimator

Starting from the time residuals of the hits with respect to the shower vertex obtained in the previous step, all hits fulfilling the condition are selected:

$$-200 \text{ ns} < t_{res} < 500 \text{ ns} \tag{4.8}$$

The direction and the energy of the neutrino are simultaneously fitted by minimising the negative log-likelihood function:

$$-\mathcal{L} = \sum_{i=1}^{N_{SelectedHits}} log\{P_{q>0}(q_i|E_\nu, d_i, \phi_i, \alpha_i) + P_{bg}(q_i)\} + \sum_{i=1}^{N_{unhitPMTs}} log\{P_{q=0}(E_\nu, d_i, \phi_i)\} \tag{4.9}$$

with:

- $P_{q>0}$: probability for a hit PMT to measure the observed charge.
- q_i: charge of *i-th* hit.
- E_ν: neutrino energy.
- $d_i = |\vec{r}_i - \vec{r}_{shower}|$: distance between the shower vertex and the PMT with the i-th hit.
- $\vec{r}_{shower}$: position of the shower.
- ϕ_i: photon emission angle.
- α_i: photon impact angle on the PMT.
- P_{bg}: probability for a random background hit to have the measured charge.
- $P_{q=0}$: probability for a PMT of not being hit.

This likelihood function depends on the shower vertex reconstruction and the PDFs are built using the MC simulation of shower events in ANTARES. The signal term $P_{q>0}$ is the expectation value of the number of photons on a PMT, given the shower vertex-OM distance, the photon-emission angle and photon-impact angle. The number of emitted photons and therefore the number of photons expected on the PMT is proportional to the neutrino energy. The number of expected photons N is calculated for a 1 TeV shower from the MC and then scaled for different energy according to:

$$N(E_\nu) = N_{1 \text{ TeV}} \cdot \frac{E_\nu}{1 \text{ TeV}} \tag{4.10}$$

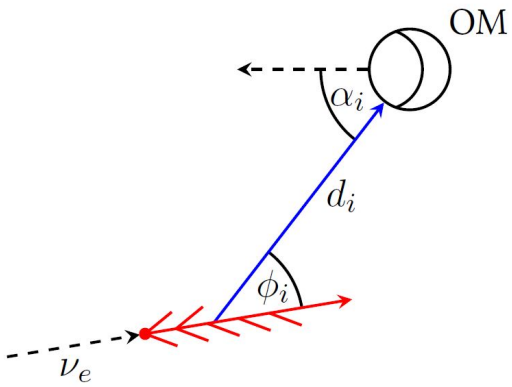

Figure 4.5: Schematic overview of the geometric variables considered in the likelihood method used in the direction reconstruction.

The overall probability to detect n photons, when the expectation is N, is given by the Poisson distribution:

$$P(n|N) = \frac{N^n}{n!}e^{-N} \tag{4.11}$$

The OMs saturate at charges above about 20 p.e. preventing to determine the true number of arriving photons.
The non-hit term $P_{q=0}$ is the probability that a PMT does not detect any hit. It is the Poisson probability to have zero charge when the expectation is N photons on the photocathode:

$$P(N) = P(q = 0|N) = e^{-N} \tag{4.12}$$

Finally the background term P_{bg} is the probability that an uncorrelated optical background event causes a hit with the observed charge. The distribution is taken from the special runs taken with the optical beacons [91], considering all hits with hit times prior to the beacon flash.

Angular error estimator

The angular error is calculated scanning the likelihood landscape around the fit along concentric circles of angular distances increasing in steps of 1 degree. When the likelihood value differs, by more than one from the best fit, the corresponding angular distance is taken as angular error estimate. This is not a rigorous estimate of the total angular error because, if the event has a very asymmetric likelihood landscape, the angular error estimator would only reflect the smallest component along the axes.

Algorithm performance

In plots 4.6 the algorithm performance are shown, for events contained in a cylindrical volume of radius 300 m and high 250 m from the detector center. The shower position can be reconstructed with a precision of about 1 m. The angular resolution ranges between 3 and 10 degrees depending on the energy. The energy resolution is $5\% - 10\%$.

4.2.2 Track-like event reconstruction

In this thesis two track-event reconstruction algorithms are used for the event selection, *AAFit* and *GridFit*. A brief description of the two and the quantities specifically used in this work are reported in the following.

AAFit

The AAFit reconstruction algorithm [92] for track-like events is based on a likelihood fit composed by three consecutive steps of increasing sophistication that provides a starting point for the last likelihood fit. The likelihood function has several local maxima and the fit is successful only if the final minimisation procedure starts with track parameters that are already a good approximation of the optimal solution.

A hit selection analogous to that of the TANTRA algorithm is applied, as well as a similar likelihood approach is used for the final fit. In this case the calculation of the time residuals is based on the hypothesis that photons are emitted by a muon track and the PDF is built accordingly. The following variable is used to characterise the quality of the fit:

$$\Lambda = \frac{log(L)}{N_{DOF}} + 0.1(N_{comp} - 1) \tag{4.13}$$

where:

- $\frac{log(L)}{N_{DOF}}$: log-likelihood per degree of freedom;
- N_{comp}: Number of compatible solutions found with the reconstruction algorithm.

The implementation of the algorithm also provides a covariance matrix for the fitted parameters such as the reconstructed direction angles. From this matrix, error estimates for the two fitted angles ϕ_{tr} and θ_{tr} can be extracted as σ_ϕ and σ_θ. The two error estimates for the separate angles can be combined to produce a total angular error estimator:

$$\beta_{tr} = \sqrt{(\sigma_\phi) \cdot sin(\phi_{tr})^2 + \sigma_\theta^2} \tag{4.14}$$

Hence the β angular resolution and the Λ quality parameter are two strong classifiers to identify a well reconstructed event.

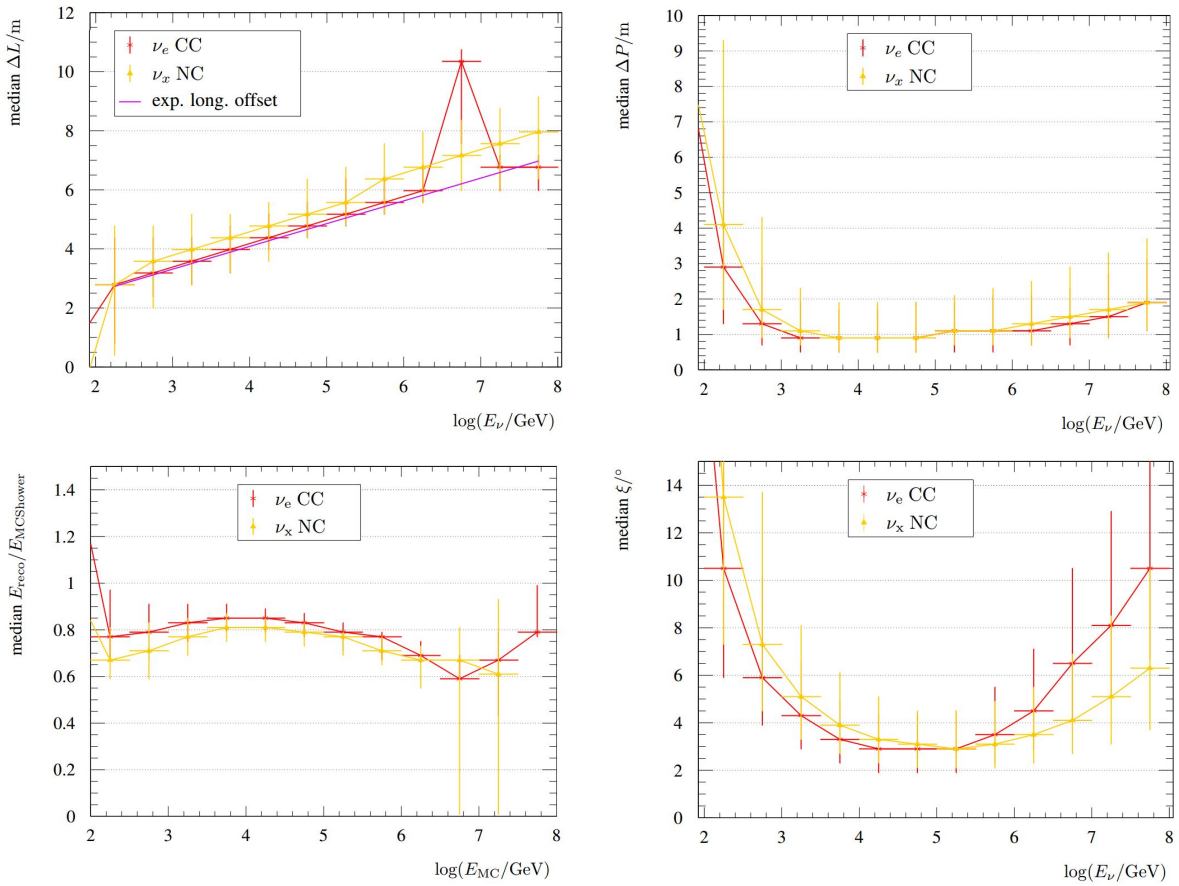

Figure 4.6: **Top-Left**: The distance between the position of the neutrino interaction vertex and the reconstructed shower position along the neutrino axis. **Top-Right**: The distance of the reconstructed shower position perpendicular to the neutrino axis. **Bottom-Left**: The ratio between reconstructed energy and the true Monte Carlo energy as a function of the shower energy. **Bottom-Right**: The angle between the directions of the reconstructed shower and the Monte Carlo neutrino as a function of the neutrino energy.

GridFit

This algorithm [93] starts by binning the full solid angle into 500 different directions. The number of hits compatible with a muon track coming from each direction is evaluated and a likelihood fit is performed to obtain the most relaiable moun direction. The *GridFit Ratio* quality parameter is then computed as the sum of the compatible hits of all upward-going and all downward-going test directions:

$$R_{GF} = \frac{\sum_{up-going} N_{hits}}{\sum_{down-going} N_{hits}} \tag{4.15}$$

The lower this number, the higher the probability for this event to be a downward-going muon.

4.3 Boosted Decision Tree (BDT)

In this section the general implementation of a *Boosted Decision Tree* classifier is described. The specific application of this multivariate analysis technique, used in this thesis, is explained in detail in chapter 5. A BDT is an algorithm that belongs to the family of the *supervised machine learning* techniques where the goal is the identification of a function that allows to classify an event sample into multiple categories labeled like *signal* or *background*. The use of the term *supervised* comes from the need of a *training* sample of events, whose output (label) is known, to build the classification function.

4.3.1 Decision tree

A *decision tree* is a binary tree classifier whose structure is sketched in figure 4.7. In the scheme, for each input event, a sequence of binary conditions (nodes) on one single variable are applied until a stop criterion is fulfilled. The result is the splitting of the phase space into several regions belonging to the *signal* or *background* domain.

The training of a decision tree is the process that defines the splitting criteria for each node. The first node is called *root node* and the training starts with the application of a starting condition to the full training sample. The root node splits the sample into two sub-samples. An additional condition is applied at the next node, which produces a further splitting. This procedure is iterated until the whole tree is built. At each node the discrimination variable and the corresponding cut value are chosen in order to obtain the best separation between signal and background. The splitting procedure ends when the minimum number of events, which is speficified by the user in the algorithm configuration, is reached. The last level of nodes represent the so-called *leaves.* They are classified as signal or background depending on the majority of events that reach the leaf.

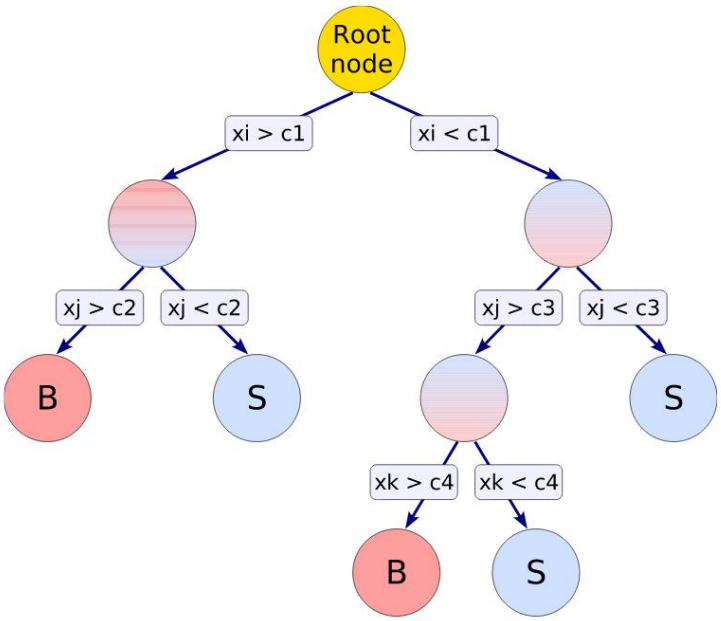

Figure 4.7: Schematic view of a decision tree where a sequence of binary decisions based on the variables x_i are applied to the data. Each decision is taken on the variable that better performs the discrimination between signal and background at that specific selection stage. Some variables can be used several times in different nodes or might not be used at all. At the end of the tree each termination point, called *leaf*, is labeled S (signal) or B (background) depending on the number of training events, with the same label (S or B), that end up there. Figure taken from [78].

4.3.2 Boosting

The *decision tree* technique can be improved by using a *boosting* algorithm where the classification machine is built with several trees forming a forest. All trees are built starting from the same training sample applying properly evaluated weights, depending on the boosting technique. At the end the results are combined into a single classifier which computes an average of the individual decision from each tree. The advantage of the boosting technique, introduced for the first time in the early '90s [94], is a reduction of the fluctuations in the training sample, resulting in a more stable response of the classifier and in a better classification performances with respect to a single tree.

Adaptive Boost (AdaBoost)

To train the BDT used for the event selection in this thesis the so-called AdaBoost (adaptive boost) [95] has been used.

During the training many trees are built sequentially and the events that are wrongly classified are then reweighted for the following tree according to a parameter α defined as:

$$\alpha = \frac{1 - err}{err} \tag{4.16}$$

where *err* is the misclassification rate from the previous tree. The weights of the entire sample are renormalised in order to keep the sum of weights constant. The result of the individual classifier (tree) is defined as $h(\mathbf{x})$, where $\mathbf{x}$ are the variables used for the classification, and takes the value:

- $h(\mathbf{x}) = +1$ for signal
- $h(\mathbf{x})$ = -1 for background

Finally the *boosted* event classification is defined according to this equation:

$$y_{Boost}(\mathbf{x}) = \frac{1}{N_{collection}} \cdot \sum_{i}^{N_{collection}} ln(\alpha_i) \cdot h_i(\mathbf{x}) \tag{4.17}$$

where the $N_{collection}$ is the total number of trees. Each event is classified as signal-like/background-like depending on the higher/lower value of y_{Boost}.

5 Event selection

The goal of this study is the measurement of the atmospheric electron neutrino flux in the energy range between a few GeV and a few dozens of TeV. This energy interval is accessible to a neutrino telescope like ANTARES which benefits of 10 years of data taking. In a neutrino telescope the interactions of electronic neutrinos determine the topology of events called *shower-events* (see 2.4.2). In the previous ANTARES analyses [6, 96] that used *shower-like* events, the selection was based on the combination of different observables provided only by the *shower-like* reconstruction algorithms. The event selection developed in this work contains several innovations and improvements including the use of a hybrid approach to look for *shower-like* events and a machine learning technique called Boosted Decision Tree. The innovative hybrid approach, on which the development of this *shower-like* selection of events is based, is the search for events with good reconstruction quality parameters according to the *shower-like* reconstruction algorithms and simultaneously poorly reconstructed as *track-like*.

5.1 Signal and background definition

The background in this analysis is composed almost entirely of atmospheric muons: one neutrino over ten thousands atmospheric muons is present in the event sample. To overcome the obstacle of the very small signal-to-noise ratio, it is necessary to develop a specific event selection chain to obtain a final sample when the background is almost entirely rejected, while keeping a statistically significant sample of neutrinos. The event selection was optimized in simulated events. The signal components are atmospheric electron and muon neutrinos generated with the Monte Carlo simulation technique (see. 4.1) according to the atmospheric neutrino models from [34] and [35].

5.2 Event selection strategy

The event selection is organized in 3 phases, during which the signal-to-noise ratio is gradually improved. In the following, a brief description of the event selection phases is presented:

- **Starting conditions**: definition of simple criteria able to reject a large part of the background due to bio-luminescence (described in chapter 3);
- **Preselection**: search for an efficient parameter to reject most of the atmospheric muons. The cutting value is tuned to preserve a good signal-to-noise ratio and to have adequate statistics to train the Boosted Decision Tree (BDT) used in the final selection phase;
- **Final selection**: training of a BDT to improve the rejection of the background due to atmospheric muons and to increase the purity of the sample of neutrinos;

Figure 5.1 shows the effect of each selection criteria on the signal of atmospheric neutrinos and on the background. The three phases previously described, in which the selection of events is divided, are also highlighted.

5.3 Blinding policy

All ANTARES analyses follow a blinding policy to avoid possible biases. The cuts and the selection criteria are studied and optimised on a sample of Monte Carlo simulated events and only at the end they are applied to the data. A small sample of data, about 10% of the total, named in the following as *0-runs* sample, is used for data-Monte Carlo comparison along the event selection chain and for sanity checks. Each time the whole data sample is used, the wording *data: 2007-2017* is reported.

5.4 The ANTARES data sample (2007-2017)

The ANTARES neutrino telescope has been taking data since 2007. The data sample for this analysis includes the 5-line period of ANTARES, when ANTARES collected data in an uncomplete configuration, and covers the whole data acquisition of the telescope until the end of 2017, for a total livetime of 3012 days. The mean run duration is around 3 hours between 2007 and 2013 and for a couple of months between 2016 and 2017. During the remaining data acquisition period the run duration has been increased to 12 hours in order to reduce the dead-time due to the transition between two consecutive runs.

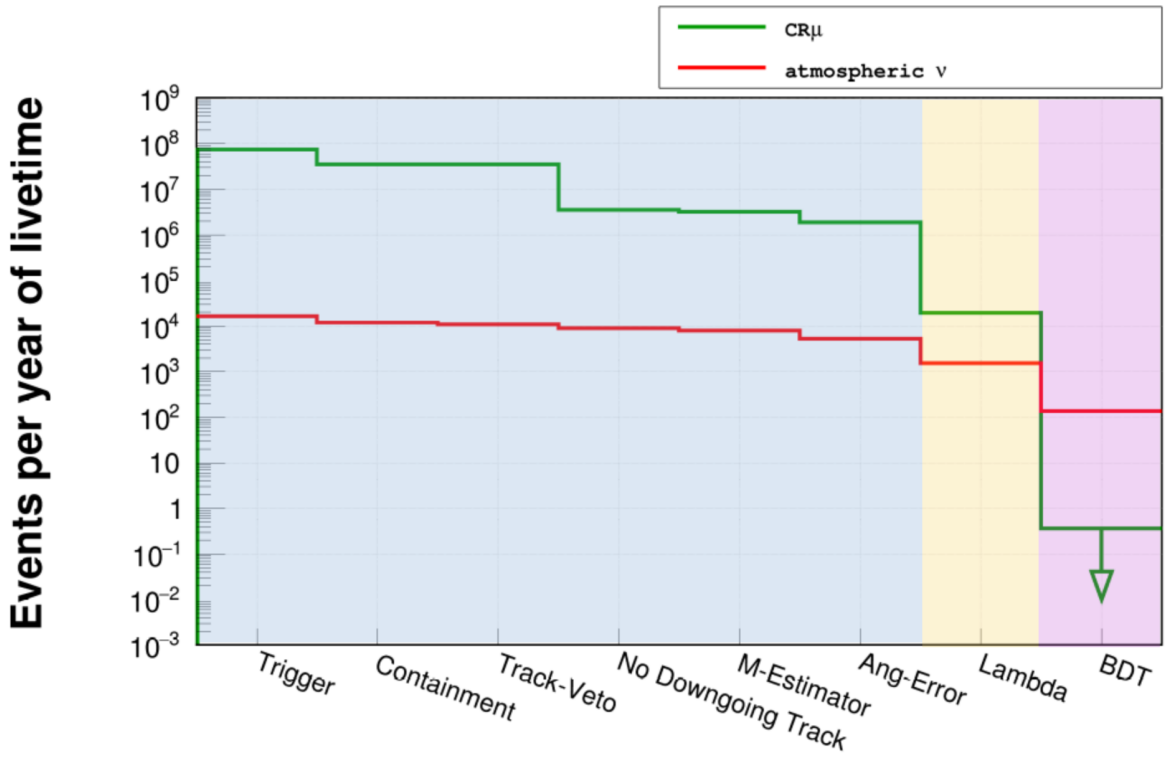

Figure 5.1: Effect of the selection criteria on the signal and on the background. The selection criteria applied are shown following the order of application on the x-axis and the number of events selected at each step is represented, normalized to one year of effective livetime, in the y-axis. The three colored bands blue, yellow and purple represent respectively the *starting conditions*, the *preselection* and the *final selection* phases. The last background point has an arrow because it represents an upper limit on the number of background events in the final sample.

5.5 Starting conditions

In the *starting conditions* step, several criteria are used to impose minimum conditions of acceptability of the events, before and after reconstruction. These parameters have been identified and inherited from previous analyses in which *shower-like* events were considered [89, 96, 97].

5.5.1 Sparking runs

The high voltage inside the PMTs occasionally creates a spark-over that becomes visible as a bright flash inside the OM. The device that should actually detect photons from *shower-like* events, which are regarded as point-like light source, suddenly turns itself into a point-like light source. This phenomenon has to be taken into account in *shower-like* analyses because sparking events mimic a high energy *shower-like* event. A small number of ANTARES runs (less than 1% of the total number of runs), called *sparking-runs*, have been identified in past analyses by searching for very frequent events located close to an OM, and are totally excluded from the present analysis.

5.5.2 Selection criteria

Hereafter the criteria belonging to the selection phase called *starting conditions* are described, following the order of application:

- **Trigger**: The data acquisition system of the ANTARES detector is described in chapter 3. The main physics triggers are the 3D-directional scan logic trigger $3N$ and cluster logic trigger $T3$. In this analysis only $T3$ or $3N$ triggered events are selected

- **Containment**: Only events, reconstructed with the TANTRA *shower-like* reconstruction algorithm Sec.4.2.1, whose vertex is contained in a cylindrical volume of radius ρ and height z, centered around the detector, are selected:

$$(\rho_{shower} < 300\ m) \quad and \quad (|z_{shower}| < 250\ m) \tag{5.1}$$

- **Track-Veto**: In previous ANTARES analyses, events have already been identified that are believed to belong to the category of *track-like* topology events [96, 97, 49]. Since this topology of events is not part of the original signal for this analysis it was decided to remove them in the event selection. These events are characterized by observables provided by the AAFit *track-like* reconstruction algorithm therefore the rejection of track like events is obtained denying the logical combination of

the criteria used for the selection of these events, by imposing the following logic condition:

$$NOT: \ (\Lambda_{AAFit}) > -5.2 \quad and \quad (\beta_{AAFit} < 1.0) \quad and \quad (cos(\theta_{Zenith,AAFit}) < 0.1) \tag{5.2}$$

- **NoDowngoingTrack**: the background of atmospheric muons is seen by the detector mainly as *track-like* events directed downwards, a condition is imposed such that all events must be reconstructed by the *track-like* reconstruction algorithm called AAFit as directed upwards:

$$cos(\theta_{Zenith,AAFit}) < 0.0 \tag{5.3}$$

- **M-Estimator**: As described in chapter 4, this parameter represents the estimator of goodness of fit given by the TANTRA *shower-like* reconstruction algorithm Sec. 4.2.1. The lower this value, the lower the probability of confusing a *track-like* event with a *shower-like* event:

$$M_{estimator} < 1000 \tag{5.4}$$

- **Ang-Error**: TANTRA *shower-like* reconstruction algorithm associates an angular uncertainty called β to the estimated incoming direction of each event. A maximum estimated angular uncertainty of 30 degrees is accepted:

$$\beta_{shower} < 30 \tag{5.5}$$

5.6 Pre-selection criteria for *shower-like* events

After the *starting conditions* in the sample about one neutrino event every 350 atmospheric muon events is present. From this quantitative consideration it is evident that the data are still dominated by the background. Therefore it is necessary to identify a parameter with a strong rejection power of the background and at the same time, able to preserve the signal events as much as possible. The experience of the analyses and studies published by the ANTARES collaboration guided the choice of the selection parameter in favor of the use of the variable Λ, which expresses the quality of the *track-like* reconstruction algorithm AAFit. This parameter allows to distinguish efficiently between the events generated by atmospheric muons and the events generated by neutrinos. The distribution of the Λ parameter for events that passed the *starting conditions* criteria is shown in the figure 5.2.

The events due to atmospheric muons are concentrated in the low value region of the Λ parameter while the neutrino signal is relatively dominant in the right region of the plot. Furthermore, at Λ about -5.2 there is a drastic drop of the number of events of

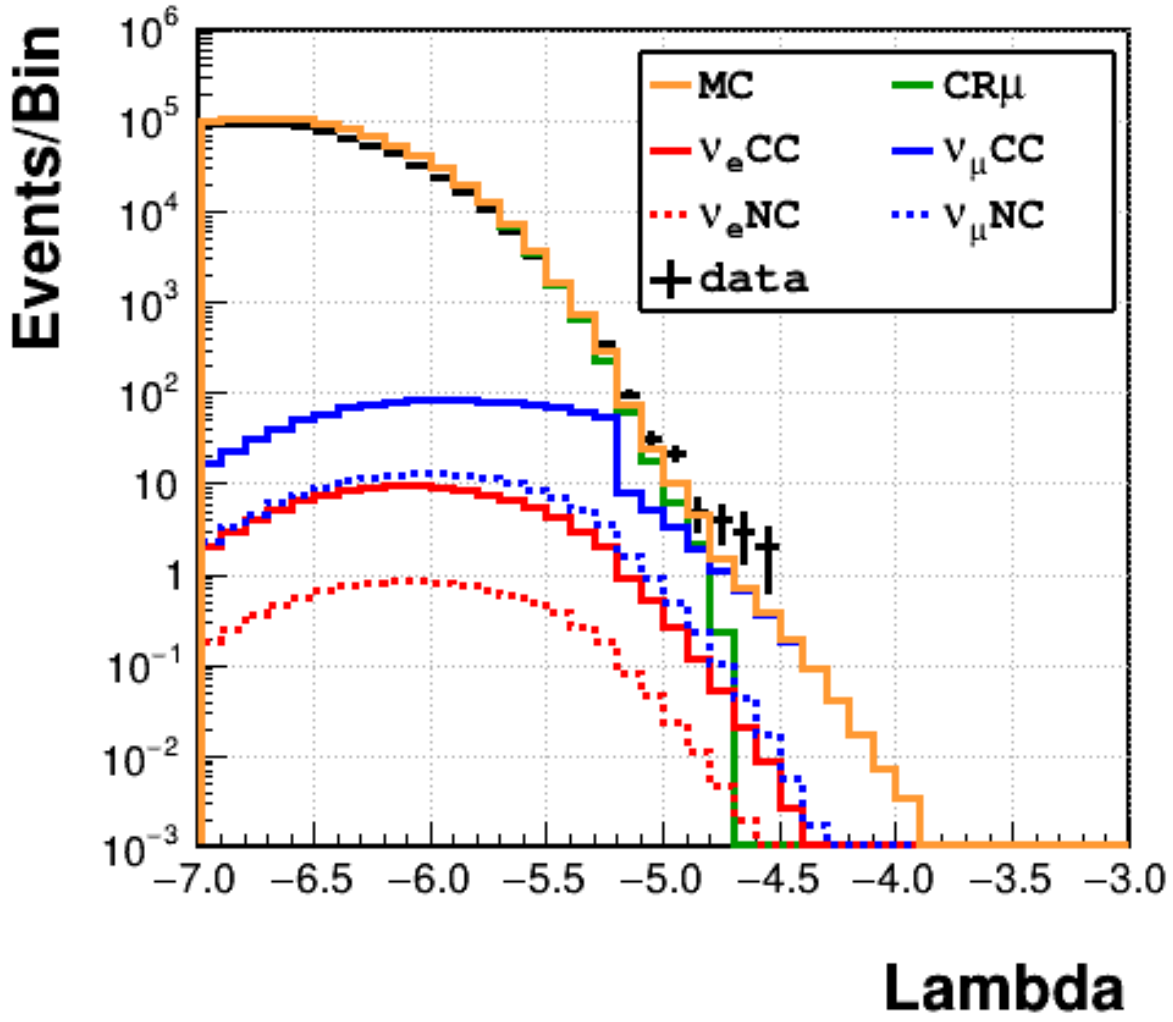

Figure 5.2: Λ parameter distribution for the events after the *starting conditions* phase. The black crosses are real data, the orange line is the sum of all Monte Carlo contributions. The green line represents the atmospheric muon events. The blue lines refer to atmospheric muon neutrino events and the red ones to atmospheric electron neutrinos. Solid lines are used for charge current interactions and dashed lines for the neutral current interactions.

the muon neutrinos that interact by charge current. This effect is due to the starting conditions criterion called *track-veto*. This interaction channel identifies the so-called *track* events that have already been cataloged in other analyses and are not of interest in this study. Hence they are excluded a priori.

Once the parameter to be used to discriminate signal and background has been identified, it is necessary to estimate the cut value for the event selection. In order to decide the best value for the cut based on the Λ parameter, the statistical significance of the signal (all neutrino events) over the total number of events of the sample has been defined as:

$$Significance = \frac{N_{signal}}{\sqrt{N_{signal} + N_{background}}} \tag{5.6}$$

The anti-cumulative distributions of the parameter Λ for atmospheric muons (background), and for signal is made of the sum of electronic and muon neutrinos (signal) and is represented in figure 5.3.

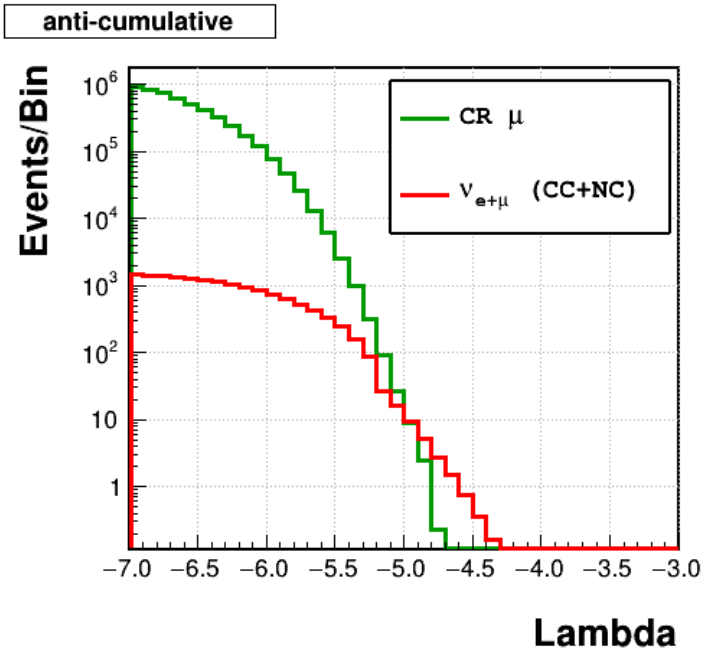

Figure 5.3: Anti-cumulative distribution of Λ for atmospheric muon background events, green line, and atmospheric neutrino events, red line.

In figure 5.4 the value of the statistical significance previously described is represented as a function of the parameter Λ. This estimator has a maximum at:

$$\Lambda = -5.36 \tag{5.7}$$

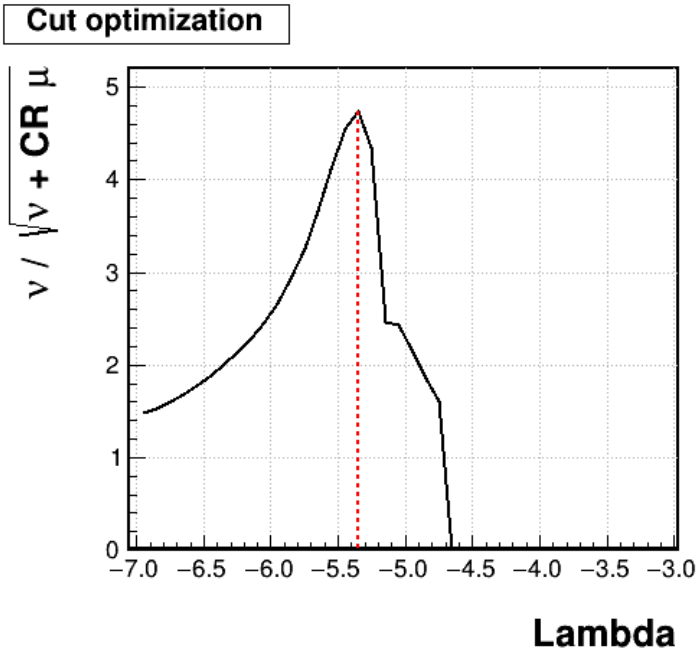

Figure 5.4: Statistical significance of the neutrino signal sample over the atmospheric muon background as a function of the Λ parameter.

The value of the statistical significance just calculated would be the best cut value on Λ if the event selection chain ended here. Unfortunately, the final sample resulting from this cut is not pure enough for the last part of the analysis, the unfolding procedure to obatain the spectrum of the atmospheric electronic neutrino flux. It was therefore decided to optimize the cut on the Λ parameter to pre-select the events which will then be definitively skimmed by a further parameter, built specifically for this analysis and described in the next section.

5.7 Final selection

The difficulty met in previous ANTARES analyses [6, 96] (*shower-like* event selection by rejecting the background of atmospheric muons with traditional strategies), suggested the use of a machine learning technique called *Boosted Decision Tree* (BDT), described in Sec. 4.3.1. This approach allows the classification of events as belonging to the signal or to the background. The main advantage of this tool is the very efficient search in the multidimensional space made up of several parameters, looking for the region where the signal-to-noise ratio is higher.

5.7.1 The training variables

The variables used to build the BDT are listed below. Each variable is shortly explained, if it has not been used and described before.

The prefix *Tantra* or *AAFit* to the name of the variable indicates that it has been calculated with one of the two reconstruction algorithms:

- ***Tantra* Zenith**: reconstructed Zenith angle;
- ***Tantra* Azimuth**: reconstructed Azimuth angle;
- ***Tantra* X, Y, Z**: reconstructed X, Y and Z position of the interaction vertex;
- ***Tantra* M-estimator**;
- ***Tantra* Lines**: Number of lines used in the final fit with at least one hit;
- ***Tantra* Hits**: Number of hits used to reconstruct the event in the last fit;
- ***Tantra* AngularEstimator**: angule error as described in 4.2.1;
- ***AAFit* Zenith**: reconstructed Zenith angle;
- ***AAFit* Azimuth**: reconstructed Azimuth angle;
- ***AAFit* TrackLength**: Estimated track length inside the detector volume;
- ***AAFit*** Λ;
- ***AAFit* Beta**: Angular resolution associated to a *track-like* event;
- ***GridFit* Quality**: Quality parameter of the *track-like* reconstruction algorithm GridFit Sec. 4.2.2;
- **μ-veto**: To discriminate between showers and atmospheric muons, a dedicated likelihood ratio variable has been defined. Track and shower likelihoods, considering only hits in coincidence on the same storey within 20 ns, are built from PDFs based on the following parameters:
  - distance r_i of the hit i from the reconstructed shower position r_{shower};
  - time residual t_{res} of the hit i defined as:

$$t_{res,i} = t_i - t_{shower} - |\vec{r}_i - \vec{r}_{shower}|/c_w \tag{5.8}$$

  - Q: number of photo-electrons detected for each event's hit;

The likelihood is:

$$\mathcal{L}_{\mu-veto} = \sum [log(P_{shower}/P_{muon})] \tag{5.9}$$

with $P_{shower} = (r, t_{res}, Q|P_{shower})$ and $P_{muon} = P(r, t_{res}, Q|muon)$ are the PDFs built for the signal and background events;

- **N-On-Time**: Number N of hits in a time window around t_{res} defined as:

$$-20 < t_{res}/ns < 60 \tag{5.10}$$

Figures 5.5, 5.6 and 5.7 show the quantities used in the training of the BDT. In each plot is represented only the distribution of the CC electron neutrino events identified as signal, and atmospheric mouns events identified as background. Both distributions were then renormalized for easier comparison.

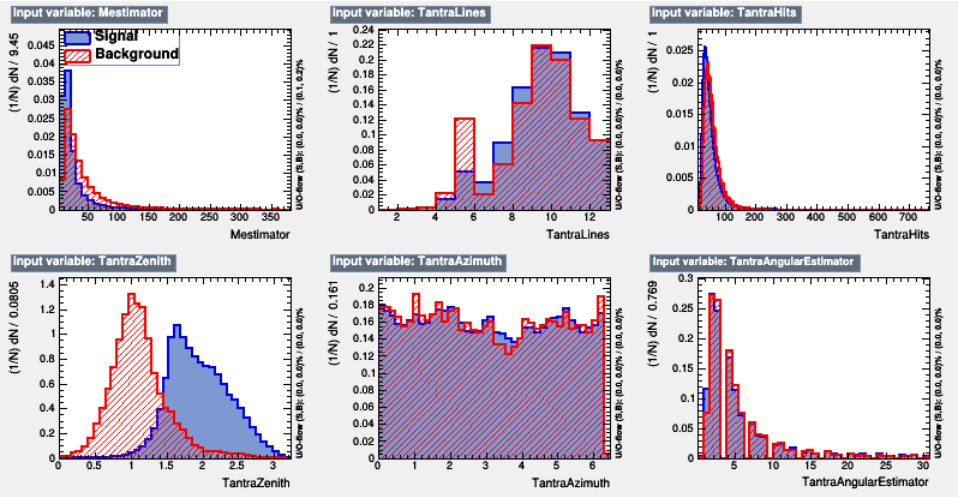

Figure 5.5: Distributions of training variables: *Tantra* M-estimator, *Tantra* Lines, *Tantra* Hits, *AAFit* Zenith, *Tantra* Azimuth, *Tantra* AngularEstimator. For each variable, the distributions of the signal in red, CC electron neutrino events, and the background in blue, atmospheric muon events, are represented and renormalized for easier comparison.

5.7.2 The training event sample

The training of the BDT has been performed considering the atmospheric muons as background. The signal is represented by the CC interactions of electronic neutrinos only. They are the cleanest case of a *shower-like* event, given that they develop an electromagnetic shower in the neutrino interaction.

A ranking of the BDT input variables is derived by counting how often the variables are used to split decision tree nodes, and by weighting each split occurrence with the

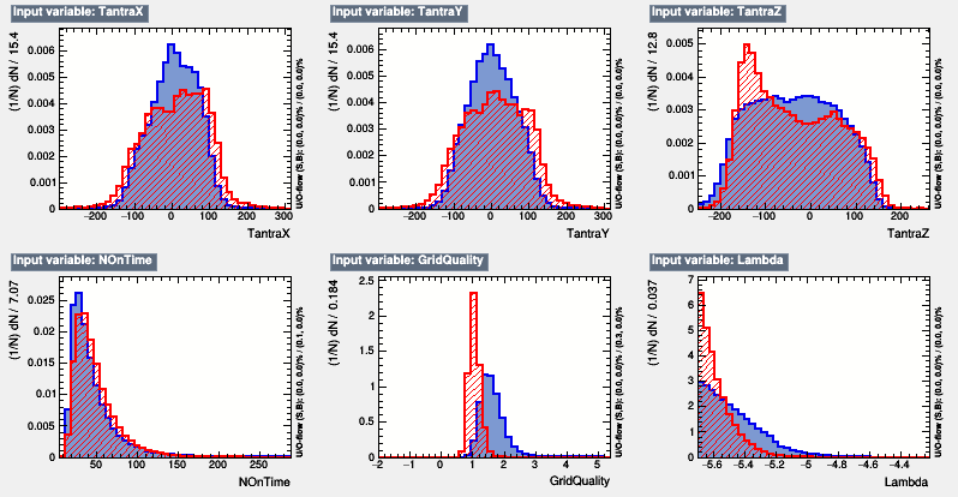

Figure 5.6: Distributions of training variables: *Tantra* X, *Tantra* Y, *Tantra* Z, N-On-Time, *GridFit* Quality, *GridFit* Quality. For each variable, the distributions of the signal in red, CC electron neutrino events, and the background in blue, atmospheric muon events, are represented and renormalized for easier comparison.

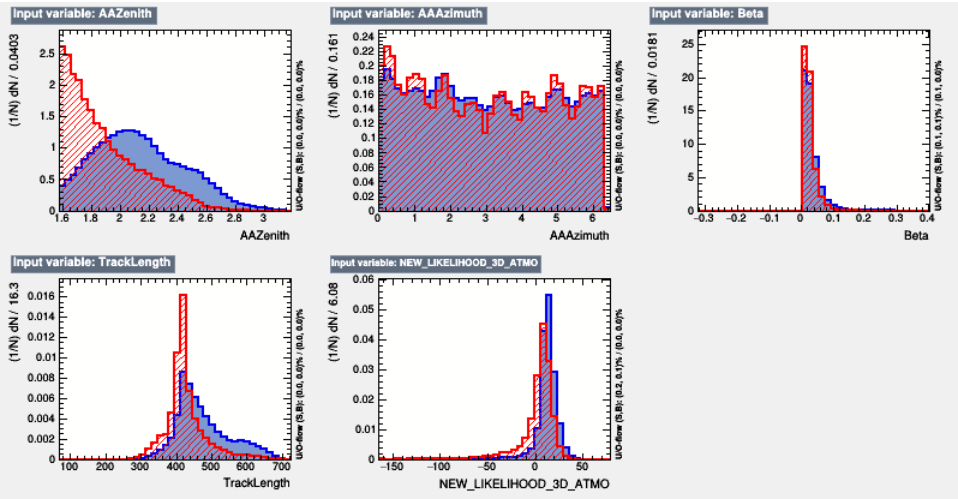

Figure 5.7: Distributions of training variables: *AAFit* Zenith, *AAFit* Azimuth, *AAFit* Beta, *AAFit* TrackLength, μ-veto. For each variable, the distributions of the signal in red, CC electron neutrino events, and the background in blue, atmospheric muon events, are represented and renormalized for easier comparison.

separation gain it has achieved and by the number of events in the node [98]. In table 5.1 the variables used in the BDT training are listed according to their ranking.

The Λ variable, already used for the *preselection* phase, is present in the training

Rank	Variable	Variable ranking
1	*Tantra* Zenith	$1.202 \cdot 10^{-1}$
2	*GridFit* Quality	$1.067 \cdot 10^{-1}$
3	N-On-Time	$7.124 \cdot 10^{-2}$
4	μ-veto	$5.930 \cdot 10^{-2}$
5	*Tantra* Azimuth	$5.893 \cdot 10^{-2}$
6	*AAFit* Zenith	$5.757 \cdot 10^{-2}$
7	*Tantra* Z	$5.625 \cdot 10^{-2}$
8	*Tantra* X	$5.530 \cdot 10^{-2}$
9	*AAFit* Azimuth	$5.514 \cdot 10^{-2}$
10	*Tantra* Y	$5.357 \cdot 10^{-2}$
11	*Tantra* M-estimator	$5.107 \cdot 10^{-2}$
12	*AAFit* TrackLength	$5.104 \cdot 10^{-2}$
13	*Tantra* Hits	$5.047 \cdot 10^{-2}$
14	*GridFit* Quality	$4.832 \cdot 10^{-2}$
15	*Tantra* Lines	$4.093 \cdot 10^{-2}$
16	*Tantra* AngularEstimator	$4.015 \cdot 10^{-2}$
17	*AAFit* Beta	$2.389 \cdot 10^{-2}$

Table 5.1: Observables used to train and build the BDT. The order, from top to bottom, is given by the variable ranking defined in chapter 4.

variables list. The reason is that the *preselection* and *final selection* phases are closely linked. In fact, depending on the more or less strict cut applied on Λ in the *preselection* phase, a different sample of events is obtained and used for the BDT training. The sample of events used for training is characterized by the absolute number of events but also by the mixture of signal and background events. In fact, together with the choice of the variables that describe the events, the features of the data sample used for training strongly influence the performance of the BDT in the signal-background discrimination.

A critical aspect in the definition of the training sample is the right balance between the request of a large number of events and the need to train the BDT with the right kind of events. Actually the BDT must recognize and reject background events that cannot be identified with other methods.

To fix the Λ value for the *preselection*, and therefore to select the events used for the BDT training, an iterative procedure has been applied starting from the optimal value of Λ considered in the *preselection*, namely $\Lambda = -5.36$.

Starting from this value and progressively relaxing the cut on Lambda, i.e. accepting a larger contamination of background events, several samples were created and used to train the BDT. The agreement between data(0-runs)-Monte Carlo for each sample resulting from the different "trees" has been evaluated. The BDT producing an average agreement close to one (see table 6.1) has been selected and the corresponding lambda value accepted as the optimal cut. In this analysis the choice is:

$$\Lambda > -5.7 \tag{5.11}$$

In figure 5.8 the distribution of the best BDT prepared according to the procedure described above, is shown.

The BDT is an excellent discriminator between signal and background. The region with low BDT values (left of the plot) is dominated by atmospheric muons while the high value region of the BDT is dominated by neutrino events.

The green line in the plot represents an estimate of the contribution of the background in the region of high BDT values. This extrapolation is made with a simple Gaussian fit and sets an upper limit to the number of atmospheric muons still present in the data sample when all atmospheric muons in the Monte Carlo simulations are rejected.

5.7.3 BDT details

Machine learning techniques are often considered as black boxes in which the functioning of the algorithm cannot be inspected. The control and monitoring of the effect of each parameter can be hardly interpreted if the technique uses a large number of parameters, 17 in this case. In order to clarify how the BDT can discriminate between signal and background, the BDT correlation as a function of each of the 17 training variables plus the reconstructed energy estimation provided by Tantra, is shown in figures 5.9 and 5.10.

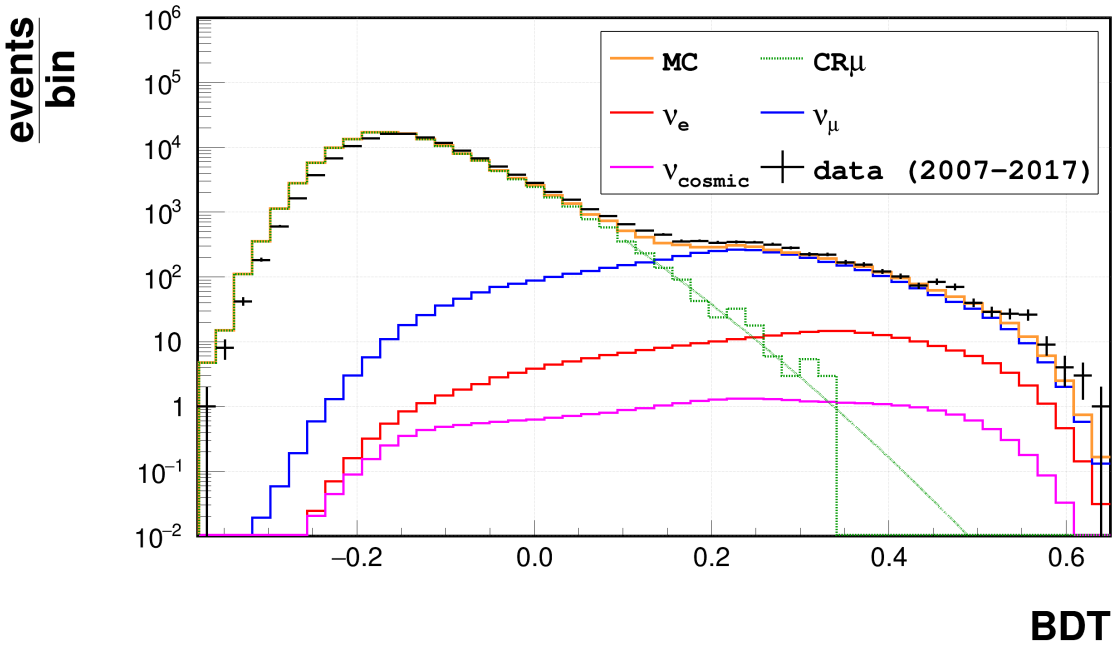

Figure 5.8: BDT parameter distribution for the events after the *preselection* phase. The black crosses are the real data while the orange line is the sum of all the Monte Carlo contributions. The green line represents atmospheric muon events and the green dashed line is the Gaussian fit extrapolation of the atmospheric muon distribution for BDT values higher than 0.33. The blue line refers to atmospheric muon neutrinos and the red one to the atmospheric electron neutrinos. Finally the magenta line is the cosmic neutrino flux estimated with the ANTARES data in a previous analysis [97].

These figures aim at making clearer how the BDT can identify whether an event is a signal or a background event.

5.7.4 BDT cut value

The purpose of this analysis is to measure an energy spectrum and to do this an unfolding procedure, described in the next chapter, is required. The aim of the unfolding is to put one or more points on a graph that correspond to the measurement of the atmospheric neutrino flux. This achievement is substantially different from the point of view of the cuts optimization compared to searching for an unknown signal. In this case one can apply procedures for maximizing statistical observables such a significance or minimizing an upper limit in order to reject a model in the most stringent way. In the case of this analysis it is not easy to find a single parameter that can be maximized or minimized in order to obtain the best value to select the events using the BDT. The measurement of atmospheric electron neutrinos has never been done by the ANTARES Collaboration because of the lack of statistics due to the limited data sample and, more relevant, because *shower-like* event selection strategies were not efficient enough to completely reject the atmospheric muon background. This second point led to the idea of proposing as cut the first BDT value that completely rejects the atmospheric muon background present in the ANTARES simulations, that is:

$$BDT > 0.33 \tag{5.12}$$

This *minimal* optimization approach allows to face the next phase of unfolding under the hypothesis of a minimum atmospheric muon background and have the maximum number of signal events at the same time. This strategy of optimizing the parameter for the *final selection* leaves room for future optimization but, as shown in the next chapter, this simplistic choice for the cut optimization already allows to fulfill the purpose of the analysis.

5.8 The selected sample

After the *final selection* all the events with a BDT value greater than 0.33 are selected. The table 6.1 shows the number of events, for data and Monte Carlo, after the cut in Λ (*preselection*) and after the cut on the BDT (*final selection*). The signal/background ratio has significantly improved from one phase to another. It is also important to underline that in the final sample there are about a thousand neutrino events of which, at most 3, may be due to atmospheric muons. Concerning the numbers of the various neutrino flavours, it is clear that the sample is dominated by atmospheric muon neutrinos while only about 10% of the events are due to electron neutrinos. This result is acceptable

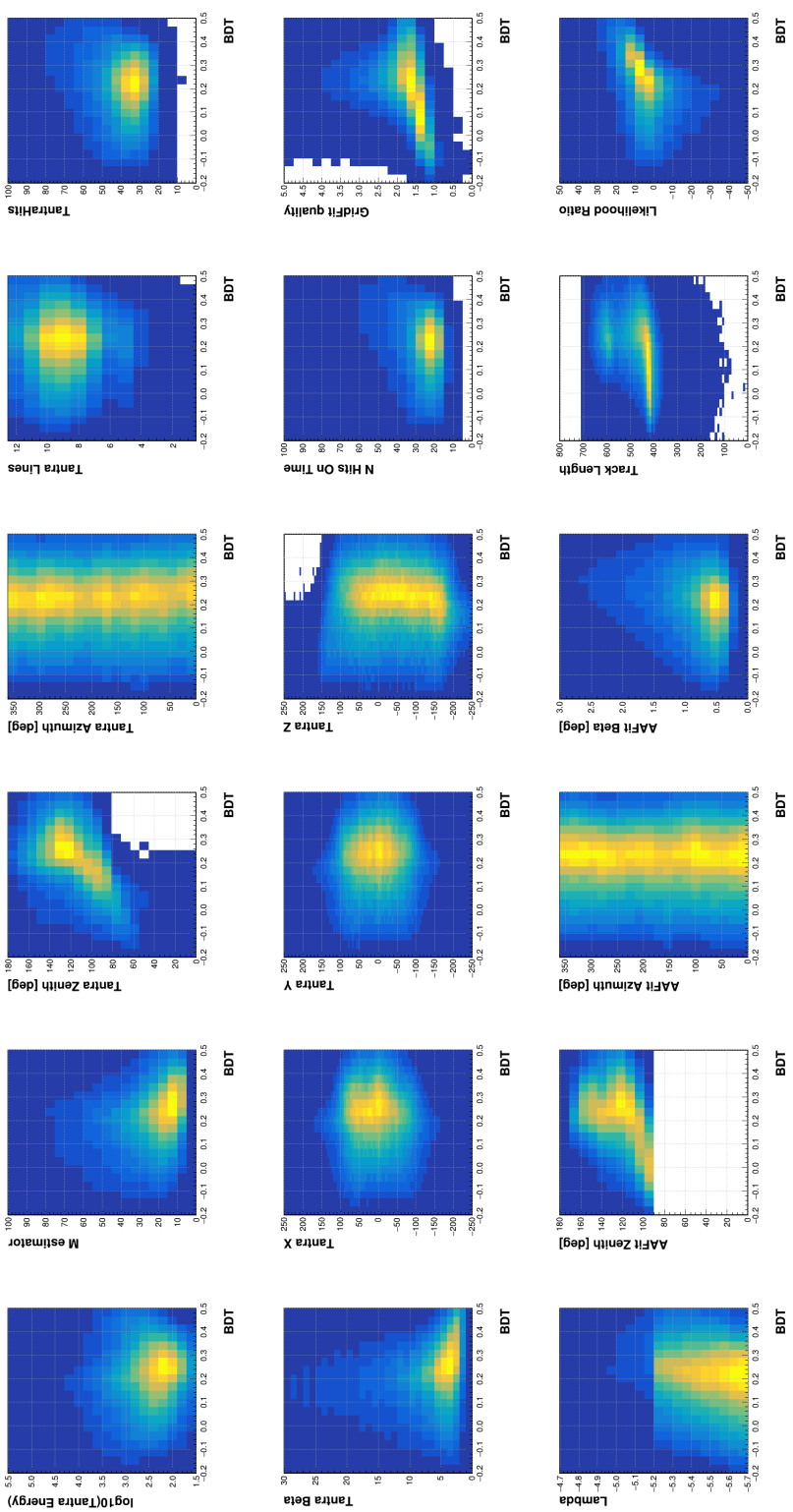

Figure 5.9: Distributions of the 17 variables used for the BDT training, plus the Tantra reconstructed energy estimator, as a function of the BDT parameter for the events coming from atmospheric electron and muon neutrinos.

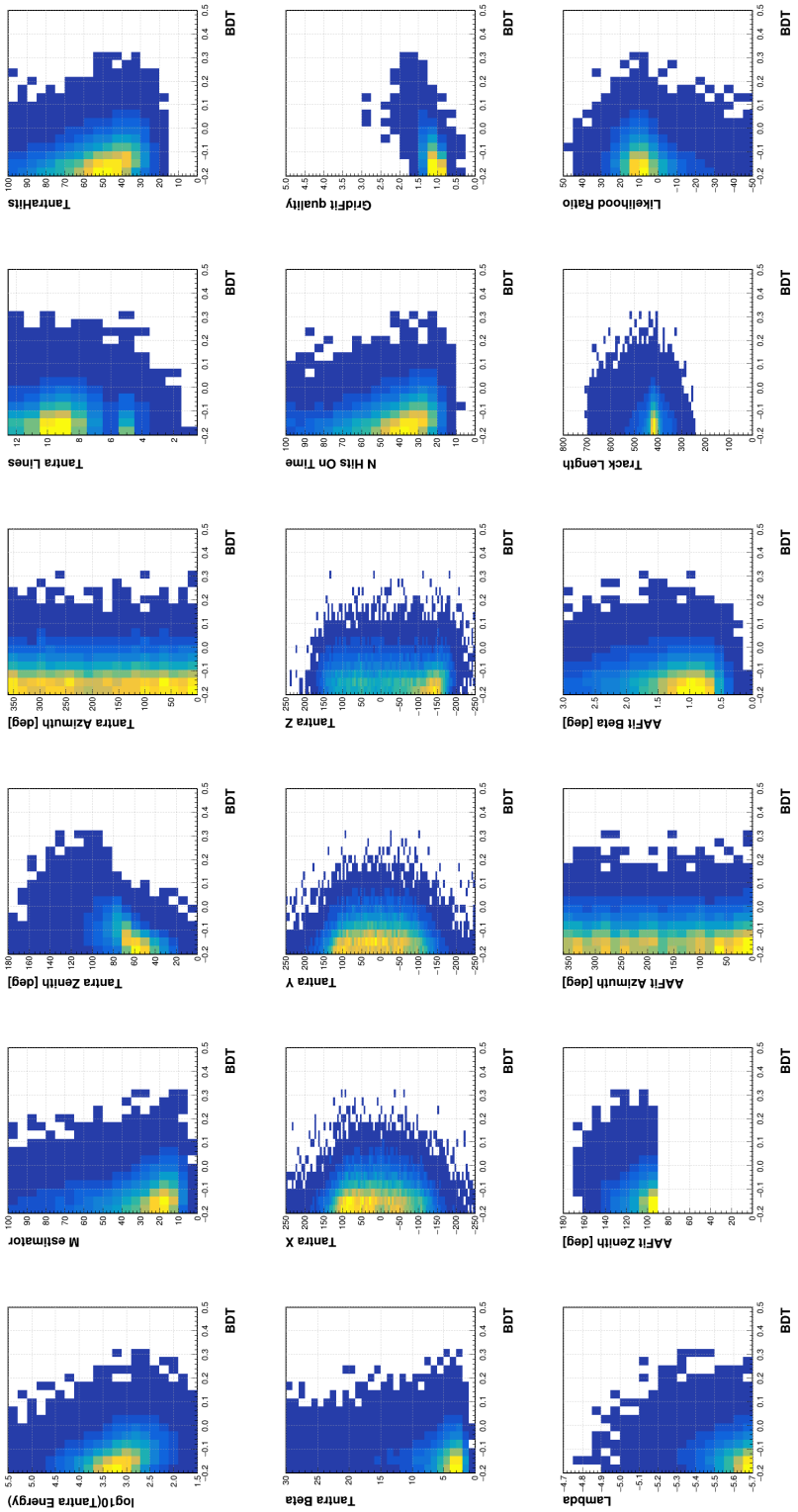

Figure 5.10: Distributions of the 17 variables used for the BDT training, plus the Tantra reconstructed energy estimator, as a function of the BDT parameter for the background events coming from atmospheric muons.

	Preselection ([1])	**Final selection ([2])**
Data	133676	1016
MC sum	141200	914
CR μ	136700	$< \sim 3$
Atmospheric ν_e CC	242	95.6
Atmospheric ν_e NC	21.6	8.6
Atmospheric ν_μ CC	3780	620
Atmospheric ν_μ NC	401	180
Cosmic ν ([3])	30.4	9.2

Table 5.2: ([1])Preselection after Λ cut, ([2])Final selection after BDT cut, ([3])Cosmic flux from ANTARES diffuse flux fit as presented in [97]:
$\phi = (4.8 \cdot 10^{-7})\ E^{-2.3}\ [\ GeV^{-1} \cdot cm^{-2} \cdot s^{-1} \cdot sr^{-1}]$

given that, for example at $\sim$1 TeV, the expected ratio between the atmospheric flux of muonic neutrinos and electronic neutrinos is expected to be ~ 20.

One aspect has to be clarified: why is the final sample mainly composed of muon neutrino events that interact by charged current? This interaction channel should generate the *track-like* event topology in which the muon generated in the interaction produces a through going track. This fact seems in conflict with the purpose of the selection strategy or the search for *shower-like* events. In fact, if a muon neutrino interacts by charged current inside the detector or very close to it, the track of the muon escaping from the interaction vertex can hardly be distinguished from the sphere of light produced at the point where the neutrino has interacted.

To support this explanation the figure 5.11 shows the interaction vertices of the simulated events produced by the charged current interaction of muon neutrinos, which have passed the whole chain of cuts. It can be clearly seen that the neutrinos have all interacted within or very close to the detector, therefore they can be classified in the topology of events called *starting-tracks*.

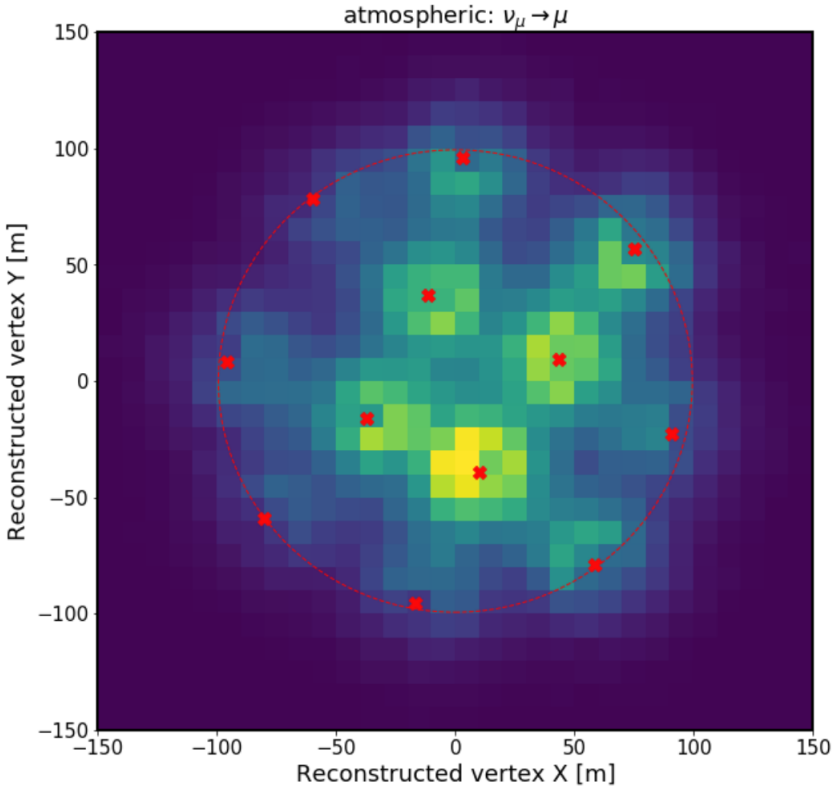

Figure 5.11: Reconstructed interaction vertices of charge current interacting muon neutrinos, after the *final selection* criteria. The x and y axes represent the horizontal plane of the detector position. The red crosses are the positions of the detector strings and the red dashed circle shows the fully contained volume.

6 Unfolding procedure

In high energy physics, measurements are often done as counting experiments, where events are grouped into certain regions of phase-space, also called bins. However, the kinematic properties of each event, such as four-momenta of particles and derived quantities, are measured only at finite precision due to inevitable detector effects. As a consequence, events may be found in the wrong bin. Furthermore there is the presence of background, such that only a fraction of the events observed in a given bin originates from the searched signal.

When the aim is to report results such as differential cross sections, independent of the detector simulation, the observed event counts have to be corrected for detector effects. This problem can be written as:

$$\tilde{y}_i = \sum_{j=1}^{m} = A_{ij}\tilde{x}_j \ , \ 1 \leq i \leq n \tag{6.1}$$

where the m bins $\tilde{x}_j$ represent the true distribution of the searched signal, A_{ij} is a matrix of probabilities describing the migrations from bin j to any of the n bins on detector level and $\tilde{y}_i$ is the average expected event count at detector level. It is important to note here that the measured counts y_i may be different from the average $\tilde{y}_i$ due to statistical fluctuation. A sketch of this process is given in figure 6.1.

If there is some background the problem becomes more complicated. In this case the $\tilde{y}_i$ receives an additional contribution from the background. This can be expressed as:

$$\tilde{y}_i = \sum_{j=1}^{m} = A_{ij}\tilde{x}_j + b_i \ , \ 1 \leq i \leq n \tag{6.2}$$

where b_i is the background affecting the bin i. Both the background and the matrix of probabilities often suffer from systematic uncertainties which have to be considered in addition to the statistical uncertainties. One may be tempted to replace $\tilde{y}_i$ with y_i and $\tilde{x}_i$

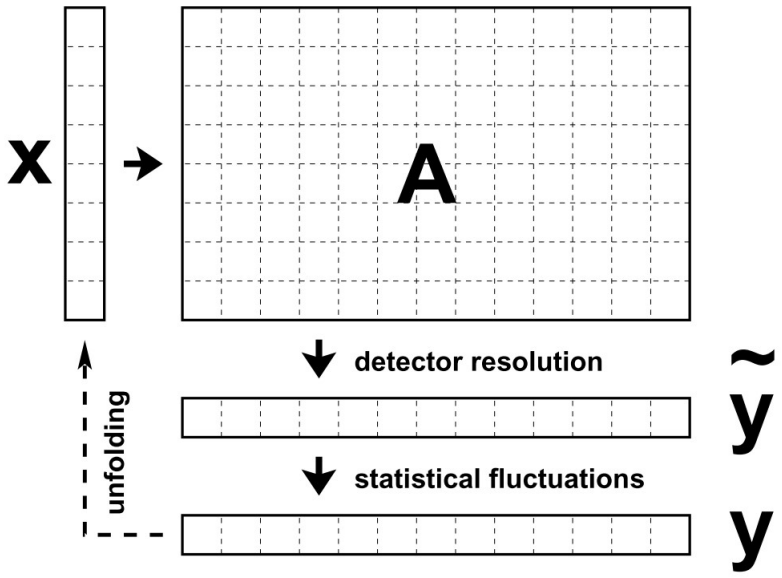

Figure 6.1: Schematic view of migration effects and statistical fluctuations. Figure taken from [100].

with x_i in equation 6.1 and 6.2 and then solve for x_j, simply by inverting the matrix of probabilities. However, it turns out that the statistical fluctuations of the y_i are amplified if the x_j are calculated this way. Such fluctuations can be damped in a procedure called *regularisation* by imposing smoothness conditions on the x_j.

Why Unfolding ?

Folding an assumed true distribution in x is simpler than unfolding an observed distribution in an attempt to obtain the true one, it is in general preferable to avoid unfolding. This then raises the question of when it might be necessary to unfold. A few cases are listed:

- Comparing or combining experimental distributions from experiments with different detectors.
- Tuning a Monte Carlo simulation, by fitting the parameters involved in the theory, to the data.
- Obtaining a plot for posterity that shows the estimate of the true distribution, rather than including the non-fundamental effects of experimental resolution.

For these reasons, the use of unfolding or deconvolution techniques in order to reconstruct the true underlying distribution is of primary importance.

6.1 Unfolding strategies and algorithms

No attempt is made here to give a complete overview of the commonly used unfolding algorithms, some reviews can be found in [101, 102]. However, it is relevant to specify that there are two major classes of unfolding algorithms:

- Algorithms based on matrix inversion or singular value decomposition. TUnfold [100], the algorithm used in this analysis, belongs to this category.
- Algorithms based on iterative methods or on the use of the Bayes' theorem [103].

For the purposes of this thesis, two main characteristics were required for the choice of the unfolding algorithm:

- Tested and validated algorithm, preferably in the context of high energy physics, and preferably easily interfaced with the ROOT framework that was largely used in this analysis.
- The possibility of handling one or more background sources in the unfolding procedure.

The bibliographic research has led to identify TUnfold [100] as the ideal algorithm for the continuation of the analysis in the unfolding step.

6.2 TUnfold

The TUnfold algorithm [100], implemented in the ROOT analysis framework, allows to estimate $\tilde{x}_j$ using a least square method, with Tikhonov regularisation [104] and an optional constraint. The mathematical structure on which the algorithm is based is a search for the stationary point of a Lagrangian multiplier problem described by the following equation:

$$\mathcal{L}(\boldsymbol{x}, \lambda) = \mathcal{L}_1 + \mathcal{L}_2 + \mathcal{L}_3 \tag{6.3}$$

where:

$$\mathcal{L}_1 = (\boldsymbol{y} - \boldsymbol{A}\boldsymbol{x})^T \boldsymbol{V}_{\boldsymbol{yy}}^{-1} (\boldsymbol{y} - \boldsymbol{A}\boldsymbol{x}) \tag{6.4}$$

is a least square minimisation problem in which the vector $\boldsymbol{y}$ has n rows and the covariance matrix $\boldsymbol{V}_{\boldsymbol{yy}}$ of $\boldsymbol{y}$ is diagonal in many cases, with the diagonal elements holding the squares of the uncertainties. TUnfold supports also the use of non-diagonal $\boldsymbol{V}_{\boldsymbol{yy}}$. The vector $\boldsymbol{x}$ corresponds to the result of the unfolding and has m rows. Finally the elements

A_{ij} of $\boldsymbol{A}$, describe the probabilities to migrate to bin i of $\boldsymbol{y}$ for each row j of $\boldsymbol{x}$. The matrix $\boldsymbol{A}$ is often determined using Monte Carlo simulations. The second term:

$$\mathcal{L}_2 = \tau^2(\boldsymbol{x} - f_B\boldsymbol{x}_0)^T(\boldsymbol{L}^T\boldsymbol{L})(\boldsymbol{x} - f_b\boldsymbol{x}_0) \tag{6.5}$$

describes the regularisation which dumps fluctuations in $\boldsymbol{x}$, coming from the statistical fluctuations of $\boldsymbol{y}$ that are amplified when determining the stationary point of equation 6.3. The parameter τ^2 gives the strength of the regularisation and is considered as a constant while determining the stationary point of $\mathcal{L}$. The matrix $\boldsymbol{L}$ has m columns and n_R rows, corresponding to n_R regularisation conditions. The product $f_b\boldsymbol{x_0}$ is the bias vector and is composed of a normalisation factor f_b and a vector $\boldsymbol{x_0}$. The simplest case is when $f_B = 0$, $n_R = m$ and $\boldsymbol{L}$ is the unity matrix. In that case, $\mathcal{L}_2$ becomes simply $\tau^2||\boldsymbol{x}||^2$, effectively suppressing large deviations of $\boldsymbol{x}$ from zero.

$$\mathcal{L}_3 = \lambda(Y - \boldsymbol{e}^T\boldsymbol{x}) \tag{6.6}$$

This last term is an optional constraint in which there is a Lagrangian parameter λ and the sum over all observations is given by:

$$Y = \sum_i y_i \tag{6.7}$$

The symbol $\boldsymbol{e}$ is the detector efficiency vector and has m rows. It is calculated starting from $\boldsymbol{A}$ with the following equation:

$$e_j = \sum_i A_{ij} \tag{6.8}$$

If the optional constraint is used, the normalisation of the result $\boldsymbol{x}$, corrected for the efficiencies $\boldsymbol{e}$, is forced to be equal to the total events Y. This procedure is applied in order to limit possible biases on the normalisation which are present if the data $\boldsymbol{y}$ follow Poisson's statistics whereas the least square assumption is strictly valid only for normal distributed measurements.

6.2.1 Stationary point

The minimum or stationary point of $\mathcal{L}(\boldsymbol{x}, \lambda)$ is determined by imposing the first derivative to zero. In the case without optional constraint, λ is set to zero and only the derivatives of $\mathcal{L}_1 + \mathcal{L}_2$ with respect to the components of $\boldsymbol{x}$ are set to zero. When including the optional constraint, the equations are solved for $\boldsymbol{x}$ and λ together. The partial derivatives of $\mathcal{L}(\boldsymbol{x}, \lambda)$ are:

$$\frac{\partial \mathcal{L}(\boldsymbol{x},\lambda)}{\partial x_j} = -2\left(\boldsymbol{A}^T\boldsymbol{V}_{\boldsymbol{yy}}^{-1}(\boldsymbol{y}-\boldsymbol{A}\boldsymbol{x})\right)_j + 2\tau^2\left((\boldsymbol{L}^T\boldsymbol{L})(\boldsymbol{x}-f_B\boldsymbol{x_0})_j\right) - \lambda e_j, \tag{6.9}$$

$$\frac{\partial \mathcal{L}(\boldsymbol{x},\lambda)}{\partial \lambda} = Y - \boldsymbol{e}^T\boldsymbol{x} \tag{6.10}$$

In order to calculate the covariance matrix of $\boldsymbol{x}$, given the covariance matrix of $\boldsymbol{y}$, the corresponding partial derivtives are calculated:

$$(\boldsymbol{D^{xy}})_{ki} := \frac{\partial x_k}{\partial y_i} \tag{6.11}$$

Finally, the covariance matrix of $\boldsymbol{x}$, originating from $\boldsymbol{V_{yy}}$, is given by:

$$\boldsymbol{V_{xx}} = \boldsymbol{D^{xy}}\boldsymbol{V_{yy}}(\boldsymbol{D^{xy}})^T \tag{6.12}$$

6.2.2 Regularisation

The strength of the regularisation, the value of τ^2, is an unknown parameter. If τ^2 is too small, the unfolding result often has large fluctuations and correspondingly large negative correlations of adjacent bins. If τ^2 is too large, the result is biased towards $f_b\boldsymbol{x_0}$. There are several methods to determine the strength of the regularisation like eigenvalue analyses [105], minimisation of correlation coefficients [106], and the L-curve method [107]. TUnfold implements a simple version of the L-curve method.

L-curve scan

The idea behind the L-curve method is to look for the point where the curvature is maximal along the curve defined by the variables L_x^{curve} and L_y^{curve}. These variables are expressed as:

$$L_x^{curve} = log\mathcal{L}_1 \tag{6.13}$$

and

$$L_y^{curve} = log\frac{\mathcal{L}_2}{\tau^2} \tag{6.14}$$

In TUnfold, the L-curve algorithm is implemented by scanning the L-curve for different values of $t = log\tau$. Eventually the curvature C of the L-curve is computed as:

$$C = \frac{d^2L_y^{curve}dL_x^{curve} - d^2L_x^{curve}L_y^{curve}}{((dL_x^{curve})^2 + (L_y^{curve})^2)^{\frac{3}{2}}} \tag{6.15}$$

The maximum of C is finally determined with the help of a cubic spline parametrisation of $C(\tau)$ and the strength of the regularisation τ^2 is fixed.

6.2.3 Background subtraction

It may happen that the measured data **y** contain some background. In this case background means all types of events, which are possibly reconstructed in one of the bins of **y** but do not originate from any of the bins of **x**. Part of the signal can be generated outside the phase-space covered by **x** and thus is counted as background. In TUnfold, a method of background subtraction prior to the unfolding is implemented. The procedure is described by the following equations:

$$\boldsymbol{y} = \boldsymbol{y^0} - f^b \boldsymbol{b} \tag{6.16}$$

$$(\boldsymbol{V_{yy}})_i j = (\boldsymbol{V^0_{yy}})_{ij} + \delta_{ij}(f^b(\boldsymbol{\delta b})_i)^2 + (\delta f^b)^2 b_i b_j \tag{6.17}$$

The components of $\boldsymbol{y^0}$ are the data before the background subtractio, with the covariance matrix $\boldsymbol{V^0_{yy}}$, f^b is a normalisation factor with uncertainty δf^b. The background distribution is represented by a vector **b** and the uncertainties on the components of **b** are given by the vector $\boldsymbol{\delta b}$. Finally, δ_{ij} is the Kronecker symbol.

The covariance matrix $\boldsymbol{V_{yy}}$ receives contributions from $\boldsymbol{y^0}$ as well as from the uncertainties on the background shape. In addition also the background normalisation uncertainty contributes to the covariance matrix. The implementation of the background subtraction in TUnfold allows to handle multiple background sources.

6.3 Unfolding ANTARES data

Figure 6.2 shows a sketch of the unfolding procedure that has been applied to the data collected by the ANTARES experiment. The purpose of the procedure is to obtain the corrected energy distribution of the selected events, starting from the energy distribution estimated by the TANTRA reconstruction algorithm. The procedure is divided into two parts, with the same structure, since the analysis goal is to measure the energy spectrum of both electron and muon neutrinos. What differentiates the two cases are respectively the unfolding matrix and the choice of background source for the background subtraction procedure.

The ingredients needed for the unfolding procedure, as can be seen from the figure 6.2, are:

- The reconstructed energy distribution of the selected events;
- The unfolding matrices for the electron and muon neutrinos;
- The background distributions for each of the two cases.

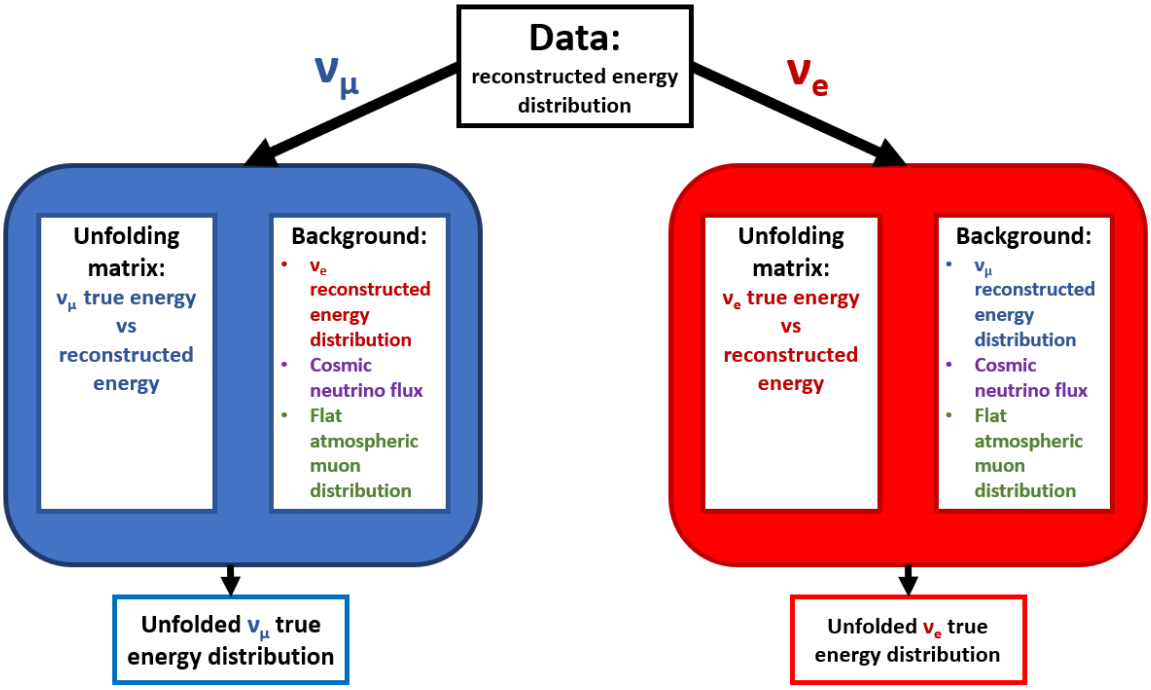

Figure 6.2: Schematic representation of the steps of the unfolding procedure and the necessary ingredients. Starting from the data represented by the top rectangle, the procedure splits to finally obtain the unfolded energy distribution for ν_e and ν_μ. In the figure a color code to identify what concerns the muon neutrinos, in blue, and what concerns the electron neutrinos, in red, has been used. The purple code referes to the cosmic neutrino flux and the green one to the flat muon distribution. Both these channels are used as background sources.

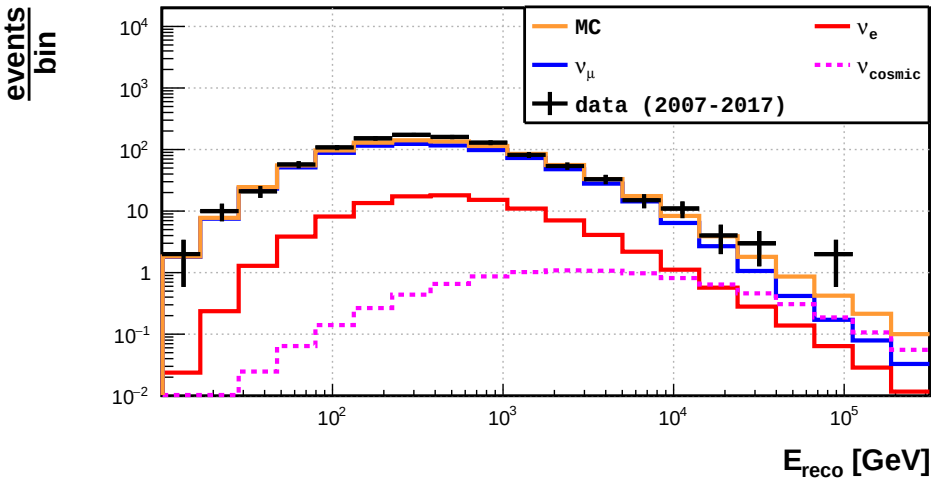

Figure 6.3: Reconstructed energy distribution with the Tantra algorithm for *shower-like* events. The black crosses are real data while the orange line is the sum of all Monte Carlo contributions. The blue line refers to atmospheric muon neutrinos and the red one to atmospheric electron neutrinos. Finally the magenta line is the cosmic neutrino flux estimated with the ANTARES data in a previous analysis [97].

6.3.1 Reconstructed energy distribution

Figure 6.3 shows the distribution of the reconstructed energy, for data and Monte Carlo, after the event selection chain. An important aspect regarding the graph is that with this event selection there is the access to events that are reconstructed in the desired energy range in order to finalise the analysis, from some GeV to a few dozens of TeV. Still, from the point of view of the energy range, it is evident at a glance how the data show an excess compared to simulations for very high energies $\sim$ 100 TeV. This excess is attributable to a flux of cosmic neutrinos above a few dozens of TeV that is expected to be higher than the flux of atmospheric neutrinos. No atmospheric muon events are shown in this figure since they have been removed with the cut on the BDT parameter. However the estimation of a maximum of three atmospheric muon events will be taken into account in the background subtraction procedure.

6.3.2 Unfolding matrices

Since the unfolding procedure aims to move from the reconstructed energy distribution of events to that of true energy, the unfolding matrix $\boldsymbol{A}$, defined in equation 6.4, is built from the Monte Carlo simulations, as a two-dimensional histogram in which the true energy of the events is on the x axis and the estimated energy on the y axis. Critical

	Reco energy range	Reco energy bins	True energy range	True energy bins
ν_e	80 GeV ÷ 40 TeV	6	80 GeV ÷ 40 TeV	3
ν_μ	100 GeV ÷ 50 TeV	15	100 GeV ÷ 50 TeV	5

Table 6.1: Binning and energy range for electron and muon neutrinos, both for the reconstructed and true energy.

for the construction of these histograms is the choice of the binning and the range of each axis. In the unfolding procedure, in order to obtain best results from the least square minimisation, the number of degrees of freedom, $n - m$, has to be larger than zero. It means that the data y_i have to be measured in finer bins that are extracted by the unfolding procedure.

For this analysis, the binning and energy ranges chosen for electron and muon neutrinos, are shown in table 6.1. For the binning choice, several tests were made with simulated data samples generated starting from the distributions represented in figure 6.3. The binning shown in the table 6.1 is the one that allowed the higher stability in terms of unfolding result compared to the input data. As regards the choice of the energy range, it was decided to limit the minimum reconstructed energy to $\sim$ 100 GeV and the maximum to $\sim$ 50 TeV. The lower bound is determined by the fact that our reconstruction algorithm cannot reliably reconstruct neutrino energies below that limit. Concerning the upper bound, above 50 TeV the event statistics is significantly reduced by the request of the interaction vertex within, or near to, the instrumented volume. In addition, cosmic neutrinos, whose flux suffers large uncertainties, starts to be dominant above these energies.

Figures 6.4 and 6.5 show the unfolding matrix used in data analysis respectively for electron and muon neutrinos.

6.3.3 Background definition

In figure 6.2 the background sources both for the muon and electron neutrino unfolding procedure are shown. The electron/muon neutrino reconstructed energy distribution are are those shown in the figure 6.3, respectively blue and red lines. The background from the cosmic neutrino flux is the reconstructed energy distribution in figure 6.3 represented by a magenta dashed line. The number of atmospheric muon events in the final sample, survived the selection with the BDT, are estimated to be at most 3. To take this background source into account, a flat distribution whose integral is 3 over the entire energy range shown in figure 6.3, is used in the unfolding procedure.

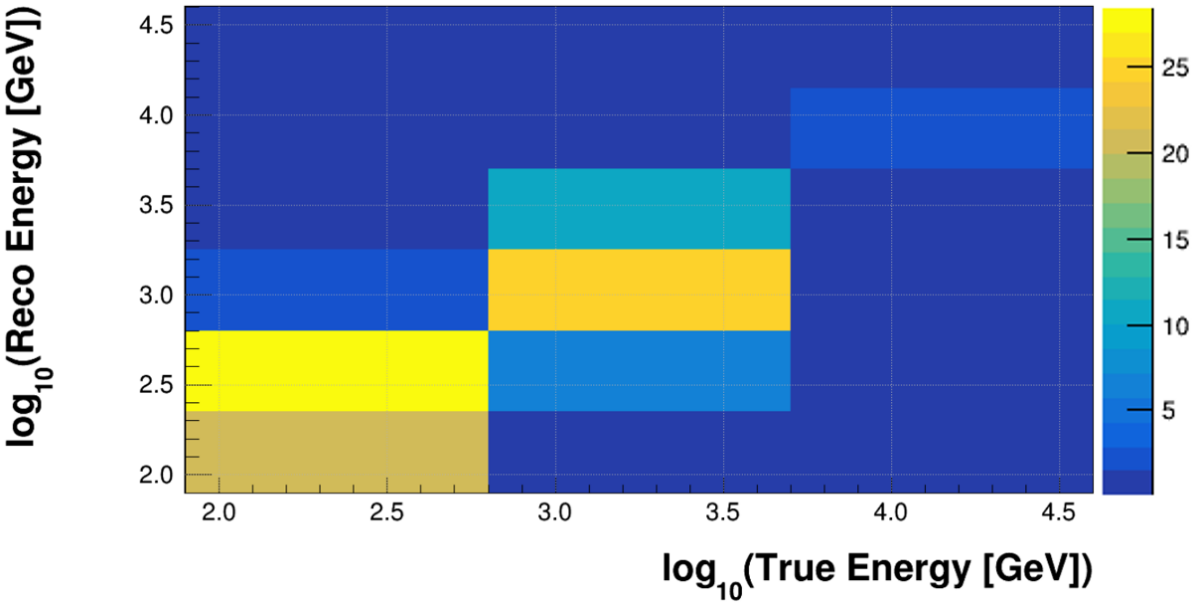

Figure 6.4: Unfolding matrix for **electron neutrinos**. On the x axis there is the true energy of neutrinos while on the y axis the reconstructed energy. The color code shows the number of event in each bin.

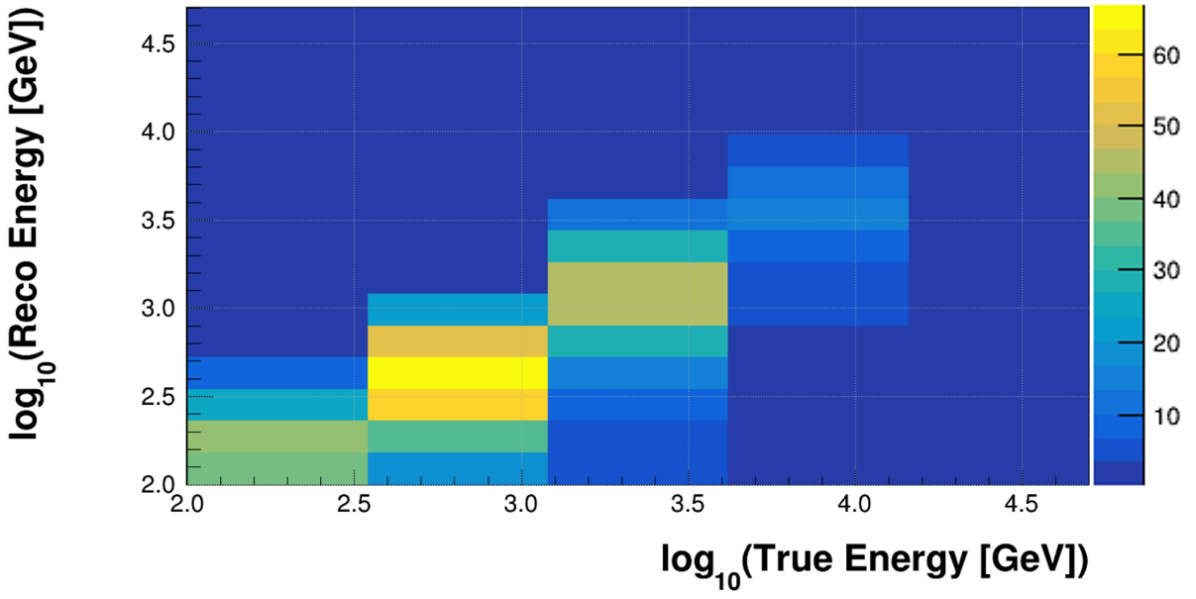

Figure 6.5: Unfolding matrix for **muon neutrinos**. On the x axis there is the true energy of neutrinos while on the y axis the reconstructed energy. The color code shows the number of event in each bin.

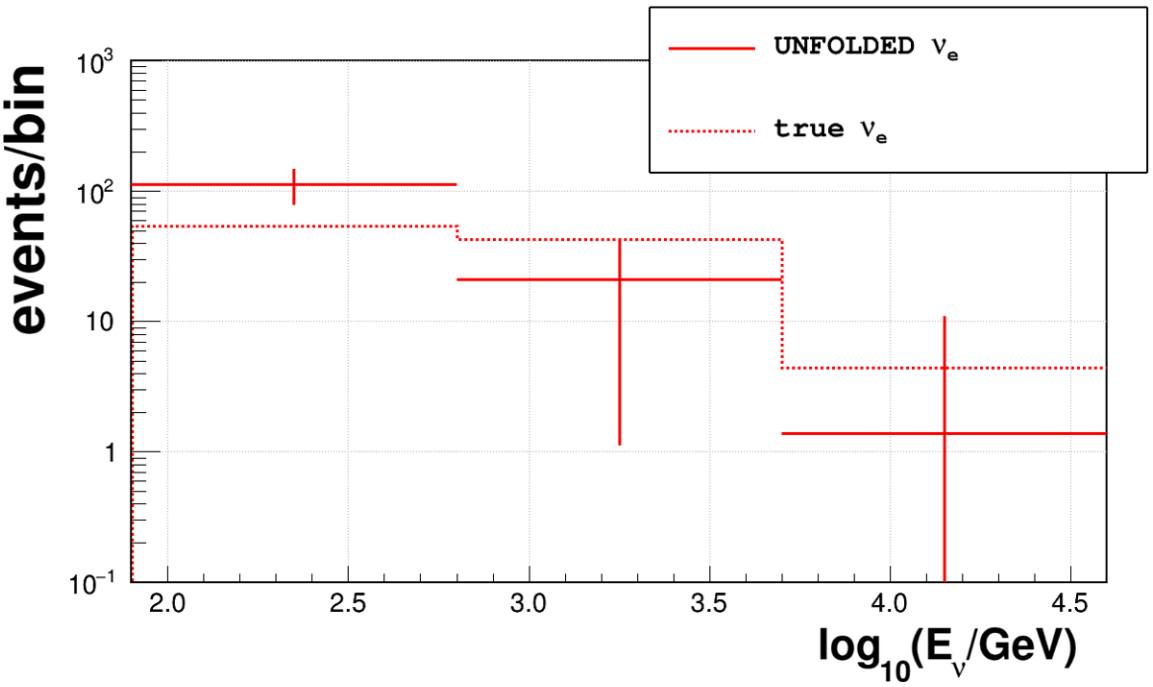

Figure 6.6: Electron neutrinos unfolded histogram compared with the true energy distributions generated in the Monte Carlo simulations. Crosses refer to unfolded distributions and dashed lines refer to simulated distributions.

6.4 Unfolding result

Following the strategy shown in figure 6.2, using the reconstructed energy distribution related to the data collected by the ANTARES telescope and the unfolding matrices represented in figure 6.4 and 6.5, the unfolding has been performed to obtain the true energy distributions of the electron and muon atmospheric neutrinos. The results are shown in figures 6.6 and 6.7 and the number of event in each bin both for muon and electron neutrino is reported in the third column of table 7.1. As it can be seen the unfolded points are close to the Monte Carlo simulation model at higher energies while they show an excess of events at lower energies. This is due to the over fluctuation observed in the data, shown in 6.3, between 100 GeV and 1 TeV of reconstructed energy.

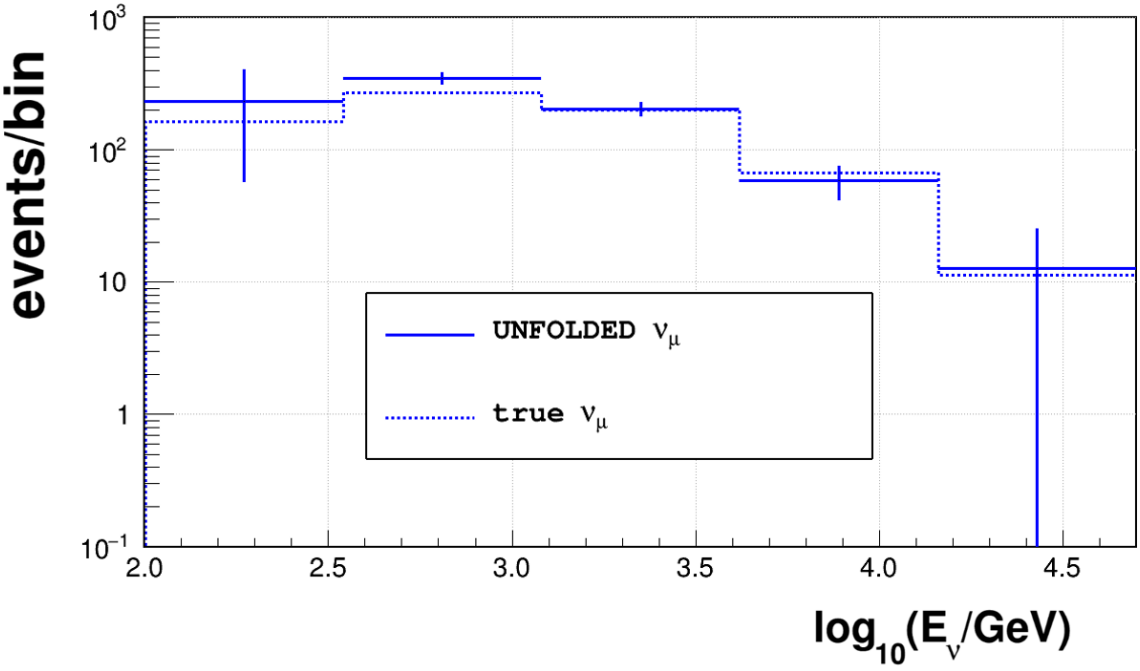

Figure 6.7: Muon neutrinos unfolded histogram compared with the true energy distributions generated in the Monte Carlo simulations. Crosses refer to unfolded distributions and dashed lines refer to simulated distributions.

7 Atmospheric neutrino flux

7.1 From unfolded energy to atmospheric flux

The unfolded energy distribution (figures 6.6 and 6.7) is given in relation to the livetime of the analyzed data, corresponding to 3012 days. To obtain the flux of atmospheric neutrinos in the proper units ($\mathrm{GeV}^{-1} \cdot \mathrm{cm}^{-2} \cdot \mathrm{s}^{-1} \cdot \mathrm{sr}^{-1}$), several steps are required:

1. Divide each bin for the livetime, expressed in seconds, thus obtaining the number of events per bin per second: [N_{events} bin^{-1} s^{-1}]. This result is the integral of the flux integrated in the logarithm of the neutrino energy.

2. Divide each bin by the width of the bin itself, 0.53 for ν_μ and 0.8 for ν_e, to obtain a number of events per unit of $\log_{10}$ (E_ν).

3. The flux is isotropic at the Earth's surface: what has been obtained so far is the result of the integration on the solid angle. To take this into account, it is necessary to divide each bin by considered solid angle, that is 2π sr.

4. The unfolded energy (figures 6.6 and 6.7) is binned as a function of $\log_{10}$ (E_ν), thus it represents a flux expressed as: $[\frac{d\phi}{d\ log_{10}(E_\nu)}]$. The final result has to be expressed as a function of dE_ν.

   Given that:

   $$\frac{d\phi}{dE_\nu} = \frac{d\phi}{d\ log_{10}(E_\nu)} \cdot \frac{d\ log_{10}(E_\nu)}{dE_\nu} = \frac{d\phi}{d\ log_{10}(E_\nu)} \cdot \frac{1}{E_\nu \cdot ln(10)} \tag{7.1}$$

   and applying this to each bin, taking as E_ν the median value of each bin, the result is a distribution expressed in: $[GeV^{-1} \cdot s^{-1} \cdot sr^{-1}]$

5. The last step is to divide each bin by the value of the effective area (see next section), calculated at the corresponding energy.

7.1.1 Effective area

The neutrino effective area is defined as:

$$A^{\nu}_{eff}(E_\nu, \theta_\nu, \phi_\nu) = \frac{N_x(E_\nu, \theta_\nu, \phi_\nu)}{N_{gen}(E_\nu, \theta_\nu, \phi_\nu)} \cdot V_{gen} \cdot \rho N_A \cdot \sigma(E_\nu) P_{Earth}(E_\nu, \theta\nu) \tag{7.2}$$

where:

- N_x is the number of events that are selected after triggering, reconstruction and event selection chain;
- N_{gen} is the number of generated events for that energy/zenith/azimuth range;
- V_{gen} is the generation volume;
- ρ and N_A are the matter density and the Avogadro number;
- $\sigma(E_\nu)$ is the neutrino cross section at the energy E_ν;
- P_{Earth} is the absorption probability for the neutrino through the Earth.

The definition shows that this parameter represents the size of a virtual target that the detector offers to a certain simulated neutrino flux. The effective area is therefore a figure of merit for a neutrino telescope, *the bigger the better*. The effective area depends on the design of the experiment, the quality of the trigger, the efficiency of the reconstruction algorithms and finally the effectiveness of the event selection.

In figure 7.1 the effective area obtained from the selection of events developed in this work is shown. As can be seen, this analysis can detect events from a few dozens of GeV, below which a denser detector would be needed, and up to few hundreds of TeV, after which the effective area has a drop because at extreme energies there would be need a much larger detector and the Earth starts to be opaque to a flux of neutrinos.

The peak of the electron anti-neutrinos around $\sim$ 6 PeV is due to the so-called *Glashow resonance*, conjectured by Sheldon L. Glashow in 1959 [99], when an electron anti-neutrino interacts with an electron producing a real W boson. The threshold for this process is easily calculated by placing the electron at rest in the laboratory frame and gives the result of 6.3 PeV.

7.2 Systematic uncertainties

The result of the unfolding process is dependent on the Montecarlo simulations via the building of the unfolding matrix. Simulations indeed depend on several parameters like the light collection efficiency of the optical modules, the light propagation properties of water and the dependency of the light detection probability on the direction of arrival

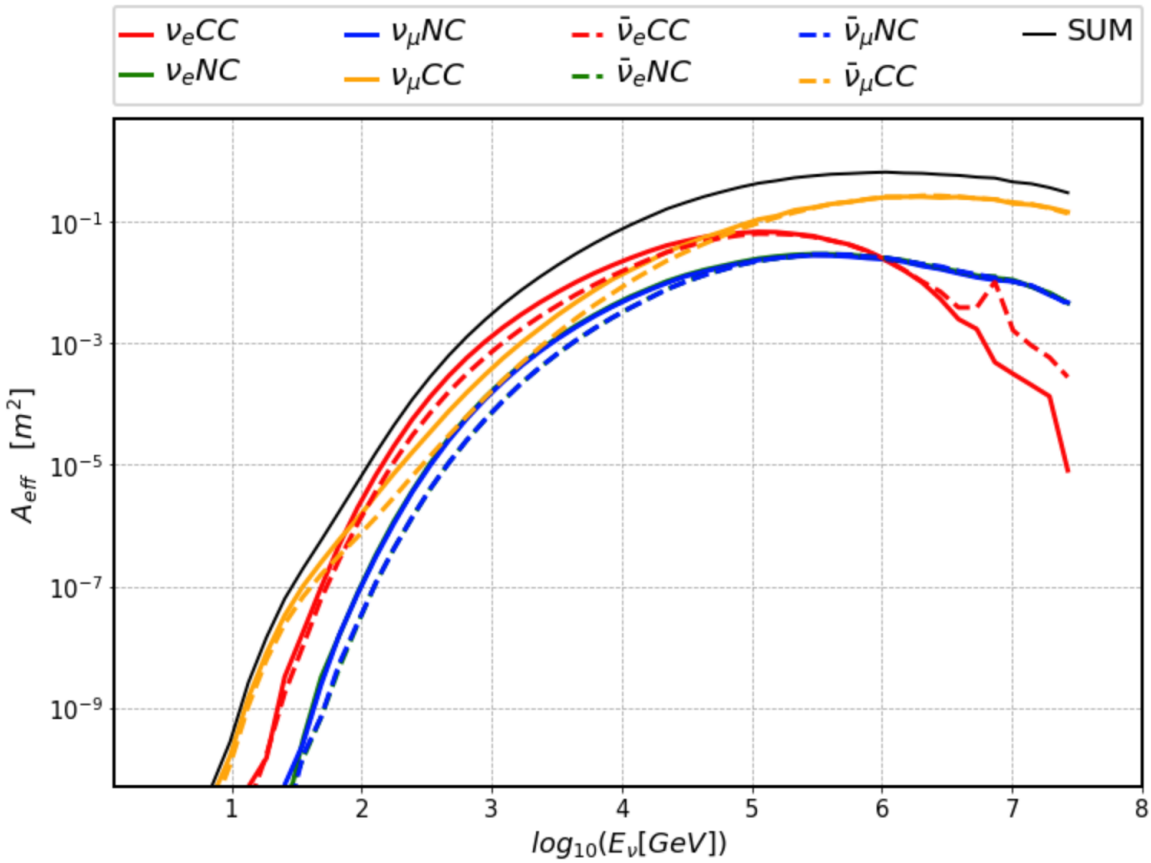

Figure 7.1: Effective area of the ANTARES neutrino telescope for the events selected with the event selection developed for this work and the energy estimated by the Tantra *shower-like* reconstruction algorithm. The yellow lines refer to charge current muon neutrino events, the blue ones refer to neutral current muon neutrino events, the red ones are for the charge current electron neutrino events and the green lines, that are actually hidden behind the other lines, refer to neutral current electron neutrino events. The solid lines represent neutrinos while dashed lines are for anti-neutrinos. Finally, the black solid line is the sum of all the interaction channels and neutrino flavours therefore it's the overall effective area.

of photons onto the PMTs and the atmospheric neutrino model used in the Montecarlo simulations.

The systematics uncertainties considered in this analysis are:

- ± 10% on the nominal value of the absorption length of light in sea water (*abs*_1.1, *abs*_0.9);
- ± 10% on the nominal value of the overall optical module (*om*_1.1, *om*_0.9*)*
- ± 0.1 on the nominal value of the spectral index of the atmospheric neutrino model in the Montecarlo simulations.

Systematic effects are evaluated using different specialised simulation data sets (*systematic MC*). These Montecarlo samples have been produced by changing the absorption length, the optical module efficiency or the spectral index of the simulated atmospheric neutrino flux. These simulations have been processed by the same chain of reconstruction algorithms and event selection criteria used for the data and the *nominal MC*.

Figure 7.2 schematizes the unfolding procedure used to evaluate the systematic uncertainties effect on the atmospheric neutrino flux measurement. This strategy, applied for electron and muon neutrinos, and for each different *systematic MC*, can be summarized as follow:

- The reconstructed energy distribution, the input for the unfolding procedure has been always the *nominal MC*;
- The unfolding matrices have been built from the four *systematic MC* and one from the *nominal MC*;
- The background source for the background subtraction procedure (with the inclusion of the cosmic neutrino background and the flat atmospheric muon distribution) and the effective area were built using the *nominal MC*;

Using this strategy, 7 different versions of the atmospheric neutrino flux for the electron neutrinos, and 7 more for the muon neutrino fluxes, were produced: 1 corresponding to the use of only the *nominal MC* and 6 from the usage of *systematic MC* for the unfolding matrices.

The ratio between the flux computed only with the *nominal MC* and each flux obtained from the *systematic MC* has been computed for each energy bin of the flux.

Estimates of the effect of systematic uncertainties on atmospheric neutrino flux are shown in figure 7.3 for muon neutrinos and in figure 7.4 for electron neutrinos. In both figures the sum in quadrature of the systematics is also reported in order to appreciate the global effect of all the possible systematic uncertainties that come into play in the

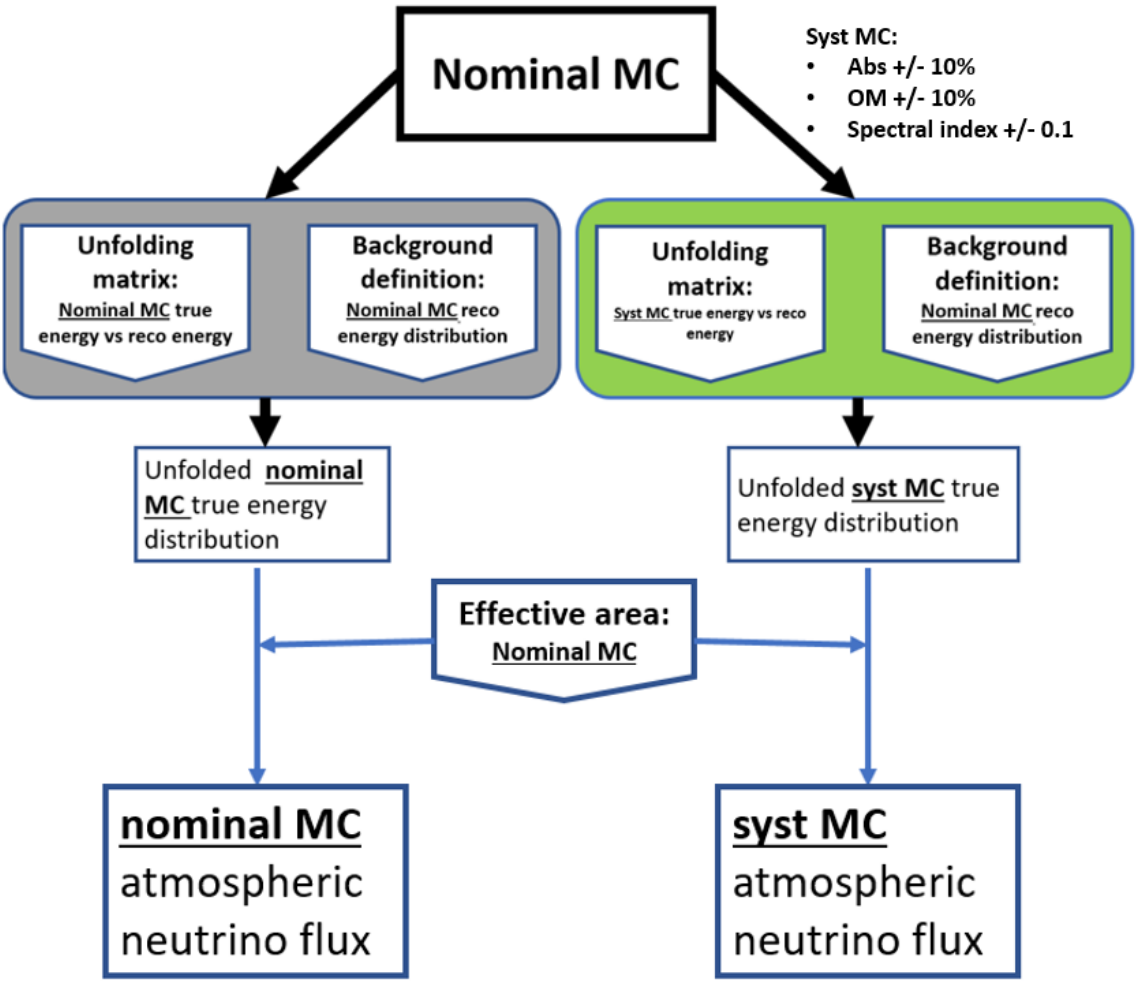

Figure 7.2: Schematic representation of the steps of the unfolding procedure to evaluate di effects of the systematics uncertainties on the atmospheric neutrino flux. The procedure starts with the nominal MC data as input for the unfolding, after which the procedure is divided in the nominal MC flux evaluation and the systematics fluxes evaluation. This procedure is used both for the muon neutrinos systematics evaluation and the electron neutrinos one.

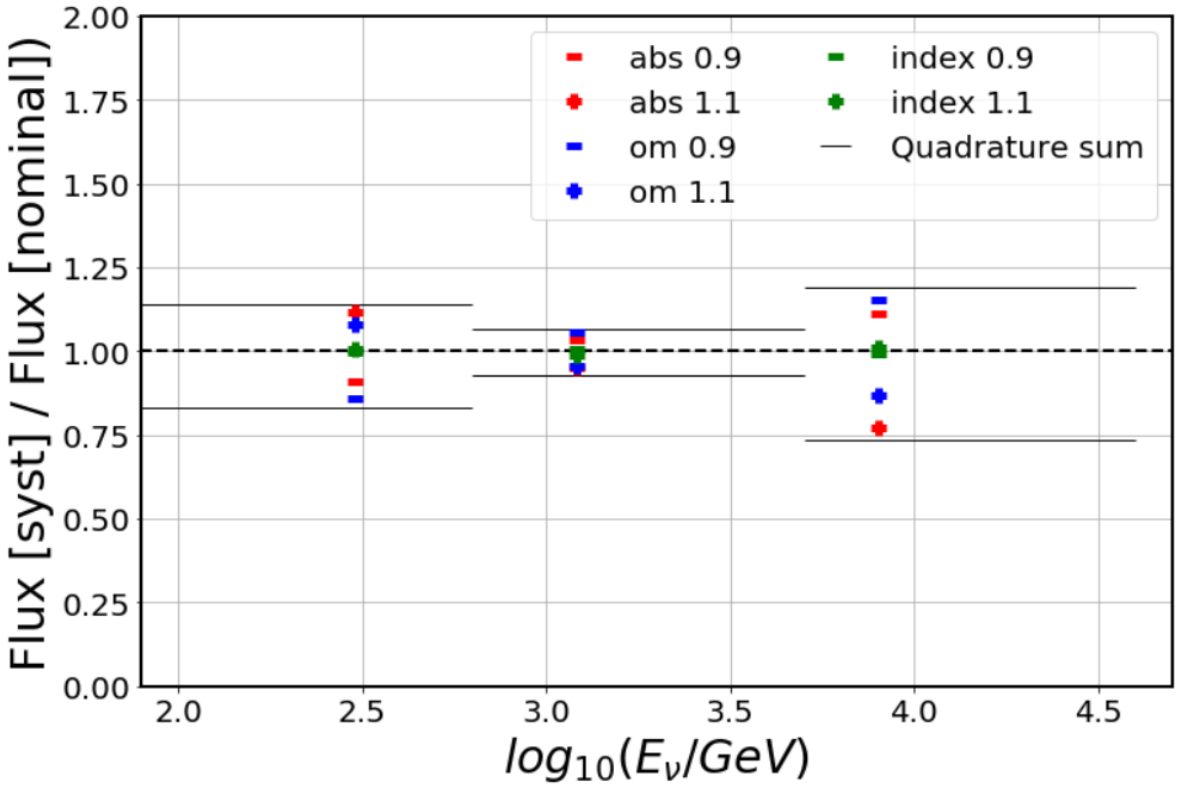

Figure 7.3: Systematic uncertainties calculated for each muon neutrino energy bin. Red points represent the effect given by a ±10% change in the absorption length in water. Blue points represent the effect given by a ±10% change in the OM efficiency with respect to the default value. The black lines represent the quadrature sum, bin by bin, of the systematic variations respect to the nominal MC.

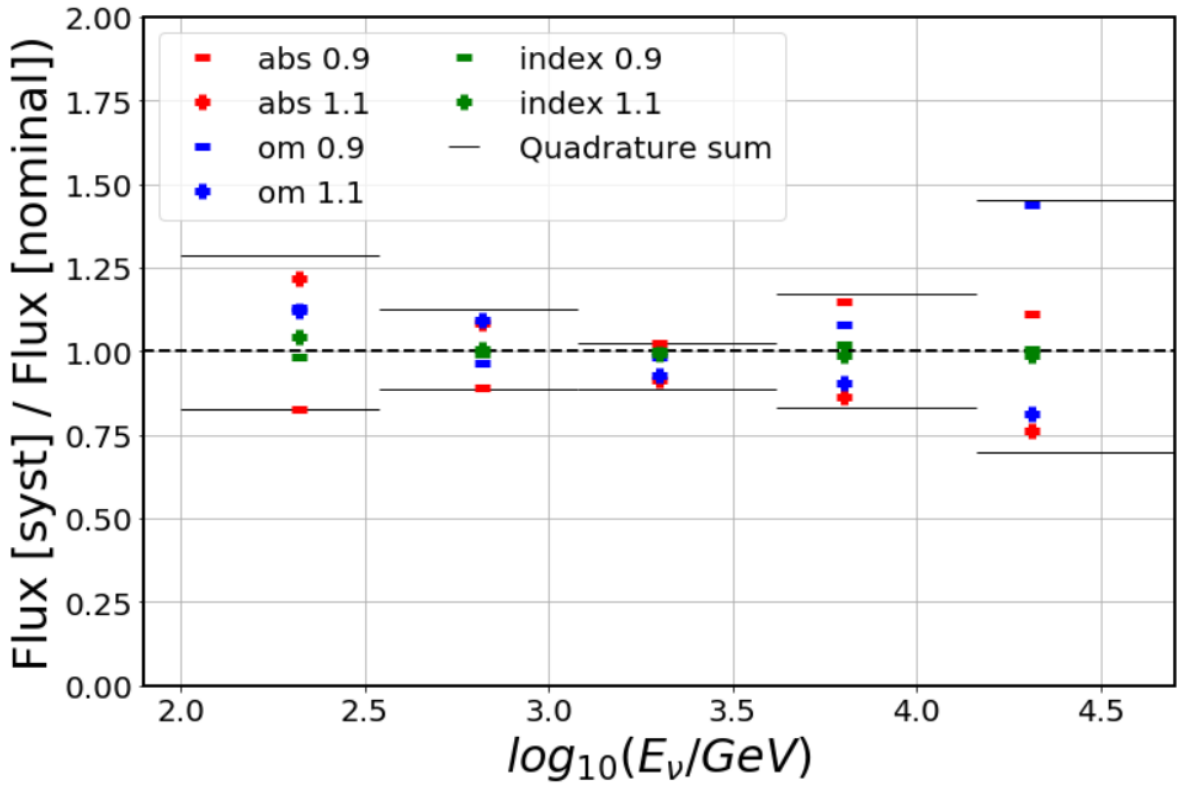

Figure 7.4: Systematic uncertainties calculated for each electron neutrino energy bin. Red points represent the effect given by a ±10% change in the absorption length in water. Blue points represent the effect given by a ±10% change in the OM efficiency with respect to the default value. The black lines represent the quadrature sum, bin by bin, of the systematic variations respect to the nominal MC.

$\Delta \log E_\nu$	$\overline{\log E_\nu}$	N^{evt}	$E_\nu^2 \Phi_\nu$	stat.	syst.
Atmospheric muon neutrinos					
2.00–2.54	2.32	232	2.4×10^{-4}	±80%	±30%
2.54–3.08	2.82	348	6.8×10^{-5}	±10%	±15%
3.08–3.62	3.30	203	1.4×10^{-5}	±15%	±15%
3.62–4.16	3.80	58	2.2×10^{-6}	±40%	±20%
4.16–4.70	4.31	13	3.8×10^{-7}	±100%	±40%
Atmospheric electron neutrinos					
1.9–2.8	2.48	113	1.2×10^{-5}	±30%	±20%
2.8–3.7	3.08	21.2	4.7×10^{-7}	±80%	±10%
3.7–4.6	3.9	1.4	1.7×10^{-8}	$^{+200\%}_{-100\%}$	±20%

Table 7.1: $\Delta \log E_\nu = \log_{10} \frac{E_\nu^{min}}{GeV}$–$\log_{10} \frac{E_\nu^{max}}{GeV}$; the weighted centre of the bin, $\overline{\log E_\nu} = \log_{10} \frac{\langle E_\nu \rangle}{GeV}$; the number of events assigned to the bin, N^{evt}; the differential flux (times E_ν^2) computed in the centre of the bin, $E_\nu^2 \Phi_\nu$, in units of GeV cm^{-2} s^{-1} sr^{-1}; the statistical error; and the total systematic uncertainty.

flux measurement. As it can be seen from these figures, the systematics tend to diverge on the edges of the energy range, both for muon neutrinos and electron neutrinos.

For muon neutrinos, the systematic uncertainties vary from a maximum of over 40% uncertainty for the highest energy bin to a minimum of around 15% uncertainty for the bin above 1 TeV.

For electron neutrinos the effect of the systematic uncertainties are always contained within an error of 20% with respect to flux computed with the *nominal MC*.

7.3 Atmospheric neutrino flux measurement

This section discusses the result obtained using the unfolding procedure on the selected events from the data collected by the ANTARES neutrino telescope between 2007 and 2017. The results of the analysis are two energy spectra, for electron neutrinos and for muon neutrinos respectively. Both fluxes are measured in the energy range between ∼100 GeV to ∼50 TeV. The electron neutrino flux is described with 3 points and the muon neutrino flux is measured with 5 points.

The results are multiplied by a E_ν^2 to facilitate the comparison with previous analyses of ANTARES and of other experiments.

Table 7.1 shows the measured values of the muon and electron neutrino spectra together with the statistical and systematic uncertainties.

Finally, figure 7.5 shows the values reported in the table 7.1. The plot also reports several measurements done in the past with other detectors both for electron and

muon neutrinos and in a very wide energy range from below 1 GeV up to hundreds of TeV. The measurement of the ν_e flux at high-energy is challenging, because very large detectors are needed to collect a statistical significant sample of events, and due to large systematic uncertainties. The present measurement is performed in seawater, under different environmental conditions and different systematic uncertainties with respect to the IceCube measurements ([47, 48]) but the result is consistent with that obtained in polar ice. Concerning the ν_μ flux, the ANTARES previous measurement [49] was done with a sample of through-going events generated by neutrino interactions external to the instrumented volume. The present measurement uses a totally independent data sample, provided by neutrino with interaction vertex reconstructed in (or nearby) the instrumented volume of the detector. The present measurement almost overlaps that of IceCube with 40 lines [46] and is about 25% below ANTARES previous measurement [49] and the flux reported by IceCube with 59 strings [109], although largely consistent within errors.

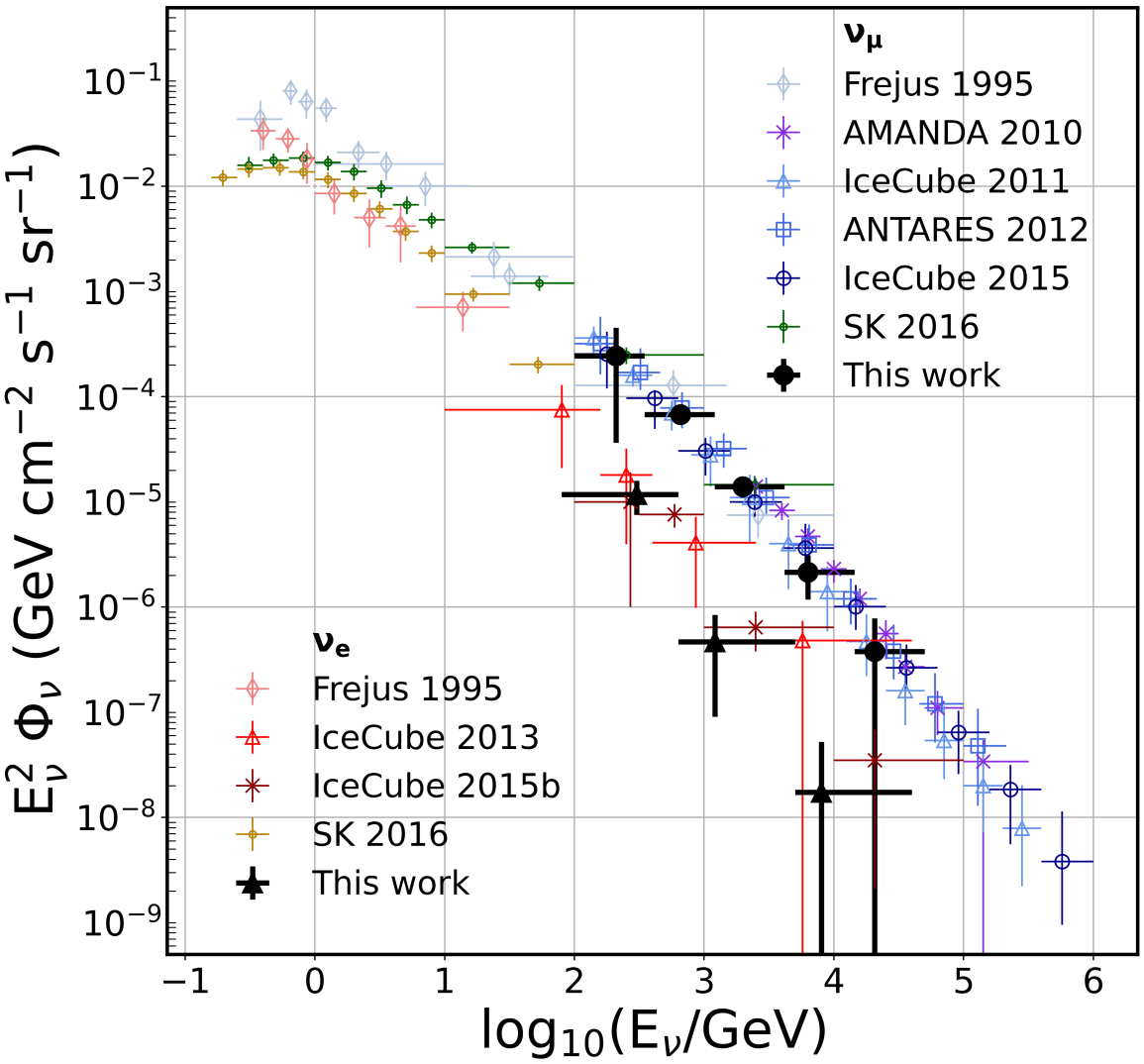

Figure 7.5: Measured energy spectra of the atmospheric ν_e and ν_μ using *shower-like* and *starting track* events in the ANTARES neutrino telescope (black). The measurements by other experiments (Frejus [43], AMANDA-II [45], IceCube [46, 109, 47, 48], and Super-Kamiokande [42]), as well as our ν_μ flux measurement using a different sample [49], are also reported. The error bars include all statistical and systematic uncertainties.

Summary and outlook

In this thesis, the first combined measurement of the energy spectra of atmospheric electron and muon neutrinos in the energy range between 100 GeV and 50 TeV with the ANTARES neutrino telescope, is presented. The analysis uses 3012 days of detector livetime in the period from 2007 to 2017, and selects 1016 neutrinos interacting in (or close to) the instrumented volume of the detector, yielding *shower-like* events and *starting-track* events. Thanks to the usage of a new dedicated event selection chain, including a Boosted Decision Tree classifier, the contamination due to atmospheric muons is suppressed at the level of a few per mill. The usage of the TUnfold unfolding algorithm allowed the separation between the atmospheric electron and muon neutrino fluxes. The result obtained is in agreement with previous measurements.

A reduction of the uncertainties, especially for the measurement of the electron neutrino spectrum, requires an increase of the statistical significance of the event sample. Larger-volume neutrino telescopes, foreseen in the next future (KM3NeT/ARCA and GVD-Baikal) or on a slightly longer term (such as IceCube-Gen2), will reach detection volumes of a few cubic kilometers, gathering much more data and therefore being more sensitive to the shape of the neutrino flux at the highest energies. Last but not least the possibility of combining different data-samples collected by different detectors will improve the knowledge of the atmospheric neutrino spectra, allowing the control of systematical uncertainties connected to the detectors.

Bibliography

[1] V.F. Hess. Phys. Zeit., 13:1084, (1912).

[2] DOI: 10.5281/zenodo.2360277

[3] Thomas K. Gaisser, Ralph Engel, and Elisa Resconi. Cosmic Rays and Particle Physics. Cambridge University Press, 2 edition, (2016). doi: 10.1017/CBO9781139192194.

[4] M.G. Aartsen et al., Science 342: 1242856, (2013).

[5] M.G. Aartsen et al., Phys. Rev. Lett. 113: 101101, (2014).

[6] A. Albert et al., Astr. Jour. Lett. 853, L7 (2018), Corresponding authors: Luigi Antonio Fusco, Sergio Navas, Federico Versari

[7] M. Longair, High Energy Astrophysics, Cambridge University Press, (1992).

[8] M. Tanabashi et al., Phys. Rev. D 98, 030001 (2018) and (2019) update.

[9] https://cosmicray.umd.edu/cream/

[10] https://cosmicray.umd.edu/atic-home

[11] Muller, D., 30th International Cosmic Ray Conference, (2007).

[12] W. Baade and F. Zwicky, Proc. of the National Academy of Science, 20:259–263, (1934).

[13] E. Fermi, Phys. Rev. 75: 1169, (1949).

[14] E. Fermi, Astroph. J. 119: 1, (1954).

[15] V. L. Ginzburg and S. I. Syrovatsky, Progress of Theoretical Physics Supplement, 20:1–83, (1961).

[16] R. Antonucci, Annual Reviews in Astronomy and Astrophysics 31 (1): 473-521, (1993).

[17] P. Urry and P. Padovani, Publications of the Astronomical Society of the Pacific 107: 803-845, (1995).

[18] P. Abreu et al., Astrop. Phys. 34: 314-326, (2010).

[19] Frail et al., Nature, 389, 261, (1997).

[20] Johannes Blumer, Ralph Engel, and JorgR. Horandel, Progress in Particle and Nuclear Physics, 63:293–338, (2009).

[21] A. Castellina, Proc. of Science ICRC2019:004, (2019).

[22] W. Hanlon, Proc. of Science ICRC2019:280 (2019).

[23] M. Bertaina, Proc. of Science ICRC2015:359 (2015).

[24] B. Bartoli et al., Phys. Rev. D 92, 092005 (2015).

[25] G. Di Sciascio, arXiv:1602.07600 (2016).

[26] L.Q. Yin et al., arXiv:1904.09130 (2019).

[27] A. Aab et al., arXiv:1604.03637 (2016).

[28] T.K. Gaisser, T. Stanev and S. Tilav, arXiv:1303.3565 (2013).

[29] T.K. Gaisser, Astrop. Phys. (35, 12): 801-806 (2012).

[30] S. Thoudam et al., Astronomy and Astrophysics 595:A33 (2016).

[31] H. Dembinski et al., Proc. of Science ICRC2017:533 (2017).

[32] A. Fedynitch, F. Riehn, R. Engel, T. K. Gaisser, and T. Stanev, Phys. Rev. D 100, 103018 (2019).

[33] F. Riehn, R. Engel, A. Fedynitch, T. K. Gaisser, and T. Stanev EPJ Web Conf. 99 (2015) 12001, [1502.06353].

[34] Honda, M., Kajita, T., Kasahara, K., Midorikawa, S., and Sanuki, T., PhRvD, 75, 043006, (2007).

[35] Enberg, R., Reno, M. H., and Sarcevic, I., Phys. Rev. D 78, 043005, (2008).

[36] G. Battistoni et al., AIP Conf. Proc., 96, (1983).

[37] M. Sanchez et al., Phys. Rev. D68, 113004, (2003). (Soudan 2 Coll.)

[38] D. Sinclair et al., Proc, Science Underground, pg. 138-142, (1982).

[39] http://www-sk.icrr.u-tokyo.ac.jp/sk/index-e.html .

[40] Y. Fukuda et al., Phys. Rev. Lett. 81, 1562 (1998).

[41] M. Ambrosio et al., Phys. Lett. 434, 451 (1998).

[42] E. Richard et al., Phys. Rev. D 94, 052001, (2016).

[43] K. Daum, Z. Phys. C 66, 417 (1995).

[44] R. Abbasi et al., Phys. Rev. D 79, 102005 (2009).

[45] R. Abbasi et al., Astropart. Phys. 34, 48 (2010).

[46] R. Abbasi et al., Phys. Rev. D 83, 012001 (2011).

[47] M. Aartsen et al., Phys. Rev. Lett. 110, 151105 (2013).

[48] M. G. Aartsen et al., Phys. Rev. D91, 122004 (2015).

[49] S. Adrian-Martinez et al., Eur.Phys. J. C 73, 2606 (2013).

[50] M. Honda, T. Kajita, K. Kasahara, and S. Midorikawa, Phys. Rev. D 83, 123001 (2011).

[51] M.A. Markov, Proc. Int. Conf. on High Energy Physics, p. 183, (1960).

[52] J.D. Jackson, Classical Electrodinamics (3rd ed.), John Wiley, ISBN 978-0-30932-1, (1998).

[53] J. a. Formaggio and G. P. Zeller,Rev. Mod. Phys. 84(2012)(3).

[54] A. Sánchez-Losa., PhD thesis. Universitat de València, Valencia, Spain, (2015).

[55] B. Hartmann,PhD thesis, University of Erlangen-Nurnberg, (2006).

[56] http://www.phys.hawaii.edu/dumand/

[57] I.A. Belolaptikov et al., Astrop. Phys. 7 (3):263-282, (1997).

[58] V. Aynutdinov et al., Astrop. Phys. 25: 140-150, 2006.

[59] A.D. Avrorin et al., PoS ICRC2019 (2020) 1011, DOI: 10.22323/1.358.1011.

[60] http://antares.in2p3.fr/.

[61] S. Adrian-Martınez et al.,arXiv:1601.07459, (2016).

[62] M. Ageron et al., Eur.Phys. J. C 80:99, (2020).

[63] F. Halzen, Eur. Phys. J. C, 46: 669-687, (2006).

[64] A. Karle et al., Proc. of the 31st ICRC, Lodz, Poland, (2009).

[65] M. G. Aartsen et al., Phys. Rev. Lett. 111 (2013) 021103, 1304.5356.

[66] M. G. Aartsen et al., Science 342 (2013) 1242856, 1311.5238.

[67] IceCube, Fermi-LAT, MAGIC, AGILE, ASAS-SN, HAWC, H.E.S.S., INTEGRAL, Kanata, Kiso, Kapteyn, Liverpool Telescope, Subaru, Swift NuSTAR, VERITAS, VLA/17B-403 Collaborations, M. G. Aartsen et al., Science 361 (2018) eaat1378, 1807.08816.

[68] M. G. Aartsen et al., Science 361 (2018) 147–151, 1807.08794.

[69] M. G. Aartsen et al, Submitted to the Journal of Physics G; arXiv:2008.04323 [astro-ph.HE], 10 August (2020).

[70] M. Ageron et al., Nucl. Inst. and Meth. in Phys. Res. A 656(1): 11–38, (2011).

[71] J. A. Aguilar et al., Nucl. Instrum. Methods Phys. Res. Sect. A 626-627, (2011).

[72] J.A. Aguilar et al., Nucl. Inst. and Meth. in Phys. Res. A 570: 106, (2007).

[73] J.A. Aguilar et al., Nucl. Inst. and Meth. in Phys. Res. A 555: 132, (2005).

[74] J.A. Aguilar et al., Astrop. Phys. 23: 131-155, (2005).

[75] P. Amram et al., Astrop. Phys. 19: 253-267, (2003).

[76] https://cc.in2p3.fr/

[77] Federico Versari, Search for a diffuse flux of cosmic neutrinos in the shower channel with the ANTARES telescope, Master thesis, (2016).

[78] https://root.cern.ch/tmva

[79] D.J.L. Bailey, ANTARES internal note, ANTARES-SOFT-2002-004, (2002).

[80] G. Ingelman et al., Comp. Phys. Comm. 101:108– 134, (1997).

[81] D. Heck et al., FZKA 6019, (1998).

[82] J. A. Aguilar et al., Nucl. Instrum. Meth. A 570 (2007) 107-116.

[83] G. Carminati et al., Comp. Phys. Comm. 179(12): 915-923, (2008).

[84] Y. Becherini et al, Astrop. Phys. 25: 1-13, (2006).

[85] M. Ambrosio et al., Phys. Rev. D 56: 1407, (1997).

[86] P. Antonioli et al., Astrop. Phys. 7: 357, (1997).

[87] L.A. Fusco and A. Margiotta, Proceedings of the VLVnT 2015 Conference, Rome, (2015).

[88] A. Albert et al., Eur. Phys. J. C 78 (2018) 669.

[89] T. Michael, PhD Thesis, University of Amsterdam, (2016).

[90] T. Michael, Proc. of the 34^{th} ICRC, The Hague, Netherlands, (2015); arXiv:1510.04508.

[91] M. Ageron et al., Nucl. Instrum. Meth. A 578 (2007) 498-509.

[92] A. Heijboer et al., Proc. of the 31^{st} ICRC, Lodz, Poland, (2009); arXiv:0908.0816.

[93] E. L. Visser, PhD Thesis, (2015).

[94] R.E. Schapire, Machine Learning 5 197-227, (1990).

[95] Y. Freund and R.E. Schapire, J. of Computer and System Science 55, 119 (1997).

[96] A. Albert et al., Phys. Rev. D 96, 082001 (2017).

[97] L.A. Fusco and F. Versari (ANTARES Collaboration) PoS(ICRC2019)891.

[98] L. Breiman, J. Friedman, R. Olshen and C. Stone, Wadsworth (1984).

[99] Glashow, Sheldon L. Phys. Rev. American Physical Society (APS). 118 (1): 316–317, (1960).

[100] S.Schmitt, JINST 7 (2012) T10003.

[101] V. B. Anykeev, A. A. Spiridonov and V. P. Zhigunov, Nucl. Instrum. Meth. A 303 (1991) 350.

[102] V. Blobel, proceedings of the PHYSTAT 2011 workshop, Eds. H. B. Prosper, L.Lynons, Geneva, (2011) 240.

[103] G. D'Agostini, Nucl. Inst. and Meth. in Phys. Res. A 362: 487, (1995).

[104] A. N. Tikhonov, Soviet Math. Dokl. 4 (1963), 1035.

[105] Glen Cowan, Oxford University Press (1998), ISBN 0198501560.

[106] V. Blobel, Hamburg (2010) http://www.desy.de/ blobel/.

[107] P. C. Hansen, Computational Inverse Problems in Electrocardiology, ed. P. Johnston (2000).

[108] M. G. Aartsen et al., Phys. Rev. D89, 102001 (2014).

[109] M. G. Aartsen et al.,Eur. Phys. J. C75, 116 (2015).